UNIVERSIDADE FEDERAL DO CEARÁ

CENTRO DE TECNOLOGIA

DEPARTAMENTO DE ENGENHARIA METALÚRGICA E DE MATERIAIS

PROGRAMA DE PÓS-GRADUAÇÃO EM ENGENHARIA E CIÊNCIA DE MATERIAIS

PEDRO QUEIROS SANTIAGO

MULTITECHNIQUE STUDY OF BIOCHAR AND BIOCHAR–BENTONITE COMPOSITE DERIVED FROM THE PETIOLE OF CARNAUBA (*COPERNICIA PRUNIFERA*) MODIFIED BY HIGH-ENERGY BALL MILLING FOR METHYLENE BLUE REMOVAL

FORTALEZA

2026

PEDRO QUEIROS SANTIAGO

MULTITECHNIQUE STUDY OF BIOCHAR AND BIOCHAR–BENTONITE COMPOSITE DERIVED FROM THE PETIOLE OF CARNAUBA (*COPERNICIA PRUNIFERA)* MODIFIED BY HIGH-ENERGY BALL MILLING FOR METHYLENE BLUE REMOVAL

Dissertation presented to the Postgraduate Program in Materials Science and Engineering of the Federal University of Ceará as a partial requirement for the degree of Master of Science in Materials Science and Engineering.

Supervisor: Prof. Dr. Ricardo Emílio Ferreira Quevedo Nogueira.

Fortaleza

2026

PEDRO QUEIROS SANTIAGO

MULTITECHNIQUE STUDY OF BIOCHAR AND BIOCHAR–BENTONITE COMPOSITE DERIVED FROM THE PETIOLE OF CARNAUBA (*COPERNICIA PRUNIFERA*) MODIFIED BY HIGH-ENERGY BALL MILLING FOR METHYLENE BLUE REMOVAL

Dissertation presented to the Postgraduate Program in Materials Science and Engineering of the Federal University of Ceará as a partial requirement for the degree of Master of Science in Materials Science and Engineering.

Approved on: 02/06/2026

EXAMINING COMMITTEE

_____

Prof. PhD. Ricardo Emílio Ferreira Quevedo Nogueira (Supervisor)
Universidade Federal do Ceará (UFC)

_____

Prof. PhD. Maria Alexsandra de Sousa Rios
Universidade Federal do Ceará (UFC)

_____

Prof. PhD. Men de Sa Moreira de Souza Filho
Empresa Brasileira de Pesquisa Agropecuária (EMBRAPA)

ACKNOWLEDGEMENTS

I am fully grateful to my family for their support, encouragement, and understanding throughout my academic journey.

I also sincerely thank Laryssa Coutinho da Silva, with whom I jointly conducted analyses and experiments, making a significant contribution to the development of this work.

I would like to express my gratitude to Prof. Ricardo Emilio Nogueira for his invaluable supervision and continuous support throughout the development of this research. I am also profoundly thankful to Prof. Maria Alexandra Rios for kindly providing the equipment and materials essential for carrying out this study. My appreciation is further extended to the members of the examination committee for their time, careful evaluation, and valuable contributions.

I would like to express my gratitude to the staff of the following laboratories for their support and assistance: the Technological Innovations and Chemical Specialties Group (GRINTEQUI) for support with material preparation and proximate analysis; the X-Ray Laboratory (LRX); the Electron Microscopy Laboratory (LME); the Vibrational Spectroscopy Laboratory (LEV); the Advanced Materials Laboratory (LMA); the Biomaterials Laboratory; and the Analytical Center of the Postgraduate Program in Chemistry.

This study was financed by the Coordenação de Aperfeiçoamento de Pessoal de Nível Superior (CAPES, Coordination for the Improvement of Higher Education Personnel), under the Ministry of Education of Brazil – Finance Code: 0001.

“A mente que se abre a uma nova ideia, jamais voltará ao seu tamanho original.” (Albert Einstein)

ABSTRACT

The escalating improper disposal of industrial effluents laden with synthetic dyes, such as methylene blue, constitutes a serious environmental hazard due to their high stability and recalcitrance to degradation. In this context, adsorption processes have gained prominence owing to their efficiency and operational simplicity, particularly when utilizing low-cost and sustainable materials. Among these, biochar and clays exhibit significant potential, especially when combined into hybrid composites that integrate high surface area, structural stability, and a diversity of functional groups. Accordingly, this study proposes the utilization of the carnauba palm petiole (*Copernicia prunifera*), an abundant and underexploited biomass, to produce clay-biochar composites for methylene blue removal. The biomass was pyrolyzed at 550 °C, producing a biochar (PB) with enhanced physicochemical properties, followed by modification through high-energy ball milling, with and without sodium bentonite clay incorporation. The results indicated that carbonization process induced significant compositional and structural changes on PB, including a reduction in volatile matter (from 77.77% to 31.04%), an increase in fixed carbon (from 9.20% to 36.96%), ash content (from 3.63% to 27.45%), along with carbon enrichment (from 43.49% to 64.02%) and a decrease in H/C and O/C ratios. Multitechnique characterization (XRD, FTIR, SEM/EDS, and thermal analyses) revealed the formation of a disordered carbonaceous matrix containing crystalline mineral phases, resulting in a heterogeneous surface with multiple active sites. High-energy ball milling significantly improved the adsorption capacity of biochar, reaching 72.39 $mg \cdot g^{-1}$ under the most severe condition (PB406). Composite materials exhibited superior performance even without milling (95.50 $mg \cdot g^{-1}$), while optimized milling conditions improved clay dispersion and accessibility of active sites. The best-performing composite (B-PB406) achieved near-complete removal efficiency (99.17%) and a maximum adsorption capacity of 205.67 $mg \cdot g^{-1}$, with excellent agreement with the Langmuir model. Thus, the results demonstrate that carnauba petiole-derived biochar and its bentonite composites are efficient and sustainable adsorbents for methylene blue removal, where the combination of pyrolysis, mechanical activation, and clay incorporation effectively tailors' material properties, enhancing adsorption through synergistic mechanisms.

Keywords: bioadsorbents; carnauba petiole; high-energy ball milling; bentonite; adsorption

RESUMO

O descarte inadequado crescente de efluentes industriais contendo corantes sintéticos, como o azul de metileno, constitui um sério risco ambiental devido à sua elevada estabilidade e resistência à degradação. Nesse contexto, os processos de adsorção têm ganhado destaque em função de sua eficiência e simplicidade operacional, especialmente quando utilizam materiais de baixo custo e sustentáveis. Dentre esses, o biocarvão e as argilas apresentam grande potencial, sobretudo quando combinados em compósitos híbridos que integram alta área superficial, estabilidade estrutural e diversidade de grupos funcionais. Assim, este estudo propõe a utilização do pecíolo da carnaubeira (*Copernicia prunifera*), uma biomassa abundante e subexplorada, para a síntese de compósitos argila-biocarvão voltados à remoção de azul de metileno. A biomassa foi submetida à pirólise a 550 °C, produzindo um biocarvão (PB) com propriedades físico-químicas aprimoradas, seguido de modificação por moagem de alta energia, com e sem a incorporação de argila bentonítica sódica. Os resultados indicaram que o processo de carbonização promoveu mudanças composicionais e estruturais significativas no PB, incluindo a redução do teor de materiais voláteis (de 77,77% para 31,04%), o aumento do carbono fixo (de 9,20% para 36,96%) e do teor de cinzas (de 3,63% para 27,45%), além do enriquecimento em carbono (de 43,49% para 64,02%) e da diminuição das razões H/C e O/C. A caracterização multitécnica (DRX, FTIR, MEV/EDS e análises térmicas) revelou a formação de uma matriz carbonácea desordenada contendo fases minerais cristalinas, resultando em uma superfície heterogênea com múltiplos sítios ativos. A moagem de alta energia promoveu aumento significativo na capacidade de adsorção do biocarvão, atingindo 72,39 $mg \cdot g^{-1}$ na condição mais severa (PB406). Os materiais compósitos apresentaram desempenho superior mesmo sem moagem (95,50 $mg \cdot g^{-1}$), enquanto condições otimizadas de moagem favoreceram a dispersão da argila e a acessibilidade dos sítios ativos. O compósito de melhor desempenho (B-PB406) alcançou eficiência de remoção quase completa (99,17%) e capacidade máxima de adsorção de 205,67 $mg \cdot g^{-1}$, com excelente ajuste ao modelo de Langmuir. Dessa forma, os resultados demonstram que o biocarvão derivado do pecíolo da carnaúba e seus compósitos com bentonita são adsorventes eficientes e sustentáveis para a remoção de azul de metileno, sendo que a combinação de pirólise, ativação mecânica e incorporação de argila permite modular as propriedades do material, potencializando a adsorção por meio de mecanismos sinérgicos.

Palavras-chave: bioadsorventes; pecíolo da carnaúba; moagem de alta energia; bentonita; adsorção.

LIST OF FIGURES

LIST OF TABLES

LIST OF GRAPHICS

ABREVIATIONS AND ACRONYMS LIST

AISI	American Iron and Steel Institute
ASTM	American Society for Testing and Materials
ATR	Attenuated Total Reflectance
BET	Brunauer–Emmett–Teller
BPB	Bentonite Petiole Biochar
BSE	Backscattered Electron
C	Carbon (elemental)
CAS	Chemical Abstracts Service Registry Number
CEC	Cation Exchange Capacity
CHNS	Carbon, Hydrogen, Nitrogen, Sulfur (elemental analysis)
DLS	Dynamic Light Scattering
DSC	Differential Scanning Calorimetry
DTA	Differential Thermal Analysis
DTG	Derivative Thermogravimetry
EBC	European Biochar Certificate
EDA	Electron Donor–Acceptor
EDS	Energy-Dispersive X-ray Spectroscopy
FC	Fixed Carbon
FTIR	Fourier Transform Infrared Spectroscopy
H	Hydrogen (elemental)
HEBM	High-Energy Ball Milling
HTC	Hydrothermal Carbonization
IBGE	Instituto Brasileiro de Geografia e Estatística (Brazil)
MB	Methylene Blue
MC	Moisture Content
MW	Molecular Weight
N	Nitrogen (elemental)
NaHMP	Sodium Hexametaphosphate
NBC	Nanobiochar
OPEFB	Oil Palm Empty Fruit Bunch
PB	Petiole Biochar

PFO	Pseudo-First Order
PSO	Pseudo-Second Order
rpm	Rotations per minute
RSM	Response Surface Methodology
SDG	Sustainable Development Goal (UN)
SE	Secondary Electron
SEM	Scanning Electron Microscopy
SSA	Specific Surface Area
TG	Thermogravimetric Analysis
UV–Vis	Ultraviolet–Visible Spectroscopy
VM	Volatile Matter
XRD	X-ray Diffraction

SYMBOL LIST

C_o	Initial concentration of adsorbate
C_e	Equilibrium concentration of adsorbate
q_e	Adsorption capacity at equilibrium
q_t	Adsorption capacity at time
q_m	Maximum adsorption capacity (Langmuir)
K_L	Langmuir constant (affinity)
K_F	Freundlich constant
n	Freundlich exponent
k_1	Pseudo-first-order rate constant
k_2	Pseudo-second-order rate constant
k_p	Intraparticle diffusion constant
R_L	Separation factor (Langmuir)
V	Volume of solution
M	Adsorbent mass
H	Removal efficiency
t	Time
α	Initial sorption rate (Elovich model)
β	Desorption constant (Elovich model)
C	Boundary layer thickness (Weber–Morris)
R^2	Coefficient of determination
T	Temperature
pH	Negative logarithm of H^+ concentration
λ	Wavelength
ω	Angular velocity
R	Radius
V	Velocity
F	Impact frequency
E	Specific milling energy
P	Power
S	Detachment parameter
D	Interlayer spacing (XRD)

SUMÁRIO

1 INTRODUCTION

The accelerated industrial advancement in recent decades has contributed to a significant increase in the generation of organic and inorganic pollutants, which are often inadequately discharged into the environment. Among these contaminants, synthetic dyes, heavy metals, organochlorine compounds, surfactants, and pharmaceutical residues stand out, posing serious risks to human health and aquatic and terrestrial ecosystems. Industrial sectors such as textiles, forestry, and pharmaceuticals are among the main sources of pollution due to the high-water consumption in their processes and the consequent production of liquid effluents highly concentrated in organic matter and toxic substances (Mergbi et al., 2023; Phiri; Mavinkere Rangappa; Siengchin, 2024; Tavares Vieira et al.,2024). Among the most concerning emerging pollutants are synthetic dyes, widely used in industrial processes due to their chemical stability and resistance to degradation. However, these same characteristics confer high environmental persistence, hindering their removal in conventional effluent treatment systems (Silva; Lima, 2017; Tavares Vieira *et al.*, 2024).

The accelerated industrial advancement in recent decades has contributed to a significant increase in the generation of organic and inorganic pollutants, which are often inadequately discharged into the environment. Among these contaminants, synthetic dyes, heavy metals, organochlorine compounds, surfactants, and pharmaceutical residues stand out, posing serious risks to human health and aquatic and terrestrial ecosystems. Industrial sectors such as textiles, forestry, and pharmaceuticals are among the main sources of pollution due to the high-water consumption in their processes and the consequent production of liquid effluents highly concentrated in organic matter and toxic substances (Mergbi et al., 2023; Phiri; Mavinkere Rangappa; Siengchin, 2024; Tavares Vieira et al.,2024). Among the most concerning emerging pollutants are synthetic dyes, widely used in industrial processes due to their chemical stability and resistance to degradation. However, these same characteristics confer high environmental persistence, hindering their removal in conventional effluent treatment systems (Silva; Lima, 2017; Tavares Vieira *et al.*, 2024).In this scenario, the development of advanced technologies for effluent treatment has gained increasing attention, driven by both public concern and the need to mitigate the environmental impacts resulting from pollution. Various methodologies have been investigated, including absorption, sedimentation, filtration, coagulation, oxidation, and adsorption processes (Silva; Lima, 2017; Tavares Vieira *et al.*, 2024). Although they yield satisfactory results under certain conditions, many of these methods exhibit limitations related to high operational costs, significant energy

consumption, and technical complexity, factors that restrict their large-scale implementation. In contrast, adsorption technology has emerged as a promising alternative, primarily due to its high efficiency in pollutant removal, operational simplicity, and economic feasibility, provided that adsorbent materials with adequate performance and sustainability characteristics are employed (Lehmann; Joseph, 2009; Silva; Lima, 2017; Tavares Vieira *et al.*, 2024).

Various adsorbent materials have been employed in the removal of contaminants present in industrial effluents, particularly those from the textile sector. However, the high cost of conventional adsorbents has driven the search for lower-cost and more sustainable alternatives. In this context, biochars have received increasing attention, as they can be produced from renewable agro-industrial wastes, such as corn cobs, wood sawdust, sugarcane bagasse, coconut mesocarp, among others (Ângelo S., 2017; Lehmann; Joseph, 2009; Phiri; Mavinkere Rangappa; Siengchin, 2024). Generally produced through biomass pyrolysis under controlled atmosphere conditions and at temperatures below 700 °C, biochar constitutes a carbonaceous material with a high surface area and potential for the adsorption of organic compounds. Despite these intrinsic properties, raw biochar may exhibit limited performance against certain pollutants, which has motivated the development of chemical, physical, or mechanical modification strategies capable of enhancing their adsorptive capacity and, consequently, its applicability in effluent treatment systems (Lehmann; Joseph, 2009; Silva; Lima, 2017).

Similarly, clay minerals such as bentonite, kaolinite, and vermiculite, as well as activated carbon, have also emerged as promising adsorbent materials due to their abundance, low cost, high cation exchange capacity, and extensive surface area. However, studies have shown that the adsorptive properties of these materials can be significantly enhanced through physical and chemical modifications, particularly when combined with carbonaceous materials (Yao *et al.*, 2014). In this context, the development of biochar–clay composites have garnered growing interest, as this association combines the structural stability and ion exchange capacity of clays with the high porosity, diversity of functional groups, and adsorption potential characteristic of biochar, resulting in high-performance hybrid materials for application in effluent treatment (Ângelo Silva, 2017; Lehmann; Joseph, 2009; Yao et al., 2014).

Among the different routes for material comminution and modification, high-energy ball milling has established itself as a promising technique, particularly in the field of carbonaceous materials and hybrid composites. This process is based on the application of intense mechanical forces of impact, friction, and shear, capable of promoting the fragmentation of matter to micro and nanometric scales, significantly increasing the surface area available for

adsorption. Beyond particle size reduction, milling induces relevant structural modifications, such as alterations in crystallinity, generation of structural defects, formation of amorphous regions, and an increase in the quantity of active functional groups on the surface (Lopez-Tenllado; Motta; Hill, 2021). These transformations confer distinct properties of reactivity and interaction capacity with contaminants to the materials. Furthermore, as it is considered a clean method that eliminates the need for aggressive chemical reagents and exhibits high reproducibility, high-energy milling has become an attractive alternative to producing high-performance adsorbents and the development of innovative composites with potential application in effluent treatment systems (Lopez-Tenllado; Motta; Hill, 2021; Yao *et al.*, 2014).

Within the broad spectrum of synthetic dyes applied in the industrial sector, reactive dyes stand out, characterized by the presence of azo groups (−N=N−) linked to aromatic systems, which confer high chemical stability and resistance to degradation. Within this class is methylene blue (MB), a cationic dye widely used in sectors such as textiles, printing, and paper. When improperly discharged into water bodies, it triggers significant alterations in the biota, including reduced biodiversity and the emergence of acute and chronic toxicity in affected ecosystems (Shore, 2002; Tavares Vieira *et al.*, 2024). Beyond the environmental impact, methylene blue exhibits potential toxicity to human health. Its high-water solubility, environmental persistence, and resistance to conventional effluent treatments make this dye particularly problematic. For these reasons, MB has been widely adopted as a model molecule in adsorption studies, serving as a reference for evaluating new adsorbent materials due to its representativeness among synthetic organic contaminants and the challenge it poses to traditional treatment methods (Lehmann; Joseph, 2009; Shore, 2002; Tavares Vieira *et al.*, 2024).

Given this scenario, the biomass chosen for this study, derived from the carnauba palm (*Copernicia prunifera*), a species native to the Brazilian Northeast, stands out as a renewable, abundant resource of significant socioeconomic importance for the region. Traditionally, its leaves are used for the extraction of carnauba wax, an activity that supports numerous local families. However, other lignocellulosic structures of the tree, such as the petiole — the segment connecting the leaf to the trunk — remain underexplored, despite their high potential for utilization.

The present work proposes the investigation of the carnauba petiole as a precursor to produce bio-adsorbents aimed at the removal of methylene blue dye from aqueous solutions. To date, there are no reports in scientific literature on the direct application of this material, nor

on the obtention of clay-biochar composites derived from it for bio-adsorption purposes. Thus, this study opens innovative perspectives, contributing to the advancement of knowledge in the field by exploring an underutilized regional biomass and proposing its application in effluent treatment technologies in a sustainable manner aligned with contemporary environmental demands.

2 OBJECTIVES

2.1 General Objectives

To evaluate the potential of the petiole of *Copernicia prunifera* as a feedstock for the synthesis of biochar via slow carbonization and of biochar–bentonite composites modified by high-energy ball milling, aiming at the application of these materials as bioadsorbents for the removal of methylene blue from aqueous media.

2.2 Specific Objectives

- To synthesize biochar from the petiole of *Copernicia prunifera* through slow carbonization.

- To prepare biochar–bentonite composites from the synthesized biochar by high-energy ball milling under different milling times and rotational speeds, and to investigate the influence of these operational parameters on the physicochemical properties and adsorption performance of the produced materials.

- To characterize the *in natura* biomass, the biochar, and the biochar–bentonite composites in terms of their physical, chemical, structural, morphological, and thermal properties using proximate and elemental analyses, particle size distribution, X-ray diffraction (XRD), Fourier-transform infrared spectroscopy (FTIR), scanning electron microscopy coupled with energy-dispersive spectroscopy (SEM/EDS), and thermal analyses.

- To evaluate the adsorption performance of biochar and biochar–bentonite composites for methylene blue removal from aqueous media under batch conditions, and to analyze the adsorption kinetics and equilibrium behavior using appropriate mathematical models.

3 LITERATURE REVIEW

3.1 Study Materials

3.1.1 Biomass

Biomass constitutes any organic matter of plant or animal origin — the stored plant energy is subsequently absorbed by animals within the food chain — which stores solar energy through photosynthetic processes (Bridgwater, 2006; Mergbi *et al.*, 2023). Chemically, it represents a renewable source of complex hydrocarbons, characterized as an agglomeration of organic polymers with significant potential for energy and industrial applications. This definition encompasses a wide range of materials, including agricultural and forest residues, energy crops, organic industrial byproducts, municipal solid waste, and sewage sludge (Morales-Paredes *et al.*, 2023; Nanda *et al.*, 2013).

Its relevance as a sustainable resource stems from its renewable nature and carbon neutrality within the biogenic carbon cycle – in contrast to fossil fuels, whose use results in net atmospheric carbon emissions. When properly managed, biomass represents a sustainable source to produce fuels, petrochemical feedstocks, and valuable chemicals through biochemical or thermochemical pathways (Carvalho, 2022; Lima et al., 2019; Mergbi et al., 2023).

Thus, among the various types of biomasses, lignocellulosic biomass stands out – dry plant material constituted primarily of structural cell walls. Its complex chemical composition derives from two fundamental types of cell walls, as schematized in Figure 1: (Bridgwater, 2006; Xu, R. *et al.*, 2023)

- **Primary Cell Wall:** Mainly composed of cellulose and pectin, it exhibits a less rigid structure and greater permeability.

- **Secondary Cell Wall:** Formed by a complex polymeric matrix designated as lignocellulose, which consists of two main groups of biopolymers: holocellulose (cellulose plus hemicellulose) and lignin:
  - Cellulose (35-50%): A linear glucose polymer that constitutes the skeletal structure of the cell wall.
  - Hemicellulose (20-35%): Heterogeneous polymers of pentose and hexose sugars.
  - Lignin (10-25%): A three-dimensional aromatic polymer that confers rigidity and hydrophobic resistance.

Figure 1 - Diagram of the components of the plant structure: cellulose, hemicellulose and lignin.

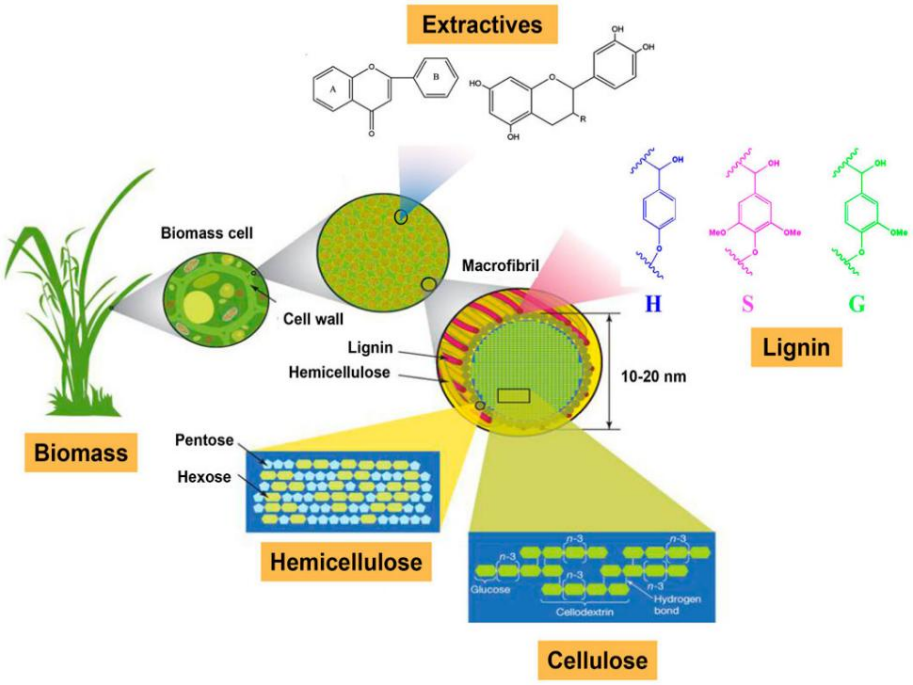

Source: Adapted from *(Huang* et al.*, 2022)*

In addition to the three main constituents, lignocellulosic biomass contains secondary, non-structural components that influence its properties:

- **Organic extractives:** Include lipids, waxes, terpenes, alkaloids, phenolics, and essential oils, responsible for characteristics such as odor, color, and natural resistance.
- **Inorganic components:** Minerals that convert to ash during thermochemical processes.

It is worth emphasizing that the compositional diversity varies significantly among plant species, growth conditions, and plant parts, directly influencing the material's thermal, chemical, and energetic properties (Bridgwater, 2006; Carvalho, 2022).

It is worth emphasizing that the compositional diversity varies significantly among plant species, growth conditions, and plant parts, directly influencing the material's thermal, chemical, and energetic properties (Bridgwater, 2006; Carvalho, 2022).Thus, the abundance and renewability of lignocellulosic biomass — continuously formed through photosynthesis using atmospheric CO_2, water, and solar energy — make it an attractive raw material for thermochemical conversion processes, particularly pyrolysis. A detailed understanding of the composition and structure of lignocellulosic biomass is fundamental for developing efficient conversion processes that enable its transformation into value-added products, contributing to low-carbon economies and the sustainable use of renewable resources (Bridgwater, 2006; Van Loo; Koppejan, 2008).

3.1.1.1 Carnauba Tree (Copernicia prunifera)

The carnauba tree (*Copernicia prunifera*) is a plant species belonging to the *Arecaceae* family and the genus *Copernicia* — a genus comprising 20 (twenty) species in total, whose nomenclature is attributed in honor of the astronomer Nicolaus Copernicus, alluding to the palm's rounded crown shape. However, it is popularly known as the "tree of life", "that which provides all" or "green gold", in addition to the term "Carnauba" meaning the "tree-that-scratches" in the indigenous Tupi language (Alves, 2008; Sousa *et al.*, 2015).

The carnauba tree (*Copernicia prunifera*) is a plant species belonging to the Arecaceae family and the genus *Copernicia* — a genus comprising 20 (twenty) species in total, whose nomenclature is attributed in honor of the astronomer Nicolaus Copernicus, alluding to the palm's rounded crown shape. However, it is popularly known as the "tree of life", "that which provides all" or "green gold", in addition to the term "Carnauba" meaning the "tree-that-scratches" in the indigenous Tupi language (Alves, 2008; Sousa *et al.*, 2015).This palm species is native exclusively to the Brazilian Northeast, located primarily in the states of Ceará, Rio Grande do Norte, and Piauí, and is found in the river valleys of the Caatinga region. Particularly in the state of Ceará, vast carnauba plantations are found in locations ranging from the hinterland to the coast, where the presence of carnauba plantations is directly related to the clay content in the soil (Alves, 2008; Sousa *et al.*, 2015). That is, carnauba typically establishes itself and grows in clay and alluvial soils, which enables it to withstand long periods of water scarcity as well as intense water volumes, in addition to tolerating high saline levels. It is also worth noting that, beyond the mentioned locations, it can be found in the states of Pará, Tocantins, Maranhão, Mato Grosso, and Goiás; however, without wax production (Carvalho, 2022; Lima et al., 2019).

Figure 2 - Carnauba Tree.

Source: Autor.

As shown in Figure 2, the carnauba tree exhibits a straight, cylindrical trunk with an average diameter ranging between 15 (fifteen) and 25 (twenty-five) centimeters. Its distinct foliar architecture is characterized by leaves arranged in a spheroidal pattern, forming a crown with a bluish-green hue – a coloration resulting from the waxy layer coating the leaf blade. Each leaf develops in a fan-like shape, reaching up to 1.5 meters in length, with a pleated surface and a tip segmented into long, erect, and rigid filaments. Furthermore, the attachment of the leaf blade to the trunk occurs via robust petioles that can reach 2 meters in length, notable for the presence of rigid spines located predominantly along the edges, morphologically resembling "cat's claws" (CARVALHO, 2022; Lima *et al.*, 2019; Sousa *et al.*, 2015).

The development of the carnauba follows a median growth pattern of approximately 30 (thirty) centimeters annually, reaching botanical maturity — marked by the first flowering event — between 12 (twelve) and 15 (fifteen) years of age. Under ideal conditions, the species can exceed 10 (ten) meters in height. Its foliar productivity ranges between 45 (forty-five) and 60 (sixty) leaves annually, which represents the primary source of carnauba wax, an economically valuable product extracted from the leaf cuticle (Alves, 2008; Lima *et al.*, 2019; Sousa *et al.*, 2015).

A significant concern for its preservation is observed among those who exploit it, primarily due to its substantial economic importance for the local population, as a large portion depends

on the exploitation of the carnauba for their livelihood. Its main economic value is associated with the harvesting of leaves, a practice carried out during the dry season − typically between July and December. Beyond its economic function, the carnauba palm is also used in urban afforestation and landscaping, reinforcing its cultural and environmental role in the regions where it occurs (Alves, 2008; Sousa *et al.*, 2015).

Thus, among the by-products of the carnauba palm, the following parts are classified: (Alves, 2008; Carvalho, 2022; Sousa et al., 2015)

I. **Straw:** It stands out as one of the most important, after the wax, especially in the artisanal context of the Northeast. Its preparation is carried out manually, from collection to transformation into braids, mats, and other artifacts. The straw is a raw material for the manufacture of a wide diversity of utensils, such as hats, baskets, bags, trunks, brooms, nets, mats, and rustic coverings, in addition to modern decorative and utilitarian articles like fruit bowls, lampshades, placemats, and coasters.
II. **Wax**: Carnauba wax, internationally known as "carnauba wax", represents the most commercially recognized product of this plant. Originating from the powder that coats the leaves, especially the younger ones, the wax constitutes a physiological adaptation of the plant to semi-arid environments, functioning as a barrier against water loss through transpiration, in addition to reducing leaf heating and providing protection against pathogens.
III. **Dewaxed Leaf:** This is a residue generated after the extraction of wax from the leaf surface. Studies conducted by Embrapa (the Brazilian Agricultural Research Corporation) demonstrate that its agricultural application favors the development of orchards, providing greater uniformity and precocity in plant growth. This efficiency stems from the rapid decomposition of the dewaxed leaf, which contributes to soil moisture maintenance, reduction of surface temperature, and increased fertility.
IV. **Petiole:** Derived from the carnauba leaf, it presents traditional and contemporary uses that expand the species' utilization potential. Traditionally, the dried petiole was used as a support for sharpening agricultural tools, but it has now become established as a raw material for the artisanal production of furniture, toys, basketry, decorative pieces, and even construction elements. Its versatility makes it a sustainable and recyclable alternative, capable of stimulating artisans’ creativity and fostering income generation in local communities.

Thus, it is observed that the carnauba tree plays a significant role in the socioeconomic dynamics of the Northeast, serving as a source of products ranging from traditional uses, linked to regional culture, to high-value-added industrial applications on a global scale. The integral utilization of the palm, associated with sustainable management practices, ensures not only the conservation of the ecosystems where it occurs but also the perpetuation of a cultural, economic, and environmental heritage of singular relevance to the Northeast region.

3.1.2 Biochar

3.1.2.1 Definition and Thermochemical Processes

Biochar can be defined as a type of carbonaceous biomaterial widely used by humanity, produced primarily through thermochemical processes, such as carbonization or pyrolysis, which utilize abundant and sustainable organic biomass as raw material. This material is a carbon–rich compound, economically viable, and obtained from the thermal decomposition of lignocellulosic biomass in environments with little or no oxygen at temperatures below 700 °C, which distinguishes biochar from other carbonized materials (Conti *et al.*, 2016; Elnour *et al.*, 2019; Guida *et al.*, 2021).

Among thermochemical conversion technologies, gasification and combustion are mainly oriented towards energy generation, and liquefaction toward liquid fuel production. Pyrolysis stands out as the most widely investigated and suitable process for obtaining biochar due to its ability to tailor physicochemical properties relevant for environmental applications (Guida *et al.*, 2021). In pyrolysis, lignocellulosic biomass undergoes thermal decomposition to produce a solid carbonaceous fraction (biochar), bio-oil, and non-condensable gases, with the proportions and properties of these products being strongly influenced by processing conditions (e.g., heating rate, temperature, and residence time) (Elnour *et al.*, 2019; Lehmann; Joseph, 2009).

Figure 3 schematizes the main thermochemical technologies, primary products, processing technologies, and their secondary products.

Figure 3- Diagram of the main thermochemical technologies, primary products, processing technologies and their secondary products.

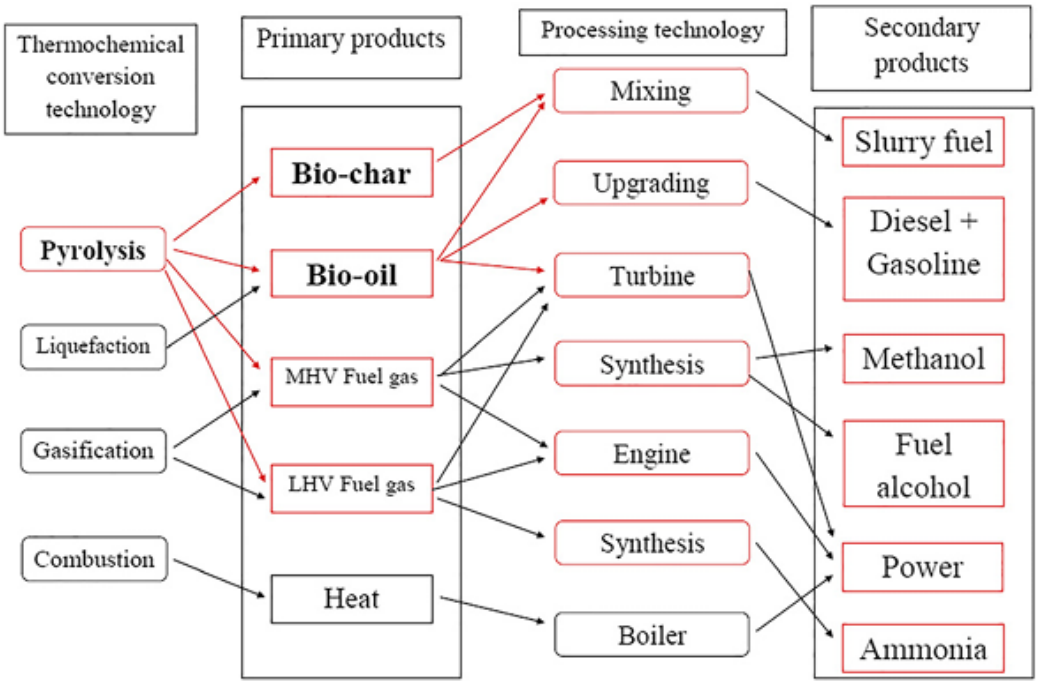

Source: Adapted from *(Guida* et al.*, 2021).*

It should be noted that biochar can be produced either directly by the pyrolysis of biomass or as a by-product of other thermochemical processes; however, the main production process combines the factors of simplicity, accessibility, and effectiveness, since pyrolysis stands out as an accessible and efficient technology for converting biomass into biochar, transforming organic waste into a stable, carbon-rich product.

According to the operational conditions and product distribution, pyrolysis processes can be classified into four main types: (Conti *et al.*, 2016; Guida *et al.*, 2021; Van Loo; Koppejan, 2008)

I. **Slow pyrolysis:** Slow pyrolysis is characterized by low heating rates (typically $0.1-1°C \cdot s^{-1}$), long solid residence times ranging from several minutes to hours, and moderate temperatures generally between 300 and 550°C. These conditions favor the maximization of solid yield, resulting in biochars with high carbon content, enhanced aromaticity, and relatively preserved oxygen−containing functional groups. Consequently, slow pyrolysis is widely employed when the primary objective is biochar production for applications such as soil amendment, carbon sequestration, and adsorption of contaminants.

II. **Fast pyrolysis:** Fast pyrolysis operates at significantly higher heating rates (> 10 °C · s^{-1}) and short vapor residence times at temperatures typically around 450–550°C. Under these conditions, biomass is rapidly decomposed, favoring the formation of liquid products (bio−oil), while the yield of biochar is comparatively lower.

III. **Intermediate pyrolysis:** Intermediate pyrolysis represents a transitional regime between slow and fast pyrolysis, combining moderate heating rates and intermediate residence times. This process leads to a more balanced distribution of solid, liquid, and gaseous products.

IV. **Flash pyrolysis:** Flash pyrolysis is conducted under extremely high heating rates (often exceeding 1000°C · s^{-1}) and very short vapor residence times, typically less than 0.5s. This process is designed primarily to maximize the rapid release of volatiles, favoring the production of gases and condensable vapors, while generating minimal amounts of biochar.

The conditions of pyrolysis not only determine product distribution but also profoundly affect the physicochemical properties of biochar, which in turn govern its effectiveness as an adsorbent. Slow pyrolysis at moderate temperatures generally yields higher carbon content and greater aromaticity, enhancing structural stability and resistance to degradation, while preserving functional groups containing oxygen that contribute to polarity and surface reactivity. Temperature influences surface area, pore structure, and functional group distribution: increasing temperature often increases surface area and porosity but may reduce the density of oxygen-containing groups, which are important for interactions with polar pollutants (Demirbaş, 2000; Lehmann; Joseph, 2009; Xu, Y.; Chen, 2013).

The adsorptive interactions between biochar and aqueous contaminants, such as synthetic dyes and heavy metals, are closely linked to these thermochemically induced features. Functional groups such as carboxyls and hydroxyls on the biochar surface can facilitate electrostatic interactions, hydrogen bonding, and complexation, while high surface area and well-developed pore structures improve physical adsorption mechanisms such as pore filling and π−π stacking with aromatic pollutants. For example, studies show that oxygen-containing functional groups retained at lower pyrolysis temperatures enhance the adsorption of ionic species, whereas higher temperatures favor structural graphitization that may improve π−π interactions with organic molecules (Demirbaş, 2000; Lehmann; Joseph, 2009; Xu, Y.; Chen, 2013).

3.1.2.2 Properties

Originating from renewable and low-cost sources, it is characterized as a "carbon–negative" material, capable of contributing to the mitigation of greenhouse gases through carbon sequestration, while simultaneously promoting direct benefits to agricultural management, such as improved soil fertility and quality (Conti *et al.*, 2016). These characteristics position biochar as a material consistent with circular economy principles and environmental impact mitigation strategies, offering a sustainable alternative in response to the growing depletion of fossil resources (Lehmann; Joseph, 2009; Xu, Y.; Chen, 2013).

Although it shares structural similarities with charcoal and other carbonaceous materials, biochar is distinguished by the specific purpose of its production: application in agricultural soils aimed at increasing productivity, enhancing carbon storage, and improving the quality of percolated water (Lehmann; Joseph, 2009; Xu, Y.; Chen, 2013).

Beyond its established use as a soil amendment and adsorbent, biochar has attracted significant interest in research focused on advanced applications. Recent studies point to its utilization in energy conversion and storage systems, such as carbon fuel cells, catalytic processes, and emerging environmental remediation technologies (Elnour *et al.*, 2019). This versatility stems not only from its porous structure and high chemical stability but also from its capacity to act simultaneously as a carbon sequestration agent and as a base material for innovative energy solutions (Lehmann; Joseph, 2009; Xu, Y.; Chen, 2013).

Accordingly, the physicochemical characteristics of biochar are inherently complex and are governed by several parameters, including the nature of the precursor material, the carbonization route, pyrolysis temperature, heating rate, and residence time. These variables strongly affect the structural and chemical attributes of the final product and, consequently, determine its suitability for a wide range of applications, including agriculture, soil improvement, and advanced materials development (Lehmann; Joseph, 2009; Xu, Y.; Chen, 2013).

3.1.3 Clay and Clay Minerals

The conceptualization of the term "clay" exhibits significant interdisciplinary variations, with no single, universally accepted definition currently existing, reflecting distinct scientific and applied perspectives. (Qi *et al.*, 2023) Although there is no universal consensus on its definition, a convergence is observed in fundamental aspects that transcend disciplinary boundaries. Thus, the terminological complexity stems not only from conceptual differences

but also from the multiple properties and applications of these materials in science and industry (Bergaya; Lagaly, 2006; Vithanage *et al.*, 2023).

The Association Internationale pour l'Étude des Argiles (AIPEA) reinforces this conception by defining clay as a material predominantly composed of fine-grained minerals that exhibits plasticity at appropriate moisture contents and hardens when dried or fired (Arif *et al.*, 2021; Steinmetz, 2007). However, the definition proposed by AIPEA, although widely referenced, presents limitations by failing to encompass fundamental aspects such as: (i) variation in chemical composition, (ii) degree of crystallinity, and (iii) presence of non-phyllosilicate components (Abollino *et al.*, 2003; Qi *et al.*, 2023).

Comprehensively, clay can be defined as a natural earthy material of fine granulometry, which exhibits plasticity when moistened and hardening when subjected to drying or heating. When pulverized and mixed with enough water, it becomes plastic and, upon drying, becomes hard and consistent. This operational definition encompasses two essential dimensions: (Abollino *et al.*, 2003; Bergaya; Lagaly, 2006; Vithanage *et al.*, 2023)

I. **Compositional:** Dominant presence of phyllosilicate minerals (clay minerals).
II. **Behavioral:** Specific rheological properties (plasticity and hardening).

However, several authors consider that all clays are constituted of extremely small crystalline particles of a limited number of minerals known as clay minerals, which exhibit plasticity and possess a layered (phyllosilicate) structure (Bergaya; Lagaly, 2006). Although particle size is an important factor in all existing definitions of clay, there is no generally accepted upper limit. It is noteworthy that some fields of science have defined a maximum size for clay particles (Abollino *et al.*, 2003; Li *et al.*, 2022).

Similarly, the concept of a clay mineral presents certain definitional difficulties due to its complexity and breadth. In general terms, it can be understood as a class of hydrated phyllosilicates that may contain other elements such as iron, calcium, sodium, and potassium in a layered crystalline structure, constituting the fine-grained fraction of rocks, sediments, and soils. Unlike the term "clay", this designation is not restricted to the material's natural origin, meaning that clay minerals can also be synthesized in the laboratory. Furthermore, grain size is not a determining criterion for their classification, which allows phyllosilicates at different scales — including macroscopic mica, vermiculite, and chlorite — to be considered clay minerals (Bergaya; Lagaly, 2006; Li *et al.*, 2022; Qi *et al.*, 2023). The absence of terminological consensus among different scientific areas does not reduce the relevance of these materials; on the contrary, it highlights their structural complexity and versatility, characteristics that sustain

their continued interest as an object of study and broaden their prospects for new technological applications (Vithanage *et al.*, 2023).

Their intrinsic properties — such as the regular organization of the silica-alumina network, high specific surface area, cation exchange capacity, high surface electronegativity, and structural stability that favors catalyst regeneration — make them highly promising materials for environmental applications, particularly in pollutant remediation (Bergaya; Lagaly, 2006; Qi *et al.*, 2023). Among the main cations present at exchange sites, sodium (Na^{+}), potassium (K^{+}), magnesium (Mg^{2+}), and calcium (Ca^{2+}) stand out. The surface charge of clay minerals results from the hydrolysis of Si−OH or Al−OH bonds in the crystalline network. This charge can vary between positive and negative depending on the medium's pH and the structural characteristics of the silica, directly influencing its reactivity. Another relevant aspect is the ease of particle separation after adsorption processes, which reinforces the applicability of clay-based modifications in environmental decontamination strategies (Abollino *et al.*, 2003; Li *et al.*, 2022).

Structurally, clay minerals are formed by the association of silicate tetrahedral sheets and octahedral hydroxide sheets. When a tetrahedral sheet and an octahedral sheet are juxtaposed, a so-called 1:1 clay is formed (e.g., kaolinite and serpentine). In 2:1 clays, an octahedral sheet is intercalated between two tetrahedral sheets (examples: illite, smectite, vermiculite, and montmorillonite) (Arif *et al.*, 2021; Bergaya; Lagaly, 2006). In the case of 2:1:1 clays, an additional magnesium hydroxide sheet is inserted into the interlayer space, a characteristic of chlorite. Beyond structural differences, the classification of clay minerals also considers aspects such as the type of substituting metals, the quantity and nature of exchangeable ions, the Si/Al ratio, and the impurities present within their layers (Qi *et al.*, 2023; Vithanage *et al.*, 2023).

Figure 4 - Silicate tetrahedral sheets and octahedral hydroxide sheets.

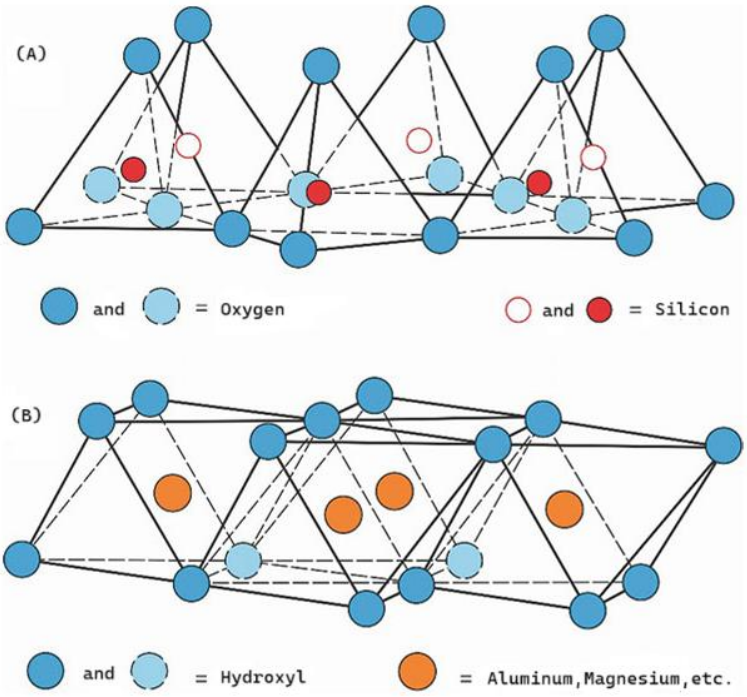

Source: Adapted from *(Vithanage* et al.*, 2023)*.

3.1.3.1 Bentonite Clay

Smectites constitute an important group of clay minerals, subdivided mainly into trioctahedral saponites and dioctahedral montmorillonite. Within this group, bentonite stands out, also referred to as a sedimentary clay, widely recognized for its unique water retention capacity (Vithanage *et al.*, 2023). Thus, bentonite is a plastic clay of high softness, composed predominantly of montmorillonite, a 2:1 type phyllosilicate mineral formed by ultrafine particles. In its purest form, bentonite can contain up to 98% montmorillonite, a characteristic that enhances its functional properties (Arif *et al.*, 2021; Bergaya; Lagaly, 2006).

Montmorillonite has a structure consisting of two tetrahedral layers of (SiO_4) intercalated by an octahedral layer of $Al(OH)_6$, forming sheets with an approximate thickness of 14Å. This arrangement generates a negatively charged surface, compensated by interlayer cations resulting from isomorphous substitutions, such as the exchange of Al^{+3} for Mg^{2+} or Fe^{2+} and of Si^{4+} for Al^{3+}, as shown in Figure 5. (Arif *et al.*, 2021; Bergaya; Lagaly, 2006)

Figure 5 - The structure of the clay mineral montmorillonite.

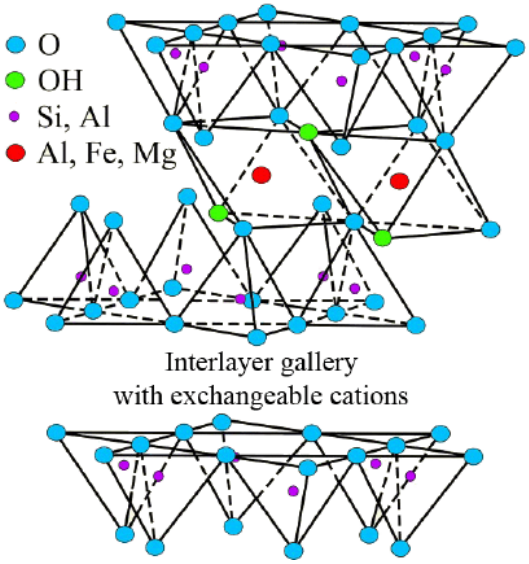

Source: Adapted from (Steinmetz, 2007)

From a compositional standpoint, bentonites can be classified according to the predominant cation in their structure, such as potassium (K), sodium (Na), calcium (Ca), or aluminum (Al) (Arif *et al.*, 2021; Vithanage *et al.*, 2023).

These structural properties result in a material with high specific surface area, chemical and mechanical stability, high cation exchange capacity (CEC), and a tendency to retain water molecules in interlayer sites (Abollino *et al.*, 2003; Vithanage *et al.*, 2023). The adsorptive performance of the clay is directly related to its layered structure and the chemical characteristics of its pores. For industrial applications, the most used varieties correspond to sodium, calcium, and potassium bentonites, each exhibiting specific properties that govern their technological application (Arif *et al.*, 2021; Li *et al.*, 2022).

3.1.4 Dyes

3.1.4.1 Definition

Global production aims to meet the commercial demand for colors, wear resistance, and other requirements of synthetic dyes, producing approximately 800,000 tons annually. Among these, about 2,000 varieties are specifically designed for the textile industry, out of a total of 10,000 types produced industrially (Euranio; Aguiar, 2012). These compounds find application in various industrial sectors, including pharmaceuticals, cosmetics, plastics, photography, paper, and food. The textile industry stands out as the main consumer, characterized by using substantial volumes of water during washing and dyeing processes, resulting in effluents of considerable chemical complexity (Carvalho, 2015; Euranio; Aguiar, 2012).

It is worth mentioning, from a conceptual standpoint, that dyes and pigments constitute classes of compounds that impart or modify the coloration of materials when applied. The traditional distinction was based on water solubility — dyes being soluble and pigments being insoluble — whereby pigments required dispersion in the medium to be colored (Shore, 2002; Tavares Vieira et al.). However, the development of new materials has demanded more sophisticated classification criteria, incorporating aspects such as chemical nature, rheological behavior, and interaction mechanisms with substrates (Ramola et al., 2022; Tavares Vieira et al.).

Thus, modern dyes exhibit notable technical properties, including high stability against light radiation, thermal variations, detergent action, and microbial activity. These characteristics, although desirable for industrial applications, represent significant environmental challenges due to their persistence in aquatic ecosystems and the complexity of the chemical substances employed (sequestering agents, dispersing agents, salts, acids, and bases) (Ângelo Silva, 2017; Carvalho, 2015).

3.1.4.2 Classification

Dyes constitute a class of organic compounds characterized by their capacity for selective absorption of electromagnetic radiation in the visible region (400 − 700 nm), endowing them with their coloring property (Silva; Lima, 2017; Tavares Martins, 2012). From a molecular perspective, these compounds present two fundamental structural units: (Carvalho, 2015; Tavares Vieira *et al.*, 2024)

I. The chromophore group, responsible for light absorption and the consequent chromatic manifestation, and
II. The auxochrome groups (also called “auxiliary” groups), which modulate the dyeing properties, colorimetric intensity, and promote specific interactions with substrates.

Thus, among the main chromophore groups, azo (−N=N−), anthraquinone, and nitro structures stand out, with azoic compounds being particularly significant due to their industrial ubiquity and chromatic versatility (Carvalho, 2015; De Costa; Furmanski; Dominguini, 2015).

The chemical classification system identifies 26 distinct categories based on fundamental molecular structure, whereas the application-based classification recognizes 20 functional categories. This dual perspective reflects the inherent complexity in systematizing these

compounds, whose structural and functional diversity challenges one-dimensional classification schemes (Ahmad *et al.*, 2020; Euranio; Aguiar, 2012).

From a regulatory standpoint, CNNPA Resolution No. 44/1977 from the Ministry of Health establishes a conceptual tripartite framework based on origin and chemical nature: (De Costa; Furmanski; Dominguini, 2015; Leal *et al.*, 2012; Shore, 2002)

- **Natural organic colorant:** Originating from plant or animal sources, isolated through appropriate technological processes.
- **Synthetic organic colorant:** Entirely produced by organic synthesis.
- **Artificial colorant:** A synthetic colorant not identified in natural products.

Regarding structural characteristics, modern synthetic dyes exhibit molecular architectures of remarkable complexity, often involving up to 500 interactive steps during their synthesis. Their colorimetric properties derive from electron conjugation enabled by chromophore groups (nitro, nitroso, azo, carbonyl), intensified or modified by the presence of auxochrome groups (amino, hydroxyl, sulfonic, halogens, alkyl, and alkoxy groups) (Shore, 2002; Tavares Vieira *et al.*, 2024). This molecular combination confers upon them not only the capacity for selective light absorption but also superior fixation properties, including wash speed and photostability (De Costa; Furmanski; Dominguini, 2015; Leal *et al.*, 2012).

In the specific context of textile applications, synthetic dyes can be categorized according to their ionic behavior and affinity for substrates: (Ramola *et al.*, 2022; Shore, 2002)

- **Anionic dyes:** Include direct, acid, and reactive dyes.
- **Cationic dyes:** Represented mainly by basic dyes.
- **Non-ionic dyes:** Constituted by disperse dyes.

3.1.4.3 Methylene Blue

Methylene blue is a cationic organic dye widely used in various industrial sectors, notably in the textile industry, printing processes, and photographic procedures. Its chemical structure corresponds to methylthioninium chloride ($C_{16}H_{18}N_3SCl$), with a molar mass of 319.85 g·mol^{-1}, as shown in Figure 6 (Leal et al., 2012; Carvalho, 2015; Tavares Vieira et al., 2024).

Figure 6 - Chemical structure of Methylene Blue.

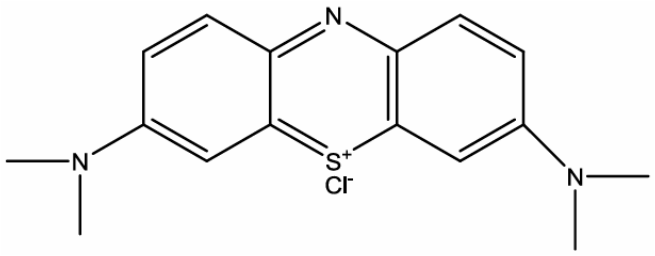

Source: Adapted from (Tavares Martins Filho, 2012).

It is a heterocyclic aromatic compound of the phenothiazine class, characterized as a basic dye soluble in water and alcohol, although it exhibits low solubility under certain conditions. Its characteristic absorption occurs in the UV-visible region, with detection around 650 nm, which contributes to its frequent use as an indicator in chemical reactions (Euranio; Aguiar, 2012; Leal *et al.*, 2012).

From a classification standpoint, methylene blue falls within the class of reactive dyes, which possess functional groups of the −N=N− type linked to aromatic systems in their structure, responsible for their higher chemical stability. More broadly, it also integrates the category of azo dyes, synthesized from aromatic amines. These constitute one of the most relevant and widely applied groups in sectors such as textile, leather, paper, pharmaceutical, and food (Euranio; Aguiar, 2012; Ramola *et al.*, 2022). However, they present disadvantages such as resistance to aerobic degradation and the generation of toxic byproducts, such as carcinogenic aromatic amines, when subjected to anaerobic biodegradation processes. In this context, methylene blue stands out both for its broad industrial applicability and its role as a marker in environmental and chemical investigations (Leal et al., 2012; Tavares Vieira et al.,2024).

Beyond its industrial value, methylene blue is widely used in scientific research as a model molecule for adsorption studies, due to its high affinity for solid surfaces and the ease of spectrophotometric monitoring in aqueous solutions. This characteristic makes it relevant for assessing organic pollutant removal processes, particularly in effluent treatment systems.

3.2 Transformation Processes

3.2.1 High Energy Ball Milling

High-energy milling constitutes a mechanical processing technique characterized by the intensive application of energy through impacts and friction between grinding balls and the mill walls. This methodology stands out for its ability to promote structural and compositional

transformations in diverse materials via the transfer of kinetic energy from the balls to the processed particles (Leonel *et al.*, 2014; Lopez-Tenllado; Motta; Hill, 2021).

The fundamental process of high-energy milling is based on successive cycles of particle welding and fracture, generated by high-energy impacts in controlled environments (Kumar *et al.*, 2020). Initially conceived as an exclusively dry process to produce composite metal powders, the technique has expanded its scope to include wet processing and a diverse range of materials. This evolution has demanded conceptual revisions, proposing a more comprehensive definition that emphasizes the production of powder alloys with a heterogeneous microstructure (Araújo *et al.*, 2003; Lopez-Tenllado; Motta; Hill, 2021).

Thus, over the last thirty (30) years, high-energy milling has demonstrated remarkable versatility in processing diverse materials, including: (Leonel *et al.*, 2014; Lopez-Tenllado; Motta; Hill, 2021)

- Powdered metal alloys
- Composite materials
- Intermetallic compounds
- Ceramic systems
- Carbonaceous materials

It should be emphasized that this technique positions itself as a sustainable alternative to conventional methods, as it eliminates the need for aggressive chemical reagents and consumes less energy compared to technologies such as laser ablation, microwave pyrolysis, chemical precipitation, among others (Lopez-Tenllado; Motta; Hill, 2021). Its potential for producing nanostructured materials — both nanocrystalline and amorphous — has driven applications in mechanical synthesis and the activation of solid-state reactions (Leonel *et al.*, 2014; Mayer-Laigle *et al.*, 2018).

The energy transmitted during the process induces significant structural modifications in carbonaceous materials, including: (Kumar *et al.*, 2020; Lopez-Tenllado; Motta; Hill, 2021)

- Reduction in particle size
- Increase in pore volume
- Modifications in surface chemical composition

Thus, these alterations result in the enhancement of adsorptive properties, which are particularly relevant for environmental applications such as the removal of dyes and heavy metals from industrial effluents. Recent studies demonstrate that biochars subjected to high-

energy milling exhibit significantly superior adsorption capacities compared to the original materials (Leonel *et al.*, 2014; Mayer-Laigle *et al.*, 2018).

3.2.1.1 Equipment and Operation

High-energy ball mills are specialized equipment characterized by their capacity to apply intense mechanical forces through impacts and shear. Among the various existing machinery, planetary ball mills stand out due to their compact configuration and versatility, being particularly suitable for laboratory-scale operations (Leonel *et al.*, 2014). Their operating principle is based on a distinct planetary movement: the grinding jar, containing the material to be processed and the grinding balls, rotates eccentrically on a sun disk that rotates in the opposite direction; that is, the equipment support rotates clockwise, while the grinding container rotates counterclockwise (Kumar *et al.*, 2020; Lopez-Tenllado; Motta; Hill, 2021).

Figure 7 - Ball milling mechanism.

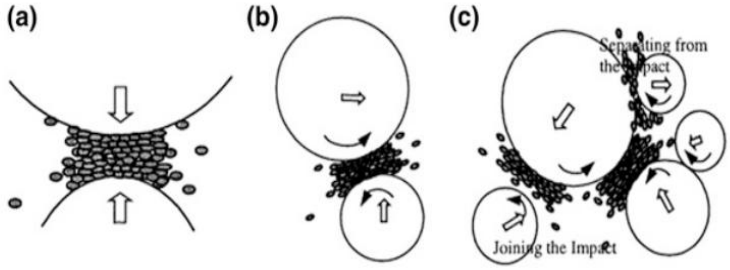

Source: Adapted from (Kopp Alves; Bergmann; Berutti, 2013)

This relative motion generates complex centrifugal forces that result in the combined application of high-energy impacts and frictional forces, creating ideal dynamic conditions for intensive grinding processes (Kumar *et al.*, 2020; Leonel *et al.*, 2014).

Thus, the fundamental process involves the conversion of kinetic energy from the moving balls into mechanical energy applied to the powder charge. This energy transfer promotes the rupture of chemical bonds and the progressive reduction of particle size through multiple mechanisms: (Kumar *et al.*, 2020; Leonel *et al.*, 2014; Lopez-Tenllado; Motta; Hill, 2021)

i. Application of compressive and shear mechanical stresses.
ii. Generation of crystalline defects and atomic displacements.
iii. Activation of mass and energy transfer processes.
iv. Modification of the materials' lattice structure.

Considering the afore-mentioned mechanisms, efficiency is intrinsically related to the magnitude and frequency of impacts, which are determined by the system's operational parameters, as shown in Table 1. The efficiency and outcomes of high-energy milling critically depend on multiple interrelated parameters.

Table 1 - Influence of high-energy ball milling parameters on the structural, chemical, particle size, and thermal properties of biochar and biochar–bentonite composites, correlated with DRX, FTIR, particle size distribution, and TG/DTG/DTA analyses. Source: Adapted from *(Araújo* et al*., 2003; Kumar* et al*., 2020; Lopez-Tenllado; Motta; Hill, 2021)*

Parameter	Influence on Milling Process	Effect on Biochar	Effect on Biochar–Bentonite Composite	Related Characterization Techniques
Milling Time	Controls degree of particle refinement and structural disorder	Progressive particle size reduction; possible increase in surface defects; partial disruption of aromatic ordering	Enhanced dispersion of bentonite layers into biochar matrix; improved interfacial contact	Particle size distribution; DRX (peak broadening); FTIR (functional group variation)
Rotation Speed	Determines impact energy and collision frequency	Higher speeds increase amorphization and surface activation	Promotes exfoliation or delamination of bentonite; stronger biochar–clay interaction	DRX (basal spacing shifts); FTIR (Si–O–C interactions); TG
Ball−To−Powder Mass Ratio (BPR)	Controls energy transfer efficiency	Higher BPR increases fragmentation and defect density	Improves clay dispersion but may induce excessive structural collapse if too high	Particle size analysis; DRX crystallinity; DTG profiles
Ball Diameter and Number	Influences impact force distribution	Larger balls → higher impact → faster size reduction	Balanced distribution favors homogeneous composite formation	Particle size distribution; DRX intensity variation
Processing Temperature	Affects diffusion and possible mechanochemical reactions	Excessive temperature may alter surface oxygen groups	May induce mechanochemical bonding between silicate layers and carbon matrix	FTIR (bond formation); TG/DTA (thermal transitions)
Nature of the Milling Medium	Determines dominant mechanisms (impact vs. friction)	Can influence oxidation or surface functionalization	May promote surface activation of both phases	FTIR; TG mass-loss variation
Processing Atmosphere	Controls concomitant chemical reactions	Inert atmosphere preserves carbon structure	Reactive atmosphere may favor interfacial bonding	FTIR; DRX structural stability; TG oxidation onset

Source: Autor.

The optimization of these parameters requires a systematic approach, considering the specific properties of the starting material and the processing objectives. The complex interaction between these factors determines not only the kinetics of size reduction but also the induced structural and chemical transformations, making parametric control essential for the reproducibility and efficacy of the process.

3.2.2 Adsorption Mechanisms

Adsorption is a mass transfer process in which a substance present in a fluid, whether liquid or gaseous, accumulates on the surface of a solid phase, termed the adsorbent. The retained species is called the adsorbate, while the release of this substance from the surface is named desorption. This physicochemical phenomenon occurs since atoms located on the surface of a solid exhibit resultant forces distinct from those observed within the bulk structure (Ângelo Silva, 2017; Tavares Vieira et al.). This difference generates surface energy, responsible for attracting and retaining molecules from the fluid phase in contact with the adsorbent. During the process, different interactions may be involved, such as hydrogen bonding, dipole-dipole interactions, van der Waals forces, electrostatic interactions, and even covalent bonds, depending on the nature of the adsorbent and adsorbate (Ângelo Silva, 2017; Silva; Lima, 2017; Tavares Martins Filho, 2012).

Figure 8 presents a general schematization of the phenomena that can be encountered in the adsorption process.

Figure 8 - General diagram of the factors present in the adsorption process.

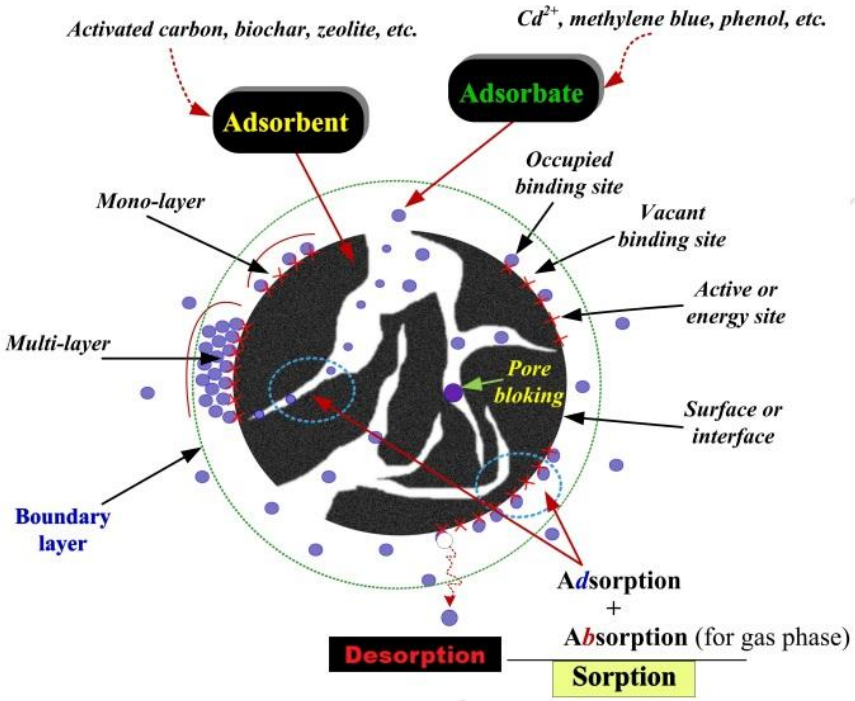

Source: Adapted from (Ângelo Silva, 2017)

The adsorption process can be reversible, allowing modifications in parameters such as temperature, pressure, or pH to promote the release of the adsorbate, enabling adsorbent regeneration and contributing to the reduction of operational costs. In practical terms, the efficiency of this mechanism is directly related to the structural characteristics of the adsorbent material (Euranio; Aguiar, 2012). Porous solids are generally the most effective, as they exhibit a high available surface area for the accumulation of molecules at the solid-fluid interface. Thus, the greater the surface area per unit mass, the higher the retention capacity and, consequently, the more efficient the adsorption process will be (Ângelo Silva, 2017; De Costa; Furmanski; Dominguini, 2015).

Among the different processes employed for the removal of dyes from industrial effluents, adsorption stands out by combining low operational cost and high removal efficiency. Another advantage of this method is the fact that, in many cases, it is not a destructive process, allowing for the recovery of the dye without compromising its chemical identity (Carvalho, 2015; Tavares Vieira *et al.*, 2024). Among the materials commonly used as adsorbents, activated carbon is one of the most efficient and is widely employed in wastewater treatment. However, its large-scale application faces limitations, as the losses occurring during the adsorbent regeneration stage increase process costs. Furthermore, because its surface exhibits a positive

charge, its effectiveness in the adsorption of cationic dyes becomes restricted (Ângelo Silva, 2017; Silva; Lima, 2017).

3.2.2.1 Adsorption by Clay-Biochar Composite

Clay-biochar composites are hybrid materials in which lamellar or fibrous minerals — such as bentonite, montmorillonite, kaolinite, or palygorskite — are integrated with biochar produced by the controlled pyrolysis of biomasses (Vithanage *et al.*, 2023; Yang *et al.*, 2020). This combination unites the high specific surface area, porosity, and oxygenated functional groups of biochar with the high cation exchange capacity, expandable interlayer structure, and chemical stability of clays, resulting in mechanically more stable adsorbent matrices with complementary active sites. Recent reviews highlight these composites as versatile materials for aqueous and soil remediation, demonstrating consistent performance against metal ions, dyes, pharmaceuticals, and nutrients, often outperforming the isolated components (Elnour *et al.*, 2019; Yao *et al.*, 2014).

Thus, the interest in these materials also stems from practical factors: low cost and wide availability of precursors (lignocellulosic wastes and natural clays), ease of synthesis (mixing/coating, intercalation, thermal or chemical activation, and functionalization), recoverability (including magnetic recovery when doped), in addition to high performance (efficiencies > 90–98% reported for various pollutants) and good applicability under real conditions. Reference works on biochar and composite reviews show that the clay-biochar synergy increases pore accessibility, site diversity, and adsorbent stability, enabling continuous systems and reuse after desorption cycles (Ângelo Silva, 2017; Silva; Lima, 2017; Tavares Martins Filho, 2012).

Regarding the adsorption mechanism for organic compounds (for example, dyes, antibiotics, and pesticides), the following interactions dominate: (Silva; Lima, 2017; Tavares Martins Filho, 2012)

i. π–π and π–π* interactions between aromatic domains of the biochar and contaminant rings;
ii. electrostatic attraction (positive/negative charge adjustable with pH and modification).
iii. hydrogen bonding.
iv. hydrophobic partitioning into micro/mesopores.
v. pore-filling.

The clay fraction contributes with specific sorption at edge sites, possible intercalation, and, when organophilized or functionalized, increases affinity for low-polarity molecules; collectively, the composite provides a landscape of heterogeneous sites that enhances capacity and selectivity (Bergaya; Lagaly, 2006; Qi *et al.*, 2023).

Thus, the critical variables governing the adsorption process performance are presented in Table 2.

Table 2 - Influence of operational variables on dye adsorption by clay–biochar composites and their relationship with key physicochemical properties of the adsorbent. Source: Adapted from (Ângelo Silva, 2017; Silva; Lima, 2017; Tavares Martins Filho, 2012)

Variable	Influence on the Adsorption Process	Correlation with Composite Properties
Solution pH	Controls the surface charge of the composite and the speciation of the pollutant. Crucial for cationic dyes like methylene blue.	Surface functional groups of biochar (–COOH, –OH) and the permanent negative charge of bentonite layers determine protonation/deprotonation behavior, influencing adsorption affinity.
Ionic strength and competing ions	Dissolved ions (Na^+, Ca^{2+}, Cl^-, etc.) can compete with the dye for active sites, reducing the adsorption capacity.	Clay cation-exchange capacity (CEC) and biochar surface charge regulate competition between dye cations and inorganic ions (Na^+, Ca^{2+}, etc.).
Adsorbent dose	Increasing dose raises the number of available adsorption sites but may reduce adsorption capacity per unit mass due to site overlaps or aggregation.	Surface area, pore volume, and dispersion of clay particles within the biochar matrix determine the effective accessibility of adsorption sites.
Clay: biochar ratio	Determines adsorption capacity and selectivity by balancing ion-exchange capacity and porous carbon adsorption mechanisms.	Bentonite contributes layered structure and ion-exchange sites, while biochar provides porosity and aromatic surfaces enabling π–π interactions with dye molecules.
Contact time and mixing regime	Influences adsorption kinetics. Generally, follows a pseudo-second-order model; efficient agitation improves diffusion and solute-surface contact.	Pore structure of biochar and interlayer spacing of bentonite influence external mass transfer and intraparticle diffusion.
Temperature	Affects the thermodynamics of sorption: can indicate endothermic or exothermic processes and influences the interaction energy.	Thermal stability and surface functional groups of the composite influence adsorption energy and dye–surface interactions.
Initial dye concentration	Determines the initial adsorption rate and equilibrium; influences the isotherm type (Langmuir, Freundlich, Temkin, etc.).	Surface heterogeneity and pore structure of the composite control saturation behavior and adsorption isotherm type (e.g., Langmuir or Freundlich).
Dissolved organic matter (DOM)	Can compete for active sites and block pores, reducing efficiency in real water matrices.	Biochar microporosity and clay interlayer spaces may become partially blocked, reducing effective adsorption capacity.

Composite modification history	Chemical activation, surface functionalization, doping, or magnetization alter affinity and recoverability.	Structural defects, new functional groups, and improved clay dispersion increase available active sites.
Biochar synthesis (pyrolysis temperature)	Biomass feedstock controls elemental composition and ash content; pyrolysis temperature defines surface area, porosity, and functional group abundance.	Higher temperatures generally increase aromaticity and surface area, while lower temperatures preserve oxygenated functional groups important for electrostatic interactions.

Source: Autor.

3.2.2.2 Adsorption Isotherms

The analysis of adsorption equilibrium is fundamental to understanding the mechanisms governing this process and for establishing parameters for the design of separation systems for the involved materials. When an adsorbent material comes into contact with a solution containing a specific adsorbate, molecules or ions migrate from the liquid phase to the solid surface until the system reaches equilibrium, that is, the point at which the solute concentration in the liquid phase (C_e) remains constant and the adsorption capacity of the solid (q_e) can be defined (Ângelo Silva, 2017; Carvalho, 2015; Silva; Lima, 2017). At this stage, the amount of adsorbate retained on the surface corresponds to the amount removed from the solution, with the adsorption capacity being calculated through a mass balance, as shown by Equation 1.

$$q_e = \frac{(C_o - C_e) * V}{m} \qquad (1)$$

Where:

- C_o is the initial concentration of adsorbate (mg L^{-1})
- C_e is the equilibrium concentration of adsorbate (mg L^{-1})
- V is the volume of solution (L)
- m is the adsorbent mass (g), and
- q_e is the adsorption capacity (mg g^{-1})

Adsorption isotherms describe the relationship between the amount of solute adsorbed by a solid material and the concentration of that solute at equilibrium, at a constant temperature. They therefore represent an essential tool for understanding the behavior of the adsorption process and for estimating the amount of adsorbent required to remove a specific concentration of contaminant in solution. In addition to allowing the evaluation of the adsorptive capacity of different materials, isotherms constitute the first experimental information used in the comparison of potential adsorbents, serving as an initial parameter in the selection of the most

suitable material for specific applications (Carvalho, 2015; Silva; Lima, 2017; Tavares Martins Filho, 2012).

To broaden the understanding of the phenomenon and analyze the structural characteristics of adsorbents, different mathematical models, of a theoretical or empirical nature, have been proposed over time. Among them, the Langmuir and Freundlich models stand out, being widely applied to carbonaceous materials (Silva; Lima, 2017).

3.2.2.2.1 Langmuir Isotherm

The Langmuir model is one of the most widely used for representing adsorption processes, especially for Type I isotherms. This model is based on theoretical assumptions that simplify the understanding of the phenomenon: (i) adsorption occurs in a monolayer, meaning each active site on the adsorbent surface can accommodate only one adsorbate molecule; (ii) all sites exhibit the same adsorptive energy; (iii) the adsorption energy is constant and independent of surface coverage; and (iv) there is no interaction between already adsorbed molecules and those in the fluid phase. Thus, the maximum adsorption capacity corresponds to the complete coverage of the solid surface by a single layer of molecules, in reversible equilibrium with the liquid phase (Ângelo Silva, 2017; Carvalho, 2015; Silva; Lima, 2017).

Validation of the Langmuir model is performed using experimental data obtained under equilibrium conditions. The residual solute concentration in solution (C_e) is determined experimentally, while the adsorption capacity of the solid (q_e) is calculated via mass balance. These data allow for the fitting of the Langmuir model equation to verify its adequacy to the experimental isotherm and to estimate fundamental parameters, such as the maximum adsorption capacity and the affinity constant between adsorbent and adsorbate (Ângelo Silva, 2017; Silva; Lima, 2017; Tavares Martins Filho, 2012).

Thus, the non-linear form of the Langmuir model is represented by the following Equation 2:

$$q_e = \frac{q_{m*} K_{L*} C_e}{[1+K_L*C_e]} \qquad (2)$$

where:

- q_e is the adsorption capacity at equilibrium (mg g^{-1})
- q_m is the maximum adsorption capacity corresponding to complete monolayer coverage (mg g^{-1})

- K_L is the Langmuir constant related to the affinity between adsorbate and adsorbent ($L\ mg^{-1}$)
- C_e is the equilibrium concentration of the adsorbate in solution ($mg\ L^{-1}$).

The linearized form of the Langmuir equation was employed for the determination of the model's characteristic parameters, particularly the maximum adsorption capacity (q_{max}) and the Langmuir constant (K_L). Equation 3 shows the linearized form: (Ângelo Silva, 2017)

$$\frac{C_e}{q_e} = \frac{1}{q_m} C_e + \frac{1}{q_{m*}\, K_L} \qquad (3)$$

From the graphical representation of [C_e/q_e] versus (C_e), the slope of the straight line corresponds to [$1/q_{max}$], while the intercept on the vertical axis is given by [$1/(q_{max} \cdot K_1)$]. Therefore, both parameters can be readily determined from the linear regression of the experimental data. The slope of the fitted line corresponds to ($1/q_{max}$), whereas the intercept on the y-axis is used to calculate the Langmuir constant (K_L) (Carvalho, 2015; Tavares Martins Filho, 2012).

Therefore, based on the values of C_e, q_e, and q_{max}, it becomes possible to evaluate the theoretical behavior of the adsorption isotherm according to the Langmuir model, verifying the agreement between the experimental data and the proposed model (Carvalho, 2015).

The analysis of the favorability of the adsorption process can be performed using the separation factor (K_L), also called the equilibrium parameter. It is a dimensionless constant, used in the Langmuir model, that expresses the essential characteristic of the isotherm and enables predicting whether adsorption will be favorable or unfavorable under certain conditions. The calculation of (K_L) is obtained from the parameters I_{max} and (K_L) as described in Equation 4 and qualitatively reflects the performance of the adsorbent/adsorbate system (Ângelo Silva, 2017; Carvalho, 2015; Silva; Lima, 2017).

$$R_L = \frac{1}{[1+K_L * C_i]} \qquad (4)$$

The interpretation of R_L values allows for establishing the relationship between the obtained value and the nature of the process, distinguishing whether adsorption occurs favorably or not. That is: (Carvalho, 2015; Silva; Lima, 2017)

i. $R_L > 1$ indicates unfavorable adsorption,
ii. $R_L = 1$ indicates linear adsorption,
iii. $0 < R_L < 1$ indicates favorable adsorption,

iv. $R_L = 0$ corresponds to irreversible adsorption.

3.2.2.2.2 Freundlich Isotherm

The Freundlich isotherm is an empirical model widely used to describe adsorption processes on heterogeneous surfaces and in systems where multilayer adsorption occurs. Unlike the Langmuir model, which assumes a homogeneous surface and monolayer adsorption with constant energy, the Freundlich model accounts for the heterogeneity of the adsorbent surface, postulating the existence of different types of active sites and an exponential distribution of adsorption energies (Ângelo Silva, 2017; Silva; Lima, 2017; Tavares Martins Filho, 2012).

This approach enables the representation of adsorbent-adsorbate interaction variability under real conditions, reflecting the lack of uniformity of the solid surface. The behavior is mathematically described by Equation 5, which expresses the relationship between the amount adsorbed and the solute concentration at equilibrium in a logarithmic form (Carvalho, 2015).

$$q_e = K_F + C_e^n \qquad (5)$$

where:

- K_F is Freundlich's constant in ($\mathrm{mg\ g^{-1}}$)
- n is Freundlich's dimensionless exponent related to the intensity of the adsorption.

3.2.2.3 Adsorption Kinetics

Adsorption kinetics refers to the rate at which solute molecules (adsorbate) are retained by the adsorbent material. This rate is influenced by the physicochemical properties of the adsorbate (such as molar mass and solubility), the structural characteristics of the adsorbent (porosity and surface nature), and the solution conditions (pH, temperature, and concentration) (Ângelo Silva, 2017; Tavares Martins Filho, 2012). Thus, the adsorption process, in kinetic terms, involves three main steps: (i) external diffusion, where the adsorbate moves through the liquid film surrounding the adsorbent; (ii) intraparticle diffusion, characterized by the migration of the solute into the interior of the pores; and (iii) final interaction with the active sites present on the solid surface (Carvalho, 2015; Tavares Martins Filho, 2012).

In effluent treatment, the study of kinetics is fundamental, as it allows for determining the process efficiency, the time required to reach equilibrium, and the speed at which contaminant removal occurs. Therefore, the use of models capable of describing and predicting the system's behavior is indispensable (Tavares Martins Filho, 2012).

Thus, various kinetic models have been employed to elucidate the mechanisms controlling the adsorption process, which may be associated with chemical reactions, diffusion, or mass transfer. Among these, the pseudo-first order (PFO) and pseudo-second order (PSO) models stand out, being widely used due to their satisfactory fit to different experimental datasets, in addition to allowing the estimation of relevant kinetic parameters (Ângelo Silva, 2017).

Nevertheless, it is important to emphasize that such models are not always sufficient to definitively describe the predominant adsorption mechanism. In these cases, other approaches can be employed, such as the Elovich, Avrami, Ritchie, and Weber-Morris models, and particularly the intraparticle diffusion model, which is frequently used to complement the interpretation of the mass transport phenomena involved in the process (Ângelo Silva, 2017; Silva; Lima, 2017).

3.2.2.3.1 Pseudo-First Order (PFO) Model

The pseudo-first order (PFO) kinetic model, proposed by Lagergren, is widely used to describe adsorption processes in liquid-solid systems, considering the retention capacity of the adsorbent. This model assumes that the adsorption rate is controlled by a single determining step, directly related to the difference between the amount of solute adsorbed at equilibrium and the amount adsorbed over time (Ângelo Silva, 2017; Tavares Vieira et al., 2024).

To differentiate it from conventional first-order kinetics, which is based on the solution concentration, Lagergren's formulation came to be termed pseudo-first order and is mathematically expressed by Equation 6.

$$\frac{dq_t}{dt} = k_1(q_e - q_t) \quad (6)$$

Where:

- k_1 is the PFO rate constant (min^{-1})
- q_e is amounts of adsorbate adsorbed per gram of adsorbent (mg g^{-1}) at equilibrium
- q_t are the amounts of adsorbate adsorbed per gram of adsorbent (mg g^{-1}) at time t

Integrating Equation (6), and applying the boundary conditions: $q_t = 0, t = 0$ when $q_t = q_t, t = t$, we obtain the linearized form of the model, Equation 7: (Tavares Martins Filho, 2012; Tavares Vieira et al., 2024)

$$ln\,(q_e - q_t) = ln\,(q_e) - k_1 t \quad (7)$$

3.2.2.3.2 Pseudo-Second Order (PSO) Model

The pseudo-second order (PSO) kinetic model, widely applied in adsorption studies, is based on the retention capacity of the adsorbent and allows for describing the process behavior throughout the entire contact time. Unlike the pseudo-first order (PFO) model, this one considers that the adsorption rate is associated with two successive steps: diffusion of the adsorbate through the external layer surrounding the adsorbent particles and the subsequent migration into the pore interior (Ângelo Silva, 2017; Tavares Vieira et al., 2024).

The mathematical formulation of this model, expressed by Equation 8, is based on the hypothesis that the process is controlled by interactions of a chemical nature (chemisorption), being useful for estimating kinetic parameters related to the adsorption mechanism (Ângelo Silva, 2017; Tavares Martins Filho, 2012).

$$\frac{dq_t}{dt} = k_2 * (q_e - q_t)^2 \qquad (8)$$

where k_2 ($g\ mg^{-1}\ min^{-1}$) is the pseudo-second-order adsorption rate constant.

Applying the boundary conditions $q_t = 0$, $q_t = q_t$, and $t = 0$ a $t = t$. And, subsequently integrating, yields the following Equation 9: (Ângelo Silva, 2017; Tavares Vieira et al.)

$$\frac{t}{(q_e - q_t)} = \frac{1}{q_e^2} k_2 t \qquad (9)$$

Subsequently, it can be linearized, resulting in the following Equation 10:

$$\frac{t}{q_t} = \frac{1}{k_2 q_e^2} + \frac{t}{q_e} \qquad (10)$$

4 METODOLOGY

4.1 Sample Preparation

4.1.1 Carnauba Petiole Sample

The petioles derived from the carnauba palm leaves — Figure 9 — were manually collected from palm trees located on the Pici Campus of the Federal University of Ceará (3.7431°S, 38.5788°W; WGS 84; SISGEN Registration Number A2B4F8E), in Fortaleza, Ceará, Brazil.

Figure 9 - Petioles derived from the carnauba palm leaves.

Source: Autor.

The harvested biomass was first dried under sunlight. Following this step, the leaf blades and spines were manually removed to ensure safer handling and to isolate the petiole fraction. The resulting material was then milled and sieved through an 18-mesh screen according to ASTM E1757 (Standard Preparation Method A), producing a total of one (1) kg of Raw Petiole (RP), which was used as the *in natura* sample for subsequent analyses.

4.1.2 Carnauba Petiole-Biochar Sample

Following the preliminary preparation of the Raw Petiole (RP) in sieved powder form, the sample was subjected to a carbonization process. The material was transferred to ceramic crucibles fitted with tight lids to restrict oxygen availability and establish self-generated oxygen-limited conditions during heat treatment at atmospheric pressure, without the need for external inert gas flow. Carbonization was performed in a microprocessor-controlled muffle furnace (Q318M21, Quimis, Brazil). The thermal program involved heating the sample from

room temperature (approximately 25 °C) to 550 °C at a rate of 10 °C·min^{-1}, followed by a holding period of one (1) hour at the final temperature.

Figure 10 - Conversion of biomass to biochar - (a) Raw Petiole and (b) Petiole Biochar.

Source: Autor.

After completion of the thermal treatment, the furnace was left to cool to room temperature. The obtained Petiole Biochar (PB) was subsequently removed from the crucibles and kept in a desiccator with silica gel to avoid moisture absorption before further characterization analyses (Figure 10).

4.1.3 Carnauba Biochar-Bentonite Sample

Subsequently, the PB was dry mixed with a commercial enological sodium bentonite clay (Enogel Master bentonite, São Paulo, Brazil), with a reported purity of 99% and nominal chemical formula $(Na,Ca)_{0.33}(Al,Mg)_2Si_4O_{10}(OH)_2 \cdot nH_2O$, whose mineralogical composition was previously confirmed through characterization analyses. The materials were combined at a mass ratio of 5:1 (biochar:bentonite), without the addition of solvents or dispersing agents, resulting in the biochar-bentonite composite (B-PB). The resulting mixture was then homogenized to ensure uniform distribution of the clay within the biochar matrix prior to subsequent microstructural physical transformation processing.

4.2 High Energy Ball Milling Preparation

High-energy ball milling was performed using a Pulverisette 6 planetary mill (Fritsch GmbH) located at the Advanced Materials Laboratory (LMA) of the Federal University of Ceará (UFC). Biochar and biochar-clay composite samples were milled using 10 g of material per batch. Stainless steel (AISI 304) vials and balls were employed, maintaining a ball-to-powder mass ratio (BPR) of 10:1. This ratio was selected because it provides an adequate balance between impact energy and milling efficiency, promoting effective particle size

reduction and structural modification while avoiding excessive agglomeration or contamination of the material (Baláž, P; Suryanarayana, 2001). The milling experiments were conducted under different operational conditions, including rotation speeds of 200, 300, and 400 rpm and milling times of 2, 4, and 6 hours. The identification of the milled materials follows the nomenclature described in Table 3.

Table 3 - Sample identification and high-energy milling parameters.

Material	Sample type	Time (h)	Rotation speed (rpm)		
			200	300	400
Biochar	PB	2	PB202	PB302	PB402
		4	PB204	PB304	PB404
		6	PB206	PB306	PB406
Bentonite-Biochar Composite	B-PB	2	B-PB202	B-PB302	B-PB402
		4	B-PB204	B-PB304	B-PB404
		6	B-PB206	B-PB306	B-PB406

Source: Autor.

These operational parameters were selected to investigate the influence of increasing mechanical energy input on the structural modification of the biochar and the biochar–bentonite composite. In planetary ball milling systems, rotation speed directly controls the kinetic energy of the milling media and the frequency of ball-powder collisions, whereas milling time determines the extent of particle refinement, defect generation, and mechanochemical activation. According to the literature, intermediate rotation speeds in the range of 200-400 rpm are commonly employed to promote efficient particle size reduction and structural activation without causing excessive amorphization or overheating of the material. Likewise, milling times of a few hours are typically used to monitor the progressive evolution of structural disorder and surface activation during mechanochemical processing (Baláž, P; Suryanarayana, 2001).

4.3 Sample Characterization

4.3.1 Proximate Analysis

Proximate analyses were performed on the RP samples and their resulting PB biochar, in quadruplicate. The procedures were based on the following standards: ASTM E872 for volatile matter content, ASTM D1762−84 for moisture content, ASTM D3172-13 for fixed carbon content, and ASTM E1755 for ash content.

- **Volatile Matter:** the determination of volatile matter (VM) content was performed according to ASTM E872 standard. For this, approximately 1 g of each sample was placed in a porcelain crucible with a lid and heated in a muffle furnace at 950 °C (± 20 °C) for 7 minutes. The percentage value of volatile matter was obtained from the mass loss recorded during the thermal process, using the following mathematical expression 11: (Fuertes *et al.*, 2010; Zhao, S. X.; Ta; Wang, 2017)

$$VM\ (\%) = 100\ \times \left(\frac{W_i - W_f}{W_i - W_c}\right) \quad (11)$$

Where:

i. *VM (%)* = volatile matter content of the sample, expressed on a mass percentage basis.
ii. W_i = initial mass of the crucible assembly (crucible and lid) containing the sample prior to thermal treatment.
iii. W_f = final mass of the crucible assembly containing the residual solid after completion of the volatile matter test.
iv. W_c = mass of the empty crucible assembly (crucible and lid).

- **Moisture Content:** moisture content was assessed according to the procedure described in ASTM D1762−84, using a Shimadzu MOC63u instrument. Approximately 1 (one) g of each sample — including both the raw material and its corresponding biochar — was analyzed and heated to 105 °C until the mass stabilized, a condition that allowed accurate determination of moisture content. (Cao; Harris, 2010; Fuertes *et al.*, 2010)

- **Fixed Carbon.** The fixed carbon quantity method is calculated from the averages of moisture, volatile matter and ash, in accordance with ASTM D3172−13, as shown in the following equation 12: (Fuertes *et al.*, 2010; Zhao, S. X.; Ta; Wang, 2017)

$$FC\ (\%) = 100\ -\ (MC + VM + AC) \quad (12)$$

- **Ash Content:** ash content was determined according to ASTM E1755, in which approximately 1 (one) g of each sample was placed in a porcelain crucible and heated in a

muffle furnace at 575°C ± 25°C for 3 hours. Ash content was calculated by the ratio of the residual mass to the initial mass of the sample, as shown in the following equation 13: (Cao; Harris, 2010; Fuertes *et al.*, 2010)

$$Ash\ (\%) = 100 \times \left(\frac{(W_i - W_f) \times 100}{W_s \times W_i}\right) \quad (13)$$

Where:

i. *Ash (%)* = ash content of the sample, expressed on a dry weight basis.
ii. W_i = initial mass of the empty crucible prior to calcination.
iii. W_f = final mass of the crucible containing the inorganic residue (ash) after complete combustion of the sample.
iv. W_s = dry mass of the sample subjected to the ash determination test.

The residues resulting from the raw material (RP) and biochar (PB) samples were stored in hermetically sealed containers for later analysis.

4.3.2 Elemental Analysis

The elemental composition of carbon, hydrogen, nitrogen and oxygen (C, H, N, and O) was obtained by direct combustion in a Perkin Elmer 2400 Series II. Approximately 2 (two) mg of samples (both the original biomass and the respective biochars) were weighed into tin capsules and subjected to duplicate analyses. The oxygen content was determined indirectly by the difference in the values of carbon, hydrogen, nitrogen, and ash contents.

4.3.3 XRD

X-ray diffraction (XRD) analyses were performed on a PANalytical X'Pert PRO diffractometer, available at the X-ray Laboratory (LRX) of the Federal University of Ceará (UFC). Co-Kα radiation was used to acquire the patterns, covering the range from 3º to 100º in 2θ, with a reading increment of 0.013º.

4.3.4 FTIR

Fourier-Transform Infrared (FTIR) analyses were conducted on a Bruker VERTEX 70v spectrometer coupled to an ATR accessory, available at the Vibrational Spectroscopy Laboratory (LEV) of the Federal University of Ceará (UFC). For midinfrared measurements, a Globar radiation source was used, combined with a DLaTGS pyroelectric detector. Each spectrum was recorded in the 4000-380 cm^{-1} range, with a 2 (two) cm^{-1} resolution and an average of 128 scans per sample, ensuring high data reliability and reproducibility.

4.3.5 SEM/EDS

Morphological and elemental characterization was conducted using a Hitachi TM3000 scanning electron microscope coupled to a Swift ED3000 EDS system at the Electron Microscopy Laboratory (LME) of the Federal University of Ceará (UFC). Samples were prepared on aluminum stubs and fixed with copper tape. Micrographs were obtained in SE and BSE modes under an accelerating voltage of 15 kV. EDS analyses, performed in the 0-20 keV range, allowed us to determine the chemical composition of the different materials, highlighting the variations between in natura samples, biochars, and ashes, in addition to the characterization of bentonite clay. Interpretation of the results emphasized the structural differences observed in the images and the changes in elemental composition between the analyzed sets.

4.3.6 Thermal Analysis

Thermal behavior was evaluated by thermogravimetric (TG), derivative thermogravimetric (DTG), and differential thermal analysis (DTA) using a NETZSCH STA 449 F3 Jupiter instrument. The measurements were conducted under a controlled atmosphere from 30 °C to 900 °C at a constant heating rate of 10 $K \cdot min^{-1}$. To ensure the accuracy of the results, an Al_2O_3 crucible was used, with a continuous flow of nitrogen (20 mL/min) as shielding gas and synthetic air (80/20, 50 mL/min) as purge gas. The analyses were conducted at the Federal University of Ceará.

4.4 Methylene Blue Adsorption Test

In the context of batch adsorption experiments, a stock solution of MB (analytical grade, C.I. 52015, CAS N° 122965-43-9, $C_{16}H_{18}ClN_3S \cdot xH_2O$, MW: 319.85 $g \cdot mol^{-1}$, Neon, Brazil) was prepared at a concentration of 1.0 $g \cdot mol^{-1}$ in distilled water. The biochar samples were weighed using an analytical balance (M5-M214Ai, BEL Engineering, Italy) with a readability of 0.0001 g (0.1 mg). All adsorption tests were conducted in quadruplicate, and the reported values of adsorption capacity (q_e) and removal efficiency (R) represent the meaning of four independent determinations.

The stock solution was kept in a sealed glass container under laboratory conditions and protected from direct light. The working solutions were obtained by dilution immediately before each adsorption test. Batch experiments were performed in 50 mL glass beakers using a horizontal shaker (Go Shaker SK-180-Pro) operated at 250 rpm and 25 °C under controlled lighting conditions, with no direct light exposure to minimize potential photochemical interference. After the predetermined contact times, the suspensions were centrifuged at 4000

rpm for 10 minutes, and the supernatant was subsequently analyzed. In all adsorption experiments, the initial solution pH was adjusted to 6, corresponding to a near-neutral condition chosen to reduce secondary chemical effects and to ensure consistent analytical determinations.

The remaining methylene blue concentration was determined by UV-Vis spectrophotometry (Shimadzu UV-2600), with absorbance spectra recorded at the characteristic wavelength of 664 nm. Based on the experimental adsorption data, the adsorption capacity, removal efficiency, and the parameters of the kinetic and equilibrium isotherm models were subsequently calculated.

4.4.1 Effect of Adsorbent Amount

The influence of adsorbent mass will be investigated by varying the quantity of biochar and biochar-clay composites, employing mass levels of 5, 10, 25, 50, 75, and 100 mg in 50 ml of a methylene blue solution with an initial concentration of 15 mg/L. A fixed contact time of 30 minutes will be adopted to approximate the system's equilibrium conditions.

4.4.2 Adsorption Isotherms

Isothermal experiments will be conducted to evaluate the adsorption behavior under equilibrium conditions. The optimal adsorbent quantity, as determined in prior assays, will be added to 50 ml of methylene blue solutions with initial concentrations of 2, 5, 8, 12, 15, and 20 mg/L. After a 30 minutes contact period under agitation, the equilibrium concentration (C_e) will be determined, and the adsorption capacity (q_e) will be calculated. The obtained data will be fitted to the Langmuir and Freundlich isotherm models for analysis of the system's behavior.

4.4.3 Adsorption Kinetics

Kinetic assays will be performed using an initial methylene blue concentration of 15 mg/L and 50 mg of adsorbent. Contact times will be set at 1, 5, 15, 30, 60, and 120 minutes; at each interval, samples will be collected, centrifuged, and analyzed by spectrophotometry. The adsorption capacity as a function of time (q_t) was determined, and the experimental results were fitted to the Pseudo-First Order (PFO) and Pseudo-Second Order (PSO) kinetic models.

Table 4 - Operational parameters employed in the MB adsorption assays using biochar (PB) and biochar–bentonite composites (B–PB).

Experiments	MB Concentration (mg/L)	Contact Time (min)	Biochar Mass (mg)	Solution Volume (ml)	pH*

Biochar Dosage Variation	**15**	**120**	**2, 5, 10, 15, 20, 25**	**50**	**6**
Contact Time Variation	**15**	**0, 5, 15, 30, 60, 120, 180, 240**	**5**	**50**	**6**
MB Concentration Variation	**2.5, 5, 8, 10, 15, 20, 40, 50, 70, 100, 150**	**120**	**5**	**50**	**6**

*Before each experiment, the pH of the solution was carefully adjusted to 6.0 by adding 0.1 M HCl or 0.1 M NaOH as needed.

Source: Autor.

5 RESULTS AND DISCUSSION

▪ PART I

5.1 Proximate Analysis

Graphic 1 summarizes the results of the proximate analysis performed on the raw petiole (RP) and its corresponding biochar (PB), enabling a comparative evaluation of the compositional modifications induced by carbonization in terms of volatile matter, moisture, ash, and fixed carbon contents.

Graphic 1 - Results of the proximate analysis for RP and PB.

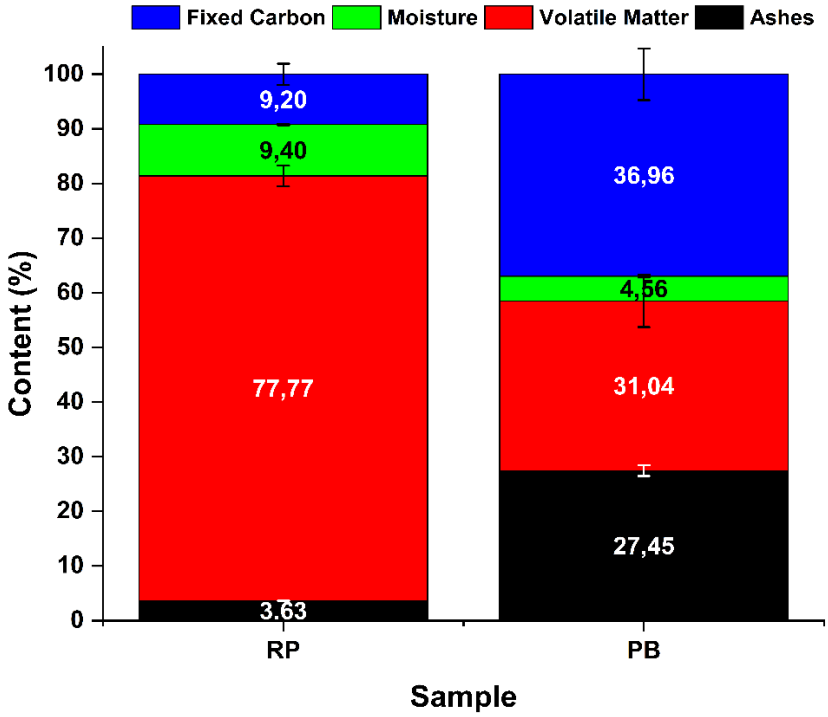

. Source: Autor.

As presented in the graphic, RP is predominantly composed of volatile matter (77.77%), followed by moisture (9.40%), fixed carbon (9.20%), and ash (3.63%). This distribution is typical of lignocellulosic biomass, whose structural components — mainly cellulose and hemicellulose — thermally degrade within the range of approximately 200-380 °C, producing condensable vapors and gaseous products during pyrolysis (Xu, Y.; Chen, 2013). The relatively low fixed carbon content observed in RP reflects the limited presence of condensed aromatic structures and the reduced thermal stability characteristic of native biomass materials (Xu, R. *et al.*, 2023).

Following carbonization at 550 °C, substantial compositional modifications were observed in the PB, confirming the effectiveness of the thermochemical conversion process. Among the

most pronounced changes was the sharp decrease in volatile matter content to 31.04% (Δ = −39.3%; $p < 0.001$), which reflects the thermal cracking and progressive decomposition of lignocellulosic fractions during pyrolysis. The degradation of hemicellulose, cellulose, and partially lignin leads to the release of labile organic compounds in the form of condensable vapors and permanent gases, leaving behind a more carbon-rich solid residue (Fuertes *et al.*, 2010; Zhao, S. X.; Ta; Wang, 2017).

The detailed quantitative values of these variations are systematized in Table 5, complementing the analysis presented graphically.

Table 5 - Biomass-biochar pair analysis by paired t-test: approximate analysis parameters before and after carbonization.

Pair	Parameter	Δ (%) [a]	t(*df*) [b]	*p*-value [c]	Effect Size (d) [d]	Direction [e]	Homogenous Group [f]
RP–PB	Ash (%)	15.8	t(3.00) = − 4.74	0.018	− 3.41	↑	RP: a PB: a
	Volatiles (%)	− 39.3	t(3.00) = 17.6	< 0.001	12.6	↓	RP: a PB: a
	Moisture (%)	− 3.06	t(3.00) = 15.5	< 0.001	11.1	↓	RP: a PB: ab
	Fixed Carbon (%)	26.5	t(2.52) = − 5.26	0.026	− 3.77	↑	RP: a PB: a

[a] Relative mass difference (percentage). [b] Test statistics and degrees of freedom. [c] Significance level of the observed difference. [d] Quantifies the magnitude of the difference. [e] Indicates the increase or decrease relative to the reference material. [f] Homogeneous groups were assigned according to the Games-Howell test. Means sharing the same letter do not differ significantly ($p > 0.05$), whereas means labeled with different letters differ significantly ($p < 0.05$). When a mean is denoted by two letters (e.g., "ab"), it indicates that this value does not differ significantly from the groups represented by either letter.

Simultaneously, a substantial increase in fixed carbon content was observed, rising from 9.20% in RP to 36.96% in PB (Δ = +26.5%; $p = 0.026$). This enrichment is characteristic of biochar formation and results from the progressive aromatization and condensation of carbonaceous structures during thermal treatment. The formation of condensed aromatic domains increases the density of π−electron systems within the carbon matrix, which can enhance the affinity of the material for aromatic pollutants through π−π interactions. This mechanism is particularly relevant for the adsorption of aromatic cationic dyes such as methylene blue, as reported in previous studies on lignocellulosic biochars (Fuertes *et al.*, 2010; Zhao, S. X.; Ta; Wang, 2017). Similar compositional trends have been documented for biochars derived from agricultural residues such as corn straw, sugarcane bagasse, and cocoa husk,

further supporting the structural transformation observed in the present study (Fuertes *et al.*, 2010; Ramola *et al.*, 2022).

Another significant modification resulting from carbonization was the increase in ash content from 3.63% in the biomass to 27.45% in the biochar ($\Delta = +15.8\%$; $p = 0.018$; $d = -3.41$). This increase reflects the relative accumulation of inorganic constituents after the removal of the organic fraction during pyrolysis. Mineral elements commonly present in plant tissues — such as potassium, calcium, and magnesium — become concentrated in the residual carbon matrix, a behavior widely reported for palm-derived biomasses (Paula *et al.*, 2020; Pereira Junio *et al.*, 2022). The presence of these mineral phases may influence the physicochemical properties of the adsorbent by modifying surface alkalinity and potentially acting as active sites for ion exchange or charge neutralization processes during adsorption of cationic species (Pereira Junio *et al.*, 2022; Zhao, S. X.; Ta; Wang, 2017).

The moisture content also exhibited a reduction, decreasing from 9.40% in RP to 4.56% in PB ($\Delta = -3.06\%$; $p < 0.001$). The relatively low initial moisture content of the biomass is advantageous for thermochemical processing because it reduces both the energy demand and the duration of thermal treatment. After carbonization, the lower moisture content contributes to improved storage stability of the adsorbent and may reduce competition between water molecules and adsorbate species for surface adsorption sites (Fuertes *et al.*, 2010).

From a comparative perspective, the compositional characteristics obtained for the carnauba petiole biochar (PB) exhibit important similarities and differences when contrasted with conventional Activated carbon, which is widely recognized as the benchmark adsorbent for dye removal from aqueous systems. Activated carbons typically present high fixed carbon contents (generally above 70–85%), low volatile fractions, and ash contents usually below 10%, reflecting the intensive thermal and chemical activation processes used during their production (Ioannidou; Zabaniotou, 2007; Marsh *et al.*, 2006). In comparison, the PB produced in this study exhibited moderate fixed carbon content (36.96%) and a relatively high ash fraction (27.45%), which indicates that the material underwent carbonization. Although the fixed carbon content is lower than that of commercial activated carbon, the increased aromaticity resulting from pyrolysis still promotes the formation of conjugated carbon structures capable of interacting with aromatic pollutants such as methylene blue through π–π interactions (Ahmad *et al.*, 2020; Fuertes *et al.*, 2010). Moreover, the higher ash content observed in PB may contribute positively to adsorption processes by introducing mineral phases capable of promoting electrostatic interactions, ion exchange, and surface complexation mechanisms with

cationic dyes (Inyang *et al.*, 2012). In contrast to activated carbon, whose adsorption performance is primarily governed by its highly developed microporous structure and extremely high specific surface area, biochars generally exhibit lower surface areas but can compensate through the presence of oxygenated functional groups, mineral components, and surface heterogeneity (Lehmann; Joseph, 2009). Therefore, while the proximate composition of PB reflects a less carbon-rich structure compared with activated carbon, its physicochemical characteristics still provide multiple adsorption pathways, supporting its potential as sustainable alternative adsorbent for dye removal in aqueous systems.

Collectively, the results of the proximate analysis demonstrate that the carbonization process substantially altered the composition and structural characteristics of the carnauba petiole biomass. The resulting biochar exhibits:

(i) Increased structural stability associated with higher fixed carbon content.
(ii) Enriched mineral composition reflected by elevated ash content.
(iii) Reduced volatile and moisture fractions.

These transformations are directly related to improvements in physicochemical properties relevant to adsorption processes, including enhanced aromaticity, potential surface reactivity, and greater stability of the carbon matrix. Consequently, the observed compositional changes strongly support the suitability of carnauba petiole-derived biochar as a sustainable bioadsorbent for environmental applications, particularly for the removal of organic pollutants such as methylene blue from aqueous systems.

5.2 Elemental Analysis

Graphic 2 illustrates the distribution of the main elemental constituents of the raw petiole biomass (RP) and the derived biochar (PB), highlighting the compositional transformations induced by the pyrolysis process. Elemental analysis provides fundamental insights into the chemical structure and degree of carbonization of lignocellulosic materials, allowing the evaluation of parameters such as aromaticity, polarity, and thermal stability of carbonaceous solids. The pronounced shifts in elemental composition observed after carbonization reflect typical thermochemical reactions occurring during pyrolysis, including dehydration, decarboxylation, and devolatilization, which progressively transform the biomass into a carbon-rich and structurally condensed material.

Graphic 2 - Results of the ultimate analysis for RP and its PB.

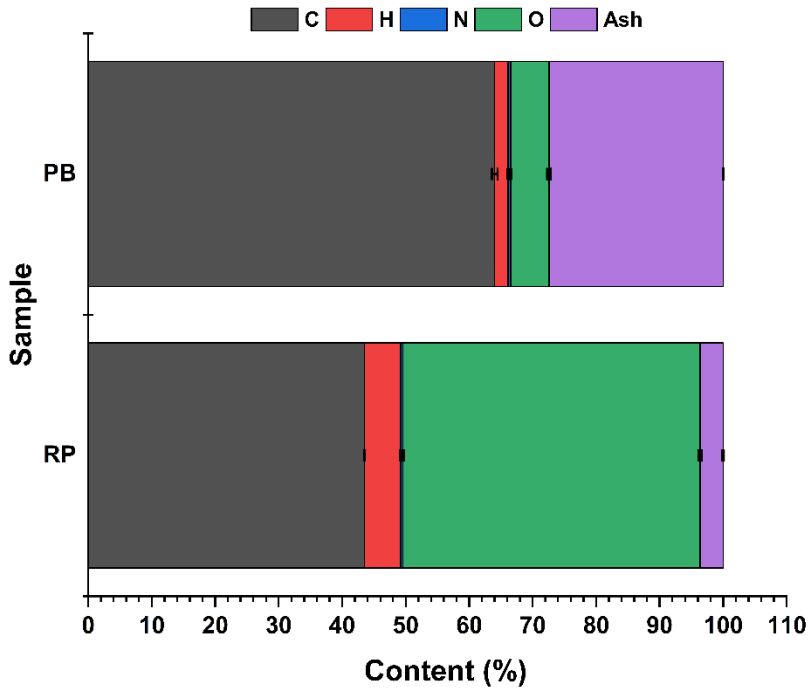

Source: Autor.

The quantitative elemental composition of RP and PB is summarized in Table 6. The raw biomass exhibited a carbon content of 43.49 wt%, hydrogen of 5.74 wt%, nitrogen of 0.33 wt%, and oxygen of 46.83 wt%, values typical of lignocellulosic feedstocks composed mainly of cellulose, hemicellulose, and lignin. After pyrolysis at 550 °C, the carbon content increased significantly to 64.02 wt%, corresponding to an absolute enrichment of approximately 20.5 wt%. This increase results primarily from the thermal decomposition of oxygenated and hydrogenated organic compounds and the progressive concentration of carbon within the residual matrix. Such enrichment in carbon is widely reported for biochars derived from agricultural residues and woody biomass and reflects the formation of increasingly condensed aromatic structures during carbonization (Ahmad *et al.*, 2020; Reza *et al.*, 2020).

Table 6 - Results of elemental analysis of biomass (RP) and its biochar (PB).

Sample	C (wt%)	H (wt%)	N (wt%)	O (wt%) *	Ashes (wt%)	H/C ratio (mol/mol)	O/C ratio (mol/mol)	N/C ratio (mol/mol)
RP	43.49 ± 0.02	5.74 ± 0.12	0.33 ± 0.19	46.83 ± 0.28	3.63 ± 0.12	1.57	0.81	0.01
PB	64.02 ± 0.42	2.11 ± 0.04	0.41 ± 0.08	06.03 ± 0.29	27.45 ± 0.08	0.39	0.07	0.01

* Oxygen content was estimated by difference: O % = 100% − (C% + H% + N% + Ashes%).

Source: Autor.

Concomitantly, the hydrogen content decreased markedly from 5.74 wt% in RP to 2.11 wt% in PB. This reduction is associated with the thermal degradation of labile organic fractions, particularly cellulose and hemicellulose, which release volatile products such as water vapor, methane, and light hydrocarbons during pyrolysis. The loss of hydrogen is indicative of the progressive removal of aliphatic structures and hydroxyl groups, resulting in a carbon matrix that is less hydrophilic and chemically more stable. Similar decreases in hydrogen content have been observed in numerous lignocellulosic biochars produced at temperatures above 500 °C, reflecting the transition from aliphatic to aromatic carbon domains (Pradhan *et al.*, 2020; Reza *et al.*, 2020).

Nitrogen content remained low in both materials, changing slightly from 0.33 wt% in RP to 0.41 wt% in PB. This small increase likely reflects the relative concentration of nitrogen during the loss of organic matter as well as the possible stabilization of nitrogen-containing aromatic structures such as pyridinic or pyrrolic moieties within the char matrix (Pradhan *et al.*, 2020; Yao *et al.*, 2014). Nevertheless, the overall nitrogen level remains low, which is typical for non-leguminous plant biomass and suggests that nitrogen functionalities play a limited role in the surface chemistry of the resulting biochar.

Oxygen content, calculated by difference, decreased sharply from 46.83 wt% in RP to 6.03 wt% in PB. This reduction reflects the elimination of oxygenated functional groups during pyrolysis through the release of CO, CO_2, and H_2O. The removal of oxygen-containing groups leads to a material with lower polarity and increased chemical stability, characteristics commonly associated with highly carbonized biochars. In addition, the substantial increase in ash content from 3.63 wt% to 27.45 wt% indicates the concentration of inorganic mineral constituents after the thermal degradation of the organic fraction, a phenomenon commonly observed in biomass-derived biochars (Lehmann; Joseph, 2009; Reza *et al.*, 2020).

The elemental composition can also be interpreted through atomic ratios, which provide useful indicators of structural transformations. The H/C ratio decreased drastically from 1.57 in RP to 0.39 in PB, indicating a pronounced increase in aromaticity and the formation of more condensed carbon structures. Low H/C ratios are commonly interpreted as evidence of highly aromatic and thermally stable biochars. Similarly, the O/C ratio declined from 0.81 to 0.07, reflecting a strong reduction in oxygen-containing functional groups and confirming the progression of carbonization reactions. In contrast, the N/C ratio remained practically constant (≈ 0.01), reinforcing the minor contribution of nitrogen functionalities to the overall structure of the material (Pradhan *et al.*, 2020; Yang *et al.*, 2020).

These compositional changes agree with the results obtained from the proximate analysis, in which the increase in fixed carbon and the reduction in volatile matter likewise evidenced progressive carbon enrichment during pyrolysis. Taken together, the proximate and ultimate analyses demonstrate that the transformation of RP into PB is characterized by the development of more condensed aromatic carbon structures along with the relative concentration of inorganic mineral constituents.

Further insights into these transformations are provided by Van Krevelen's diagram presented in Graphic 3.

Graphic 3 - Van Krevelen diagram for RP and PB.

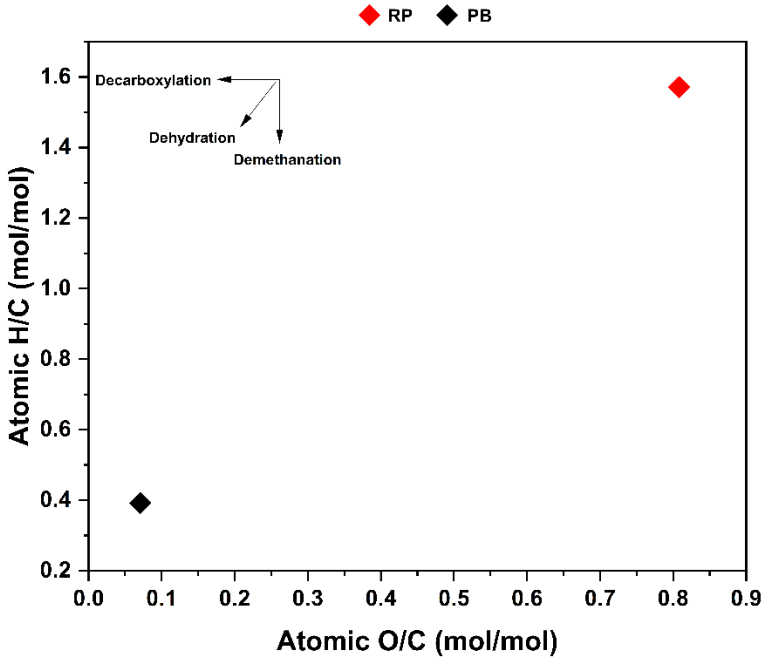

Source: Autor.

This diagram is widely used to evaluate the evolution of carbonaceous materials during thermal conversion processes. The displacement of the PB point toward the lower-left region of the diagram clearly indicates extensive dehydrogenation and deoxygenation reactions during pyrolysis (Pradhan *et al.*, 2020; Reza *et al.*, 2020). Such movement is typically associated with dehydration, decarboxylation, and demethanation reactions, which progressively remove hydrogen and oxygen atoms from the structure and promote the formation of condensed aromatic carbon networks. The position of PB in the diagram, characterized by H/C < 0.5 and O/C < 0.1, is consistent with biochars produced at relatively high pyrolysis temperatures and indicates a highly carbonized and chemically stable material (Lehmann; Joseph, 2009; Reza *et al.*, 2020).

The elemental composition and derived atomic ratios also provide valuable insights into the potential adsorption mechanisms of methylene blue, a planar aromatic cationic dye. The low H/C ratio observed in PB suggests a high degree of aromaticity, which enhances the density of π−electrons on the carbon surface and favors π–π interactions with the aromatic ring system of methylene blue. These interactions are widely recognized as an important adsorption mechanism for aromatic dyes on carbonaceous materials (Lehmann; Joseph, 2009; Pradhan *et al.*, 2020). In addition, the relatively high ash content indicates the presence of mineral constituents that may provide additional adsorption pathways through electrostatic attraction, ion exchange, or surface complexation with cationic species (Ioannidou; Zabaniotou, 2007).

From a broader perspective, the elemental composition of PB can also be compared with that of conventionally activated carbon. Activated carbons typically exhibit carbon contents above 80 wt%, very low H/C ratios (< 0.3), and significantly lower ash contents, generally below 10 wt%, due to the activation processes used during their production (Ioannidou; Zabaniotou, 2007; Marsh *et al.*, 2006). In comparison, the biochar produced in this study presents a moderate carbon content (64.02 wt%) and a higher ash fraction (27.45 wt%), indicating that it underwent carbonization. Nevertheless, the relatively low H/C ratio (0.39) suggests the presence of a well-developed aromatic carbon structure capable of interacting with aromatic pollutants through π–π interactions. Furthermore, the higher mineral content of biochar may contribute positively to adsorption processes by providing additional active sites for ion exchange and electrostatic interactions with cationic dyes (Ioannidou; Zabaniotou, 2007; Marsh *et al.*, 2006). Therefore, although PB does not reach the carbon purity or structural order typically observed in activated carbons, its combined characteristics — moderate aromaticity, mineral-rich composition, and heterogeneous surface chemistry — can enable multiple adsorption mechanisms and support its potential as a sustainable and low-cost alternative adsorbent for dye removal from aqueous systems.

5.3 XRD

The X-ray diffraction patterns of RP and the PB are presented in Graphic 4, allowing the evaluation of structural transformations induced by the carbonization process.

Graphic 4 - Diffractogram of RP and PB.

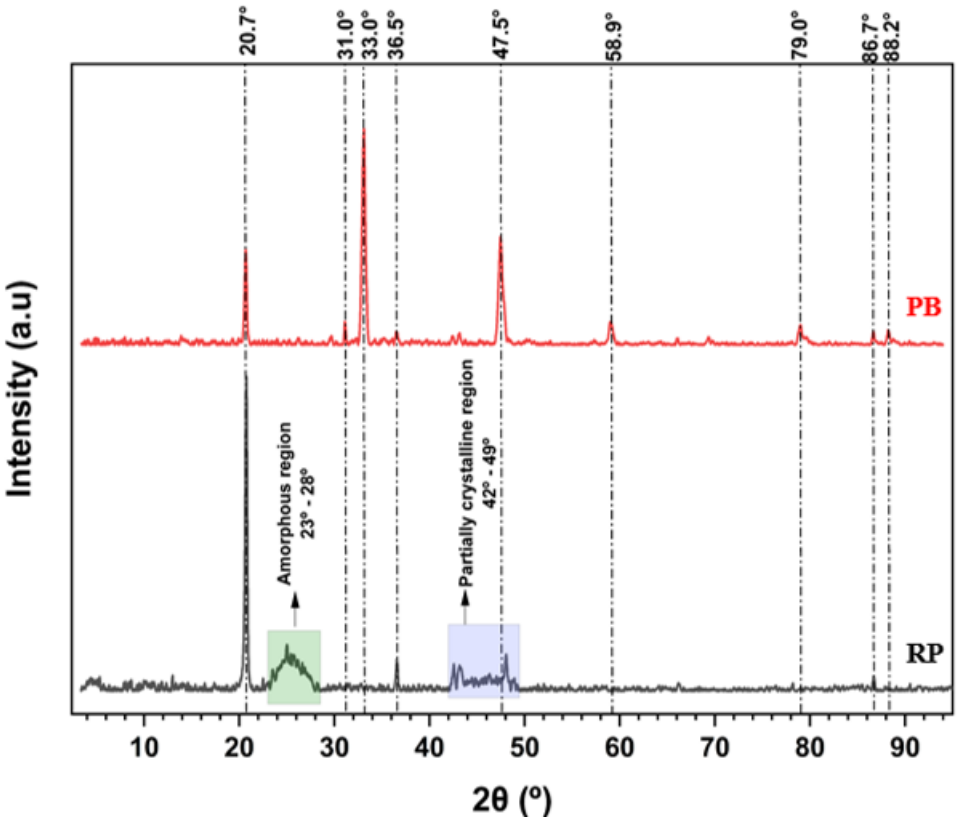

Source: Autor.

The diffractogram of RP exhibits a typical profile of lignocellulosic biomass, characterized by a combination of crystalline and amorphous features. A prominent peak at approximately 20.7° (2θ) is observed, which is commonly associated with the (002) plane of cellulose I, indicating the presence of crystalline domains ordered within the plant cell wall (Nanda *et al.*, 2013; Subratti *et al.*, 2021). Additionally, a broad halo in the range of 23-28° confirms the predominance of amorphous components, mainly hemicellulose and lignin. Secondary features, including reflections near 36.5° and a partially crystalline region between 42-49°, suggest localized structural organization, possibly related to microcrystalline cellulose domains and minor mineral phases such as silica or quartz dispersed within the biomass matrix. The relatively broad and low-intensity nature of these signals indicates a low degree of crystallinity, which is consistent with the heterogeneous anatomical structure of plant tissues (Chang *et al.*, 2023; Subratti *et al.*, 2021).

After pyrolysis, the diffractometric profile of PB undergoes significant modifications, reflecting the profound structural reorganization of the material. The disappearance or attenuation of the amorphous halo and the emergence of sharp and well-defined peaks at approximately 31.0°, 33.0°, 47.5°, 58.9°, 79.0°, and in the region of 86-88° clearly indicate the

formation and/or concentration of crystalline inorganic phases (Chang *et al.*, 2023; Subratti *et al.*, 2021). These peaks are commonly attributed to mineral constituents such as quartz (SiO_2), carbonates (e.g., $CaCO_3$ and $K_2Ca(CO_3)_2$), and other inorganic salts derived from the ash fraction of the biomass. This behavior is a direct consequence of the thermal degradation of organic components during pyrolysis, which leads to the volatilization of lignocellulosic fractions and the relative enrichment of mineral matter in the solid residue (Chang *et al.*, 2023; Pasumarthi *et al.*, 2024).

Concomitantly, the loss of crystalline cellulose and amorphous lignocellulosic structures is evidenced by the reduction of diffuse scattering and the absence of typical biomass-related features. This structural transformation is consistent with the results obtained from proximate and elemental analyses, particularly the decrease in volatile matter, the reduction in H/C and O/C ratios, and the increase in fixed carbon and ash content. Together, these changes confirm the progression of carbonization and the conversion of the original biomass into a more stable carbonaceous material with a heterogeneous structure composed of disordered carbon domains and crystalline inorganic phases (Anoop; Palanisamy, 2025; Pasumarthi *et al.*, 2024).

It is noteworthy that, although biochars often exhibit a broad diffraction band associated with turbostratic or poorly ordered graphitic carbon (typically in the range of 20-30° for Cu-Kα radiation), this feature is not strongly pronounced in the PB sample. This suggests that the carbon structure is predominantly disordered with limited graphitic stacking or that the signal from inorganic crystalline phases dominates the diffractogram. Such behavior indicates that, under the applied pyrolysis conditions (550 °C), the degree of graphitization is relatively low, and the material retains a largely amorphous carbon structure interspersed with mineral crystallites (Anoop; Palanisamy, 2025; Chang *et al.*, 2023; Subratti *et al.*, 2021).

From the perspective of adsorption mechanisms, these structural characteristics are highly relevant. The coexistence of disordered carbon domains and crystalline inorganic phases creates a heterogeneous surface environment capable of supporting multiple adsorption pathways. The amorphous carbon fraction contributes to adsorption through π–π interactions and hydrophobic effects, particularly relevant for aromatic molecules such as methylene blue. At the same time, the mineral phases detected by XRD can provide active centers for electrostatic attraction, ion exchange, and surface complexation with cationic species. Accordingly, the XRD results reinforce the interpretation that adsorption by PB occurs through the combined action of several mechanisms rather than being controlled by a single predominant interaction, which is a behavior commonly reported for biochars derived from lignocellulosic biomass.

From a comparative standpoint, activated carbons generally exhibit broad and diffuse XRD patterns dominated by two characteristic bands around ~23° and ~43°, corresponding to the (002) and (100) planes of turbostratic graphite-like structures, reflecting a predominantly amorphous carbon matrix with a higher degree of structural ordering at the nanoscale (Ioannidou; Zabaniotou, 2007; Marsh *et al.*, 2006). In contrast, the PB analyzed in this study shows a diffractogram strongly influenced by sharp crystalline peaks associated with inorganic phases, indicating a lower degree of graphitic organization and a higher mineral content. While activated carbon adsorption performance is mainly governed by its highly developed microporous structure and extensive π−electron system, the biochar exhibits a more heterogeneous structure in which mineral components play a significant role (Ioannidou; Zabaniotou, 2007; Marsh *et al.*, 2006). This difference suggests that, although PB may not reach the same level of structural ordering or surface area as activated carbon, its adsorption performance can benefit from additional mechanisms such as ion exchange and mineral-mediated electrostatic interactions. Consequently, the XRD results reinforce the classification of PB as a mineral-rich, partially ordered carbon material with multifunctional adsorption capabilities, supporting its application as a low-cost alternative adsorbent for dye removal.

5.4 FTIR

The FTIR spectra of the raw petiole biomass (RP) and the corresponding biochar (PB) are presented in Graph 5, enabling the identification of functional groups and the evaluation of structural changes induced by carbonization. The comparison between both spectra provides important insights into the chemical transformations of the material and their implications for adsorption behavior.

Graphic 5 - FTIR analysis of RP and PB.

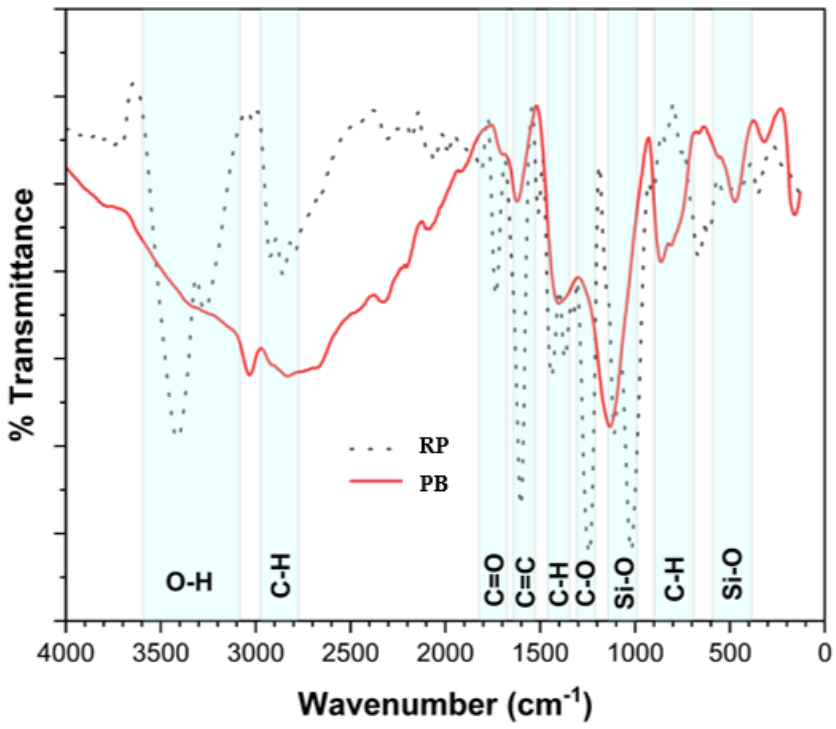

Source: Autor.

The FTIR spectrum of RP displays the characteristic absorption bands of lignocellulosic materials, confirming a composition dominated by polysaccharides and oxygen-containing functional groups. The broad absorption band observed between 3410 and 3415 cm^{-1} is associated with O–H stretching vibrations of hydroxyl groups present in hemicellulose, cellulose and lignin, reflecting the highly polar nature of the biomass surface (Lu, 2002; Pasumarthi *et al.*, 2024). The bands located at 2924 and 2855 cm^{-1} are attributed to aliphatic C–H stretching of methyl and methylene groups originating from the structural biopolymers. The peak near 1732 cm^{-1} corresponds to C=O stretching vibrations of ester and carboxylic functionalities, predominantly associated with hemicellulose, whereas the absorptions around 1600 and 1510 cm^{-1} are related to aromatic C=C vibrations characteristic of lignin. Additionally, the region between 1300-1200 cm^{-1} reflects C−O stretching in glycosidic bonds. These features are consistent with the proximate analysis, which indicates high volatile matter content, and with elemental analysis results showing elevated O/C and H/C ratios, typical of low-carbonized, highly functionalized biomass. Furthermore, the XRD pattern of RP, characterized by a broad amorphous halo and low-intensity crystalline peaks, supports the predominance of disordered lignocellulosic structures associated with these functional groups (Jindo *et al.*, 2014; Lu, 2002; Tomczyk; Sokołowska; Boguta, 2020).

After pyrolysis, the FTIR spectrum of PB shows pronounced structural modifications that reflect the transition to a carbonized and more stable material. The strong attenuation or disappearance of O−H and aliphatic C−H bands indicates dehydration and devolatilization processes, in agreement with the significant reduction in volatile matter observed in proximate analysis and the decrease in hydrogen and oxygen contents in elemental analysis (Lu, 2002; Tomczyk; Sokołowska; Boguta, 2020). Similarly, the reduction of the carbonyl band (~1730 cm^{-1}) confirms the thermal degradation of hemicellulose and cleavage of ester linkages. In contrast, the relative intensification of the band near 1580-1600 cm^{-1} indicates the formation of condensed aromatic structures, consistent with the decrease in H/C and O/C ratios and the increase in fixed carbon content. These changes reflect the development of a more aromatic and thermally stable carbon matrix (Goshadrou; Karimi; Lefsrud, 2013; Jindo *et al.*, 2014).

The FTIR results are also in strong agreement with the XRD findings. While the RP diffractogram shows a predominance of amorphous lignocellulosic phases, the PB pattern is marked by sharp diffraction peaks attributed to crystalline inorganic phases such as silica and carbonates. This mineral enrichment is corroborated in FTIR by the increased intensity of bands in the low-wavenumber region (700-450 cm^{-1}), associated with Si−O and metal-oxygen vibrations (Goshadrou; Karimi; Lefsrud, 2013; Tomczyk; Sokołowska; Boguta, 2020). These observations confirm that pyrolysis not only promotes organic matter degradation and aromatization but also leads to the concentration and structural reorganization of inorganic constituents, as indicated by the increase in ash content from proximate analysis.

From an adsorption standpoint, the integration of these techniques reveals a clear shift in the dominant mechanisms. In RP, the abundance of hydroxyl and oxygenated groups suggests that adsorption is mainly governed by hydrogen bonding and polar interactions. In contrast, PB exhibits multifunctional adsorption behavior resulting from its heterogeneous structure, that is, the aromatic carbon domains favor π−π interactions with methylene blue molecules, while residual oxygenated groups and mineral phases contribute to electrostatic interactions, surface complexation, and ion exchange. The increase in fixed carbon and aromaticity, combined with mineral-induced surface heterogeneity, enhances the overall adsorption potential of the biochar (Goshadrou; Karimi; Lefsrud, 2013; Jindo *et al.*, 2014; Tomczyk; Sokołowska; Boguta, 2020).

Activated carbons typically exhibit highly carbonized structures with low H/C and O/C ratios, similar to PB; however, their FTIR spectra generally show fewer functional groups due to extensive thermal and chemical activation, and their XRD patterns are dominated by broad bands associated with turbostratic carbon rather than distinct mineral peaks (Jindo *et al.*, 2014;

Marsh *et al.*, 2006). In contrast, the PB in this study retains a greater diversity of surface functionalities and a significant mineral fraction, as evidenced by both FTIR and XRD. While activated carbon adsorption is primarily driven by its high surface area and microporosity, PB combines multiple adsorption mechanisms due to its chemical heterogeneity and mineral content.

5.5 SEM/EDS

The SEM micrographs of the raw petiole (RP) and the corresponding biochar (PB) are presented in Figure 11, allowing the visualization of morphological transformations induced by carbonization.

Figure 11 - SEM micrographs: (a) RP at 30x magnification, (b) RP at 1000x magnification, (c) PB at 80x magnification and (d) PB at 600x magnification.

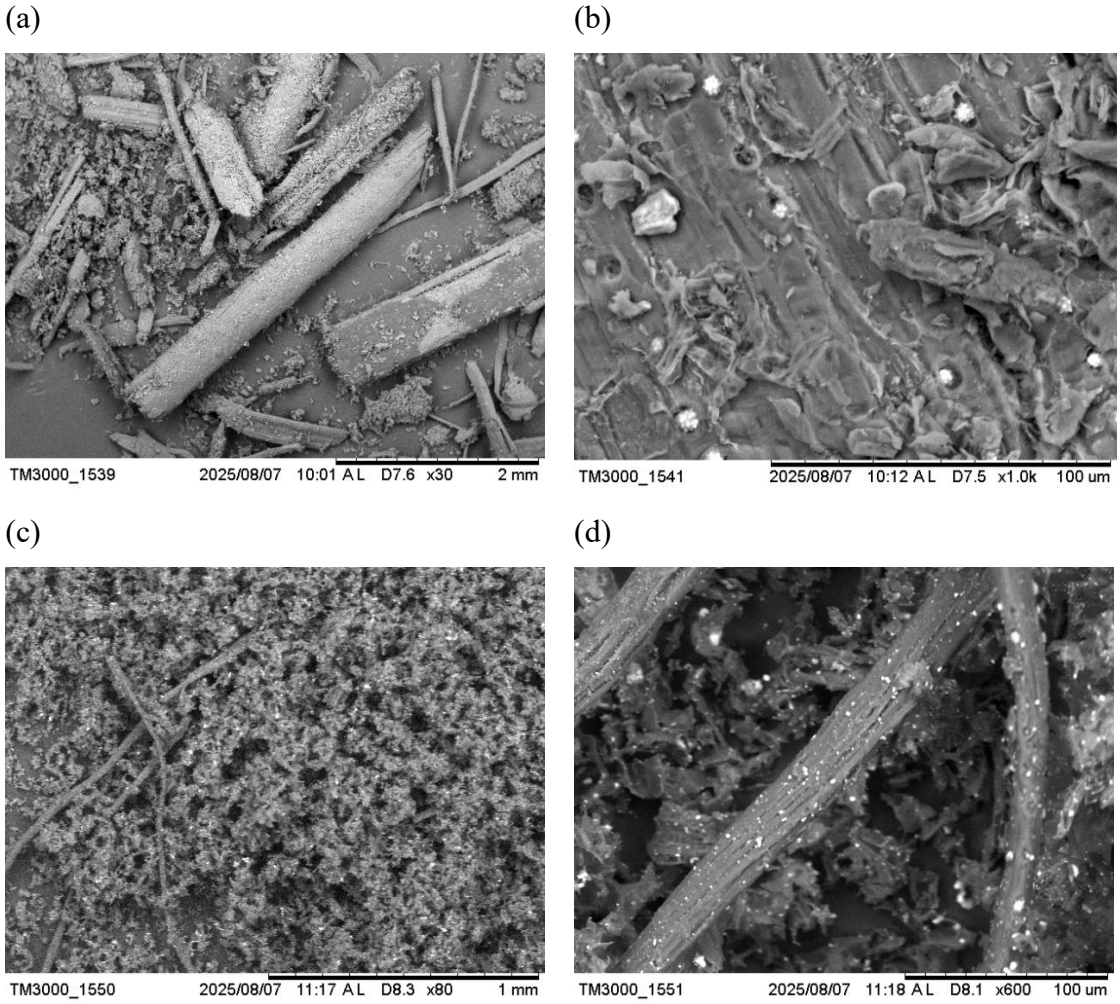

Source: Autor.

The SEM images of RP, shown in Figure 11 (a–b), display the characteristic morphology of a lignocellulosic material, consisting of elongated fibrous structures and relatively compact

domains. In the lower-magnification image (Figure 11–a), the preservation of vascular bundles and fibrous elements can be clearly observed. At higher magnification (Figure 11–b), the surface appears dense and comparatively smooth, with little apparent porosity. Small silica-rich particles, probably corresponding to phytoliths, are also visible dispersed throughout the biomass matrix.

This morphological pattern reflects the preservation of cellulose microfibrils surrounded by a matrix composed of hemicellulose and lignin, which is consistent with high volatile matter content (77.77%), the elevated O/C and H/C atomic ratios, and the abundance of oxygen-containing functional groups identified by FTIR, such as O−H, C=O, and C−O (Reza *et al.*, 2020; Xu, R. *et al.*, 2023). The relatively smooth and dense surface, with limited visible porosity, also aligns with the partially crystalline and amorphous domains detected in the XRD pattern of RP, where cellulose-related reflections coexist with a broad amorphous halo.

Following pyrolysis, morphology undergoes substantial modifications, as observed in the micrographs of PB, Figure 11 (c−d). The well-organized fibrous structure of the biomass is disrupted, giving rise to a more irregular, fragmented, and homogeneous surface. In which, it can be noted that the biochar exhibits greater roughness and the development of microscopic and mesoscopic voids, resulting from the thermal decomposition of groups of biopolymers, and the release of volatile compounds (Ramola *et al.*, 2022; Zhao, S. X.; Ta; Wang, 2017). This structural rearrangement agrees with the reductions in volatile matter and oxygen content observed in the proximate and elemental analyses, and with the collapse of the ordered organic domains identified in the XRD results, as well as in other biochars found in the literature. Thus, the resulting porous and disordered carbon matrix increases the accessibility of the surface and facilitates the diffusion of adsorbed molecules, which is crucial for adsorption performance (Morales-Paredes *et al.*, 2023; Ramola *et al.*, 2022).

The EDS data is summarized in Table 7, which provides complementary information on the chemical transformations induced by carbonization.

Table 7 - EDS for RP and PB.

Sample	Si (%wt)	K (%wt)	Cl (%wt)	Ca (%wt)	S (%wt)	Mg (%wt)	Na (%wt)
RP	14.03	23.67	27.50	5.56	—	3.72	—
PB	4.58	29.33	27.81	6.70	2.24	7.28	—

Source: Autor.

The EDS data presented in Table 7 confirms the compositional changes, highlighting the decrease in oxygen content and the relative enrichment of mineral constituents. An increase in potassium (23.68 → 29.33 wt%), calcium (5.56 → 6.70 wt%), and magnesium (3.73 → 7.28 wt%) can be observed, reflecting the concentration of non-volatile inorganic species as the organic fraction is progressively removed (Elnour *et al.*, 2019; Ramola *et al.*, 2022). At higher magnification, Figure 11 − (b), the presence of silica-rich phytoliths dispersed within the lignocellulosic matrix is evident, where these structures are consistent with the relatively high silicon content detected by EDS (14.03 wt%) and contribute to the mechanical rigidity of the biomass.

Additionally, the appearance of sulfur in PB (2.25 wt%) suggests the formation or stabilization of sulfur-containing groups during pyrolysis, potentially contributing to surface reactivity. These compositional changes corroborate the FTIR observations in the low-wavenumber region (Si−O and metal−O vibrations) and reinforce the interpretation of a mineral-enriched biochar matrix (Morales-Paredes *et al.*, 2023; Ramola *et al.*, 2022; Reza *et al.*, 2020).

Another important feature observed in the PB microstructure, Figure 11 − (d), is the presence of mineral aggregates dispersed throughout the carbon matrix. This observation is strongly supported by proximate analysis and EDS, which indicate a substantial increase in ash content (from 3.63% to 27.45%) and an enrichment of inorganic elements such as K, Ca, and Mg (Elnour *et al.*, 2019; Zhao, S. X.; Ta; Wang, 2017). These findings are also consistent with the XRD results, where sharp and well-defined peaks were attributed to crystalline mineral phases such as carbonates and silicates. The decrease in silicon content (14.03 → 4.58 wt%) is associated with the redistribution or partial transformation of silica phases during pyrolysis, possibly linked to structural rearrangements or partial volatilization. Meanwhile, chlorine remains relatively constant, indicating the retention of inorganic salts intrinsic to the biomass (Elnour *et al.*, 2019; Morales-Paredes *et al.*, 2023). Overall, these results confirm that carbonization leads to a mineral-enriched carbon matrix.

From an adsorption mechanisms perspective, the integration of morphological, structural, and compositional characteristics provides a comprehensive understanding of PB behavior. The increased roughness and porosity favor physical adsorption and intraparticle diffusion, while the aromatic carbon domains — evidenced by low H/C ratios and enhanced C=C bands — promote π−π and π−cation interactions with methylene blue molecules. In parallel, the mineral fraction introduces additional mechanisms, including ion exchange and electrostatic

interactions, particularly relevant for cationic species. Thus, unlike RP, where adsorption is mainly governed by polar functional groups, PB exhibits a synergistic adsorption behavior combining carbon-based interactions and mineral-mediated processes.

When compared to activated carbon, the PB biochar exhibits both convergent and divergent characteristics. Activated carbons typically present highly developed microporosity, large specific surface areas, and low ash content, resulting in adsorption dominated by pore-filling and π–π interactions. In contrast, the biochar produced in this study presents a more heterogeneous structure, with moderate porosity and a significant mineral fraction. While activated carbon adsorption is largely governed by pore-filling and π–π interactions, the PB combines these mechanisms with mineral-mediated processes, such as ion exchange and surface charge interactions. Studies have shown that mineral-rich biochars can exhibit comparable or even superior adsorption performance for cationic dyes under certain conditions, particularly due to the contribution of inorganic phases and surface heterogeneity. Therefore, the PB biochar derived from carnauba petiole can be interpreted as a multifunctional adsorbent, whose performance arises from the combined effects of structural carbon evolution and inorganic phase enrichment.

5.6 Thermal Analysis

Through thermogravimetric analyses, relevant information was obtained regarding the decomposition behavior of organic constituents, the endothermic and exothermic reactions associated with pyrolysis, and the thermal stability of the petiole-derived material. The thermograms obtained from thermogravimetric (TG), derivative thermogravimetric (DTG), and differential thermal analysis (DTA) of raw petiole and the corresponding petiole biochar are presented in Graphic 6 (a–c). Panels (a) and (b) correspond to the TG/DTG curves of the biomass and biochar, respectively, and panels (c) and (d) display the DTA curves of the same samples, highlighting the thermal transformations associated with each material.

Graphic 6 - Thermograms for RP & PB: (a) TGs, (b) DTGs and (c) DTAs.

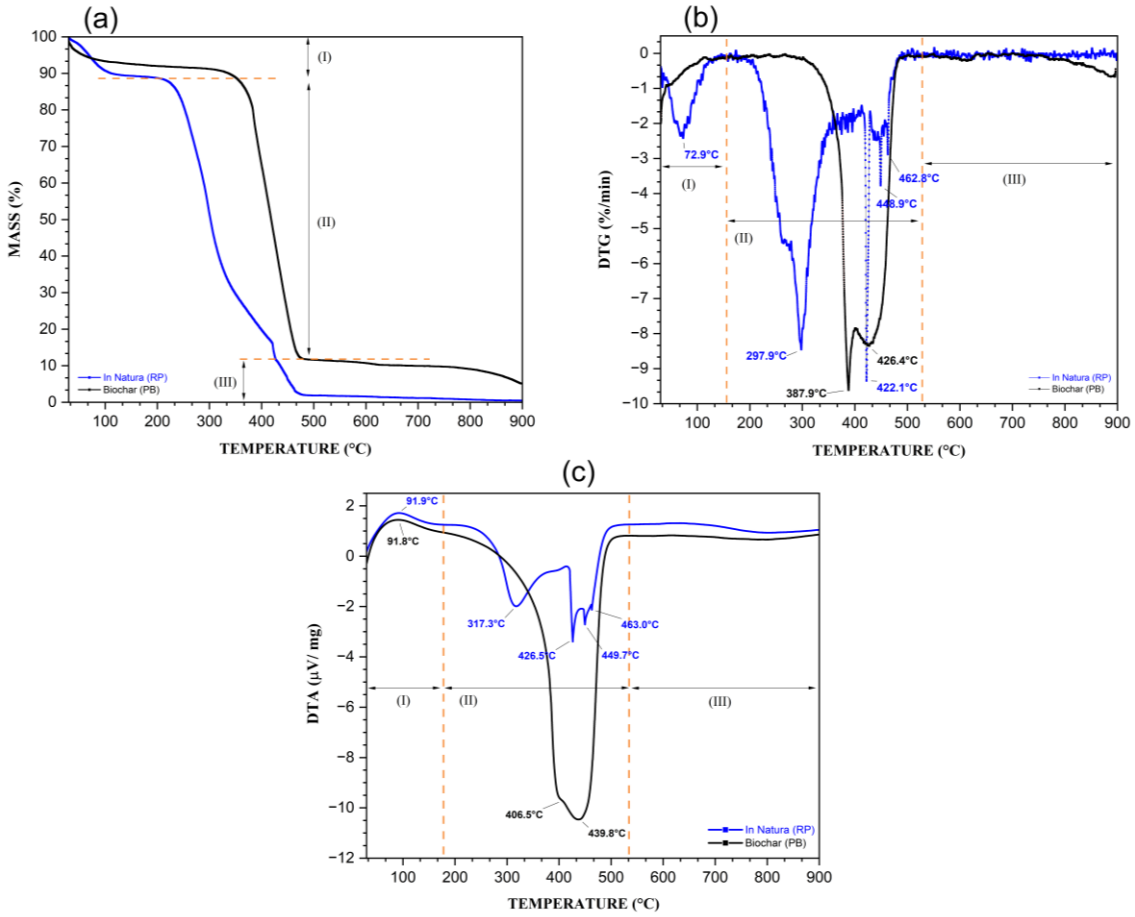

Source: Autor.

The main thermal parameters observed in the thermograms are summarized in Table 8.

Table 8 - Parameters associated with thermal events identified in the TG/DTG and DTA analyses.

Sample	Region I			Region II			Region III		
	Δ [a]	T_{max} [b]	V_{max} [c]	Δ [a]	T_{max} [b]	V_{max} [c]	Δ [a]	T_{max} [b]	V_{max} [c]
RP	10.73 %	72.5 °C	−2.41 %/min	87.11 %	422.1 °C	−9.34 %/min	1.71 %	—	—
PB	7.88 %	68.5 °C	−1.99 %/min	81.88 %	387.9 °C	−9.61 %/min	5.13 %	—	—

[a] Mass loss rate (in percentage)

[b] Maximum degradation temperature (°C)

[c] Maximum reaction rates (%/min)

Source: Autor.

Through careful analysis, it is observed region I (≈ 30 − 200 °C) is primarily associated with dehydration and the release of low-molecular weight volatile compounds, representing the initial stage of thermal evolution for both materials. In this temperature range, the RP exhibits

a more pronounced mass loss (Δ = 10.7%) compared to PB (Δ = 7.8%), which can be directly attributed to its higher moisture content and the abundance of thermally labile oxygenated groups inherent to the lignocellulosic structure (Fernandes *et al.*, 2011; Ribeiro Filho *et al.*, 2024). This behavior is further supported by the DTG profiles, where peaks at 72.5 °C (RP) and 68.5 °C (PB), combined with subtle endothermic signals in the DTA curves, confirm that the dominant processes involve water evaporation and the release of weakly bound volatiles. Therefore, the comparatively lower intensity observed for PB reflects the prior removal of these components during pyrolysis, reinforcing the interpretation that carbonization significantly reduces the presence of volatile matter, as previously indicated by proximate and elemental analyses (Fernandes *et al.*, 2011; Ram *et al.*, 2014).

Pronouncedly, region II (≈ 200 – 550 °C) represents the main stage of thermal degradation and clearly highlights the structural differences between RP and PB. In the case of the raw biomass, this region is characterized by an intense and rapid mass loss (Δ = 87.1%), indicative of the progressive decomposition of its lignocellulosic constituents. The DTG curve reveals distinct and well-defined peaks corresponding to the sequential degradation of hemicellulose (≈ 270 – 300 °C), followed by cellulose (≈ 390 – 420 °C), and finally lignin, which decomposes over a broader temperature range (Fernandes *et al.*, 2011; Ram *et al.*, 2014). These transformations are accompanied by pronounced exothermic events in the DTA curve, reflecting the energetic nature of bond cleavage and depolymerization reactions within the organic matrix. Altogether, this stage evidences the intrinsic thermal instability of untreated biomass and its high content of reactive, oxygen-rich components (Chen, M., 2016).

In contrast, the thermal behavior of PB within this same temperature interval is markedly different, reflecting the structural transformations induced by carbonization. Although a significant mass loss is still observed (Δ = 81.8%), the DTG profile becomes broader and less defined, with a main degradation peak centered around 391.2 °C. The lack of well-defined peaks attributable to hemicellulose and cellulose indicates that these components were extensively degraded during pyrolysis and no longer remain as separate phases with distinguishable thermal behavior. Instead, the thermal response is governed by the decomposition of more stable carbonaceous structures, primarily derived from lignin and newly formed aromatic domains (Bizerra *et al.*, 2023; Chen, M., 2016). This interpretation is further supported by the DTA curve, which exhibits broader and less intense exothermic events, consistent with a more condensed and thermally resistant structure. Furthermore, the displacement and widening of these thermal events may also be associated with the presence of

inorganic species such as K, Ca, and Mg, which can act as catalysts during thermal decomposition by facilitating bond cleavage and inducing structural rearrangements within the carbonaceous matrix.

Lastly, region III (≈ 550 – 900 °C) corresponds to the final stage of thermal stabilization, where both materials approach a relatively inert state. In this region, RP shows minimal additional mass loss (Δ = 1.7%), indicating that most of its organic constituents have already been decomposed in the previous stages. Similarly, the biochar still exhibits a small but noticeable mass loss (Δ = 5.1%), which can be associated with the gradual decomposition of residual carbon structures and possible transformations of mineral phases, such as the decomposition of carbonates (Ram *et al.*, 2014; Ribeiro Filho *et al.*, 2024). In addition, the absence of significant DTG peaks and the stabilization of the DTA signal confirms that no major thermal events occur in this range. Importantly, the reduced reactivity and enhanced resistance of PB at high temperatures reflect the formation of a more stable carbon framework, which is consistent with the increased fixed carbon content, reduced H/C and O/C ratios, and the development of disordered aromatic domains identified in previous analyses (Bizerra *et al.*, 2023; Fernandes *et al.*, 2011).

From a comparative perspective, the thermal profiles clearly demonstrate that carbonization promotes a substantial increase in the thermal stability of the material. While RP is dominated by the decomposition of labile lignocellulosic components, PB exhibits a more gradual and energetically attenuated degradation behavior, characteristic of condensed carbon structures. This transition is fully consistent with the transformations identified by proximate analysis, elemental composition, FTIR, and XRD, all of which indicate the evolution from a volatile-rich, oxygenated matrix to a more aromatic and mineral-enriched carbon material.

As a result, these thermal characteristics have direct implications for adsorption performance. The formation of a thermally stable and structurally rigid carbon matrix in PB enhances the persistence of aromatic domains, which are essential for π–π interactions with methylene blue molecules. At the same time, the retention and concentration of inorganic constituents contribute to surface heterogeneity and enable additional mechanisms such as ion exchange and electrostatic interactions. In contrast, activated carbons are typically characterized by extremely high thermal stability, minimal mass loss above 400 °C, and highly developed microporous structures resulting from physical or chemical activation processes.

In comparison, the PB exhibits broader degradation features and residual mass loss at higher temperatures, indicating a less ordered carbon structure (Ram *et al.*, 2014). However, unlike

activated carbon, PB retains a significant mineral fraction, which introduces additional functionalities that can enhance adsorption through mechanisms beyond simple pore filling. Therefore, PB may be considered a thermally stable and multifunctional adsorbent, whose performance arises from the combined effects of aromatic carbon domains and mineral-mediated interactions.

5.7 Adsorption Tests

The adsorption of methylene blue (MB) onto PB was examined under controlled experimental conditions by assessing the influence of adsorbent dosage, contact time, and initial dye concentration. The sensitivity of the process to these operational variables indicates that adsorption is strongly affected by the accessibility of the surface and the gradual occupation of the available active sites. Taken together, the kinetic and equilibrium results point to a combined adsorption mechanism characterized by a fast initial uptake at the external surface, followed by a slower stage governed by diffusion within the porous network and adsorption onto sites with different energy levels.

5.7.1 Biochar Dosage Variation

Graph 7 shows the relationship between the effect of biochar dosage (PB) on adsorption capacity (q_e) and methylene blue (MB) removal efficiency. A clear and systematic trend is observed, in which q_e decreases with increasing adsorbent dosage, while the overall removal efficiency increases. At the lowest dosage (2 mg), the system exhibits the highest adsorption capacity (32.5 $mg \cdot g^{-1}$) but the lowest removal efficiency (8.66%). Conversely, at the highest dosage (25 mg), q_e decreases to 7.3 $mg \cdot g^{-1}$, whereas removal efficiency reaches its maximum value (27.83%). This inverse relationship between q_e and removal percentage is common characteristic of batch adsorption systems and reflects the interplay between adsorbent mass and solute availability.

Graphic 7- Adsorption behavior of PB at varying adsorbent dosages, presented in terms of equilibrium adsorption capacity (qe) and MB removal efficiency (%).

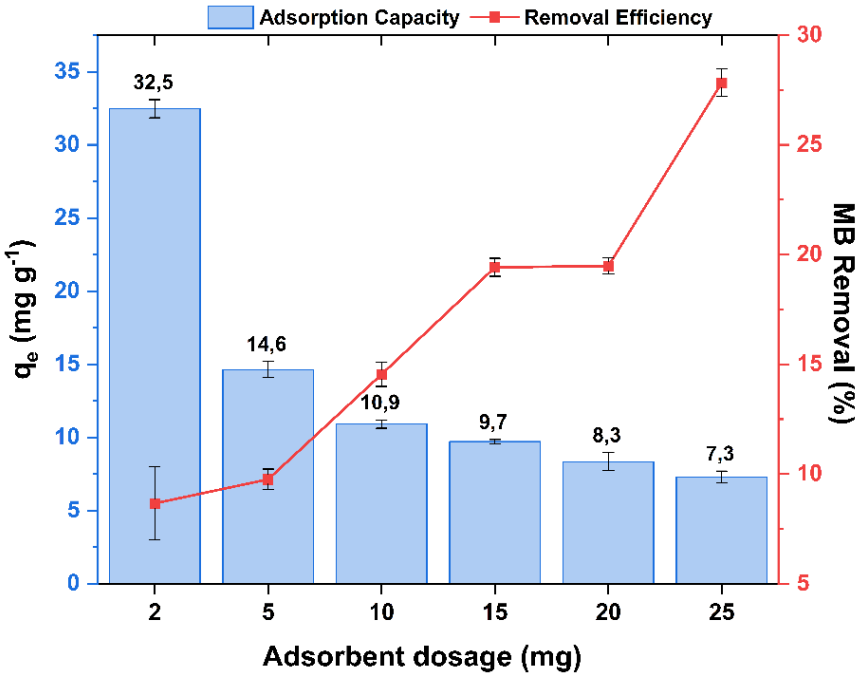

Source: Autor.

The observed behavior can be fundamentally explained by mass balance considerations under limited solute conditions. As the adsorbent dosage increases, the number of available adsorption sites increases proportionally; however, the total amount of dye in solution remains constant (da Gama *et al.*, 2024; Wang *et al.*, 2023). Consequently, the available MB molecules are distributed over a larger mass of adsorbent, leading to a reduction in adsorption capacity per unit mass (q_e). At the same time, the increase in the total available surface area promotes greater absolute absorption of the dye, resulting in improved removal efficiency. Therefore, the observed trends do not indicate changes in the intrinsic adsorption mechanisms, but rather a redistribution effect governed by the adsorbent/adsorbate ratio (da Gama *et al.*, 2024).

A more detailed examination shows that the removal efficiency increases progressively as the adsorbent dosage rises from 2 to 15 mg, followed by an apparent stabilization between 15 mg (19.42%) and 20 mg (19.48%). This near-constant behavior indicates that the system is approaching equilibrium, where the increase in adsorbent mass is nearly offset by the continuous decline in adsorption capacity (q_e), resulting in similar overall amounts of methylene blue removed. Within this dosage interval, the process becomes increasingly constrained by the limited concentration of MB in solution rather than by the number of available adsorption sites (da Gama *et al.*, 2024; Mohan *et al.*, 2014). Consequently, the higher removal efficiency observed at 25 mg does not necessarily indicate a substantial enhancement in adsorption

performance, but rather reflects a shift in the mass balance, in which the additional adsorbent mass is no longer completely counterbalanced by the reduction in q_e, thereby enabling a greater total uptake of dye.

Furthermore, it is worth highlighting that the monotonic decrease in q_e across the entire dosage range indicates that there is no improvement in intrinsic adsorption efficiency at higher dosages. Phenomena frequently associated with high adsorbent loadings, such as particle aggregation or diffusion boundary layer overlap, which typically reduce adsorption performance, are not necessary to explain the observed behavior (Ahmad *et al.*, 2020; Wang *et al.*, 2023). Instead, the results are consistent with classical adsorption trends reported for biochar systems, where adsorption performance is primarily controlled by the ratio between adsorbent mass and solute concentration under batch conditions.

From a comparative standpoint, the behavior observed for PB is consistent with that reported for lignocellulosic biochars, which commonly exhibit decreasing q_e and increasing removal efficiency with increasing dosage due to site underutilization at higher solid loadings (Ahmad *et al.*, 2020; Mohan *et al.*, 2014). However, when compared to activated carbons, some distinctions become evident, the PB biochar shows a more pronounced decline in q_e, which may be attributed to its lower surface area and the presence of mineral phases that, although contributing to adsorption via electrostatic and ion-exchange mechanisms, do not compensate for the reduced availability of high-energy adsorption sites typical of activated carbons.

On the other hand, the mineral-rich nature of PB may confer advantages in specific systems, particularly for cationic dyes such as methylene blue. As a result, despite its lower q_e compared to activated carbons, PB can achieve competitive removal efficiencies under optimized conditions, especially in systems where surface heterogeneity and multiple interaction mechanisms play a significant role. Therefore, the adsorption behavior of PB reflects a balance between carbon-based interactions (π–π) and mineral-mediated processes, distinguishing it from both conventional activated carbons and less functionalized biochars (da Gama *et al.*, 2024; Mohan *et al.*, 2014).

5.7.2 Contact Time Variation

Graphic 8 illustrates the adsorption kinetics of methylene blue onto PB, showing the evolution of adsorption capacity (q_t) as a function of contact time, along with the fitted kinetic models (PFO, PSO, Elovich, and Weber–Morris). The kinetic profile exhibits the typical two-step behavior commonly observed in adsorption systems, characterized by an initial stage of rapid dye uptake followed by a more gradual progression toward equilibrium. In the first

minutes of contact, q_t increases markedly, reaching 4.96 $mg \cdot g^{-1}$ after 5 min and 8.42 $mg \cdot g^{-1}$ after 15 min, which reflects the abundance of readily accessible active sites and the strong mass transfer driving force generated by the concentration difference between the bulk solution and the adsorbent surface. This fast initial stage is typically associated with external surface adsorption and boundary layer diffusion. As time progresses, the rate of adsorption gradually decreases, reaching 12.16 $mg \cdot g^{-1}$ at 60 min and approaching equilibrium values of 15.13 $mg \cdot g^{-1}$ at 240 min. This second stage reflects the progressive occupation of active sites and the increasing importance of intraparticle diffusion and pore accessibility limitations.

Graphic 8 – Time dependent adsorption behavior of MB onto PB, expressed as adsorption capacity as a function of contact time.

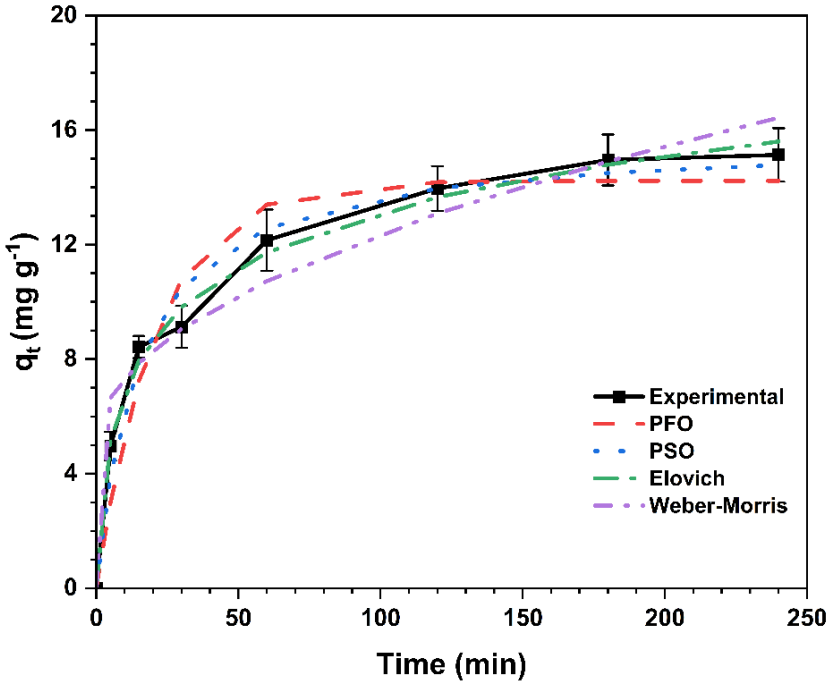

Source: Autor.

The kinetic parameters summarized in Table 9 provide further insight into the adsorption mechanism.

Table 9 - Kinetic parameters obtained for the adsorption of MB onto PB.

MODEL TYPE	PARAMETER	PB
Experimental	q_e (mg/g)	15.13
Pseudo-First Order (PFO)	q_e (mg/g)	14.23
	k_1 (h^{-1})	0.047

	R^2	0.87
Pseudo-Second Order (PSO)	q_e (mg/g)	15.70
	k_2 (g/mg·h)	0.0043
	h (mg/g·h)	1.06
	R^2	0.95
Elovich	α (mg/g·h)	2.98
	β (g/mg)	0.35
	R^2	0.98
Intraparticle Diffusion (Weber–Morris)	K_p (mg/g·$h^{1/2}$)	0.73
	C (mg/g)	5.01
	R^2	0.91

Source: Autor.

Among the evaluated models, the PSO and Elovich models exhibited the best fit to the experimental data, with correlation coefficients (R^2 = 0.959 and 0.986, respectively) significantly higher than that of the PFO model (R^2 = 0.877). In addition, the equilibrium adsorption capacity predicted by the PSO model (q_e = 15.70 mg · g^{-1}) is in close agreement with the experimental value (15.13 mg · g^{-1}), reinforcing its suitability to describe the system. The good adjustment of the PSO model suggests that the adsorption rate is controlled by site-dependent interactions involving the availability of active sites, rather than solely by solute concentration in the liquid phase (Ahmad *et al.*, 2020; Mohan *et al.*, 2014). Meanwhile, the Elovich model, which assumes a heterogeneous surface with a distribution of activation energies, further supports the presence of energetically non-uniform adsorption sites, consistent with the structural complexity of biochar evidenced by FTIR, XRD, and SEM/EDS analyses.

It is worth noting that the intraparticle diffusion model (Weber–Morris) also provides relevant mechanistic information. Although the model shows a reasonable fit (R^2 = 0.913), the deviation from linearity and the non-zero intercept (C = 5.01 mg · g^{-1}) indicate that intraparticle diffusion is not the only rate-limiting step. Instead, adsorption occurs through multiple sequential mechanisms, including surface and pore diffusion (da Gama *et al.*, 2024; Wang *et al.*, 2023). This behavior is typical of biochar-based adsorbents, whose heterogeneous structure

combines micro-, meso-, and macroporous domains, along with various surface functionalities (Ahmad *et al.*, 2020).

From a mechanistic standpoint, the relatively fast initial uptake can be attributed to electrostatic attraction between the cationic MB molecules and negatively charged surface sites, as well as π–π interactions with aromatic domains formed during carbonization (as indicated by elemental analysis and FTIR). As adsorption progresses, the contribution of intraparticle diffusion becomes more significant, reflecting the role of the porous structure observed in SEM images. Additionally, mineral components identified by EDS and XRD (e.g., K, Ca, Mg) may contribute to secondary mechanisms such as ion exchange and surface complexation, further enhancing adsorption performance. Therefore, the adsorption process is best described as a synergistic combination of physisorption and surface-controlled interactions occurring on a heterogeneous matrix.

A critical comparison with activated carbon and other lignocellulosic biochars highlights important aspects of PB's performance. PB biochar reaches equilibrium in approximately 180-240 minutes, which is consistent with values reported for non-activated biochars derived from lignocellulosic residues (Ahmad *et al.*, 2020; Marsh *et al.*, 2006). However, although slower than activated carbon, this kinetic behavior is comparable to or even more favorable than other biochars, particularly considering the absence of chemical or physical activation. Furthermore, good fit for the PSO and Elovich models is widely reported for both activated carbons and biochars in the adsorption of cationic dyes, indicating that surface heterogeneity and site-dependent interactions are common characteristics of these materials (Mohan *et al.*, 2014; Wang *et al.*, 2023). Thus, unlike activated carbons — where adsorption is predominantly governed by micropore filling and π–π interactions — PB biochar exhibits a more complex adsorption mechanism, involving not only carbonaceous domains but also mineral phases that contribute to electrostatic and ion-exchange interactions. This multifunctional behavior may compensate, to some extent, for the smaller surface area typically observed in biochars, making PB a competitive and economical adsorbent for dye removal.

5.7.3 MB Concentration Variation

Graphic 9 presents the equilibrium adsorption isotherms of methylene blue onto biochar, correlating the adsorption capacity (q_e) with the equilibrium concentration (C_e). The experimental results reveal a continuous, non-linear increase in the equilibrium adsorption capacity (q_e), rising from 7.39 $mg \cdot g^{-1}$ to 129.45 $mg \cdot g^{-1}$ as the equilibrium concentration (C_e) increases. This behavior reflects the gradual filling of the available adsorption sites on the PB

surface. At low concentrations, the pronounced rise in q_e indicates a strong affinity between methylene blue molecules and the adsorbent, attributable to the abundance of easily accessible active sites. As C_e becomes higher, the slope of the isotherm progressively decreases, indicating the partial saturation of these sites and a greater contribution of interactions among adsorbed dye molecules.

Graphic 9 - Adsorption isotherms of MB onto PB.

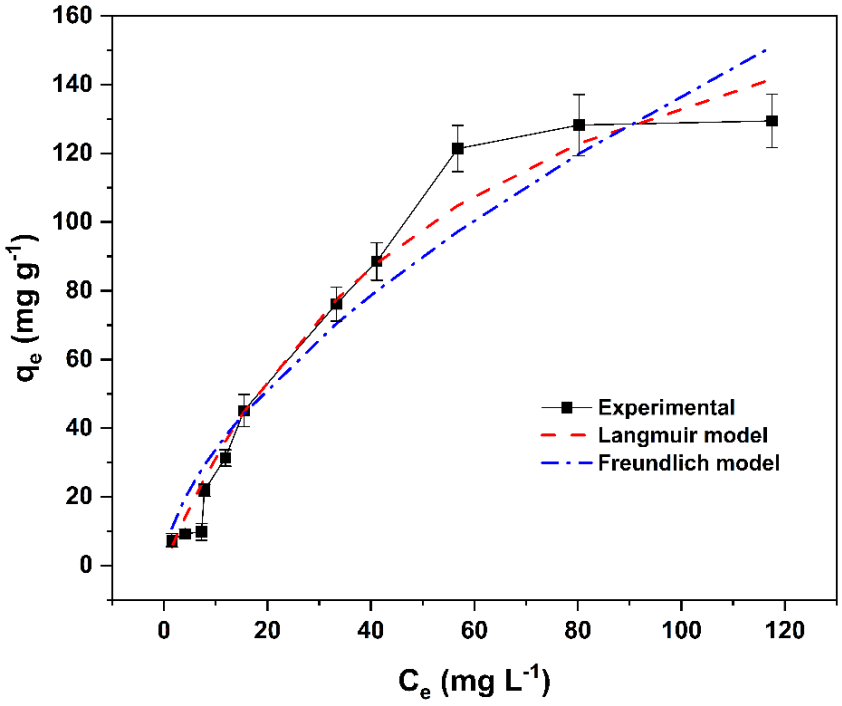

Source: Autor.

The isotherm parameters summarized in Table 10 provide further insight into the adsorption process.

Table 10 - Parameters estimated from fitting the adsorption isotherm models to MB equilibrium data.

MODEL TYPE	PARAMETER	PB
Langmuir	q_m (mg/g)	210.66
	K_L (L/mg)	0.01744
	R^2 (a)	0.971
	R_L (b)	0.27 – 0.96
Freundlich	K_F (c)	8.41
	n (d)	1.65

	R^2 (a)	0.928

(a) Coefficient of determination (dimensionless)
(b) Langmuir separation factor (dimensionless)
(c) Freundlich constant [(mg/g)·(L/mg)$^{1/n}$]
(d) Heterogeneity factor (dimensionless)

Source: Autor.

As we can see from the graph, the Langmuir model exhibited a better fit to the experimental data (R^2 = 0.971) compared to the Freundlich model (R^2 = 0.928), indicating that, from a mathematical standpoint, the equilibrium data are well described by a model assuming finite adsorption capacity. It is worth noting that the maximum adsorption capacity estimated by the Langmuir model (q_m = 210.66 mg·g^{-1}) substantially exceeds the highest value obtained experimentally (129.45 mg·g^{-1}). This difference suggests that full monolayer coverage was not achieved within the concentration range investigated, and therefore q_m should be regarded as a theoretical parameter obtained by model extrapolation rather than as an experimentally attained capacity (Avom *et al.*, 1997; Gouamid; Ouahrani; Bensaci, 2013). In addition, the Langmuir separation factor (R_L = 0.27−0.96) indicates that methylene blue adsorption onto PB is favorable throughout the range of concentrations evaluated.

Although the Langmuir model provides the best statistical fit, the Freundlich parameters offer important complementary insight into the heterogeneous nature of the PB surface. The Freundlich constant (K_F = 8.41) and heterogeneity factor (n = 1.65) indicate favorable adsorption (n > 1) and confirm that the surface is energetically non-uniform, which is consistent with the multitechnique characterization revealing a complex matrix composed of aromatic carbon domains, residual functional groups, and mineral phases (Avom *et al.*, 1997; de Oliveira *et al.*, 2025). From a mechanistic standpoint, this heterogeneity implies that adsorption cannot be strictly described as ideal monolayer coverage; instead, it involves a combination of interactions, including π–π stacking between MB molecules and aromatic structures, electrostatic attraction with negatively charged sites, and possible contributions from mineral components via ion exchange or surface complexation. This synergistic behavior is further reflected in the isotherm profile, where adsorption is initially dominated by high-energy sites at low concentrations and progressively shifts toward lower-energy sites and potential multilayer contributions as these sites become occupied (de Oliveira *et al.*, 2025; Gouamid; Ouahrani; Bensaci, 2013).

▪ **PART II**

5.8 Statistical Analysis of Milled Samples via Response Surface Methodology

The application of Response Surface Methodology (RSM) in the statistical analysis of the milled samples is justified by the need to systematically evaluate the combined effects of process variables — milling time, rotational speed, and the resulting specific energy input — on the adsorption performance of the materials. High-energy ball milling is inherently a multivariable process in which interactions between parameters can produce non-linear and non-intuitive effects on structural, textural, and surface properties (Chen, S. *et al.*, 2022; Kovalchuk *et al.*, 2023). In this context, RSM provides a robust and efficient statistical framework to model these interactions, identify significant factors, and determine optimal processing conditions while minimizing the number of experimental runs.

Graphics 10 (a–b) shows the relationship between adsorption capacity and milling energy for the biochar (PB) and clay–biochar composite (B-PB) samples, allowing a direct evaluation of how the mechanical energy input influences the adsorptive performance of the materials. The energy parameter, calculated as a function of milling time and rotation speed, Graphics 10 (c), provides an integrated perspective of the processing intensity, enabling a more comprehensive interpretation compared to isolated variables.

Graphic 10 - Contour plots for (a) PBs, (b) B-PBs, and (c) adsorption capacity as a function of specific milling energy for PBs and B-PBs.

(a)

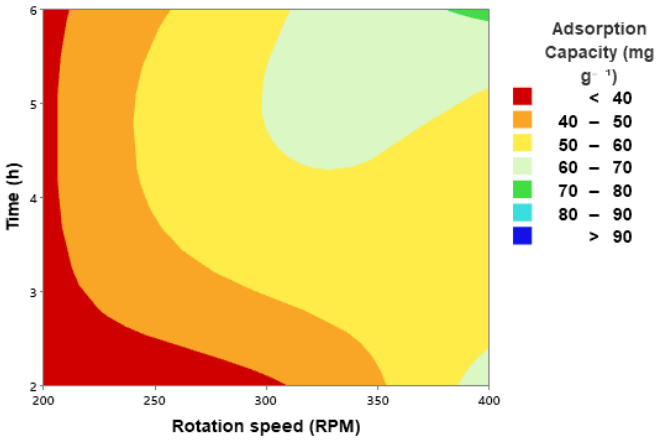

(b)

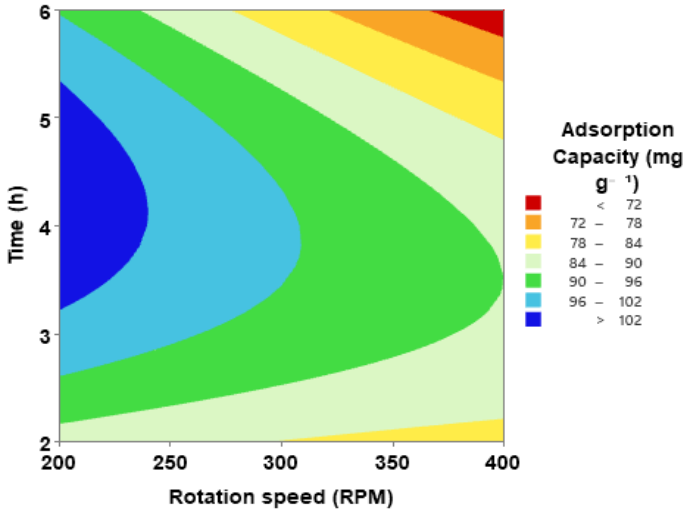

(c)

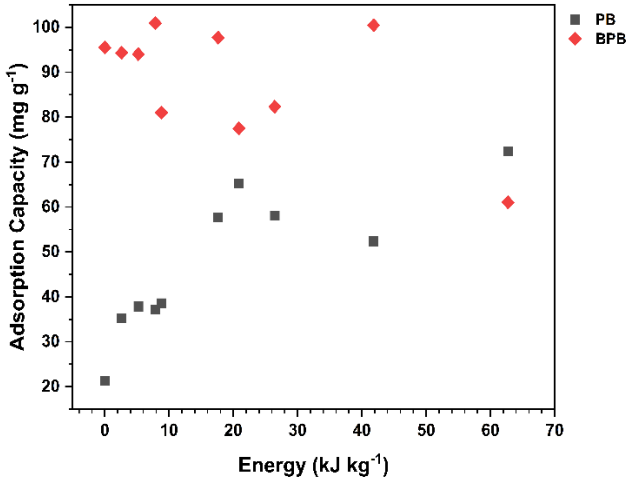

Source: Autor.

For the biochar samples (PB), a general increasing trend in adsorption capacity is observed with increasing milling energy, although with some fluctuations. The untreated material (0 $kJ \cdot kg^{-1}$) exhibited a relatively low adsorption capacity (21.33 $mg \cdot g^{-1}$), while the application of mechanical treatment significantly enhanced performance. At intermediate energies (17.64–26.46 $kJ \cdot kg^{-1}$), adsorption capacity increased to approximately 57–58 $mg \cdot g^{-1}$, indicating that structural modifications such as particle size reduction and increased surface area contributed positively to adsorption. The highest performance was obtained at the maximum energy level (62.73 $kJ \cdot kg^{-1}$), reaching 72.39 $mg \cdot g^{-1}$ (PB406). According to researchers Kovalchuk et al., 2023, this behavior is consistent with the effects induced by high-energy ball milling on the material, which promotes pore development, the generation of structural defects, and the exposure of active sites within the biochar matrix, thereby enhancing the adsorption capacity.

On the other hand, the B-PB composite exhibits a markedly different behavior, with high adsorption capacity already observed in the untreated condition (95.50 $mg \cdot g^{-1}$). Unlike PB, the relationship between energy and adsorption is non-linear, with performance strongly dependent on the combination of milling parameters. While moderate energy inputs (e.g., 5.24−7.86 $kJ \cdot kg^{-1}$) maintain or slightly improve adsorption capacity (up to 98.75 $mg \cdot g^{-1}$ for B-PB206), excessive energy input leads to performance deterioration, as observed at 62.73 $kJ \cdot kg^{-1}$ (61.02 $mg \cdot g^{-1}$ for B-PB406). This decline can be attributed to excessive aggregation of clay particles, which reduces the accessibility of active sites (Hamzaoui *et al.*, 2015; Harindintwali *et al.*, 2023).

Thereby, the selection of samples for advanced characterization (PB202, PB406, B-PB206, and B-PB406) was strategically based on contrasting adsorption performances. PB202 and B-PB406 represent conditions with relatively low adsorption efficiency under their respective systems, while PB406 and B-PB206 correspond to optimal or near-optimal conditions. This approach enables a more robust interpretation of the structure property relationships by comparing extreme conditions, highlighting how milling energy influences both beneficial and detrimental modifications in the materials.

From a mechanistic standpoint, the distinct behaviors of PB and B-PB can be explained by their structural differences and the way milling energy influences each system. However, excessive milling can disrupt the lamellar structure of bentonite or promote particle agglomeration, ultimately reducing the availability of active sites. As a result, while higher energy generally improves the performance of biochar, composite systems require an optimized intermediate condition to preserve the synergistic interaction between biochar porosity and clay functionality. This behavior highlights milling energy as a critical parameter in controlling adsorption performance and reinforces the importance of process optimization in the development of high-performance adsorbents derived from lignocellulosic biomass and mineral additives.

5.9 XRD - Selected Samples

Graphic 11 presents the X-ray diffraction (XRD) patterns of selected samples (PB, PB202, PB406, B-PB206, and B-PB406), allowing a comparative evaluation of the structural organization of the biochar and biochar–bentonite composites after high-energy ball milling. The diffractogram highlights the main diffraction angles at 20.7°, 23.0°, 24.3°, 31.0°, 33.1°, 47.5°, 59.1°, 69.4°, 79.1°, and 88.4°, revealing contributions from both carbonaceous and mineral phases.

Graphic 11 - Diffractogram of the selected samples (PB, PB202, PB406, B-PB206 and B-PB406).

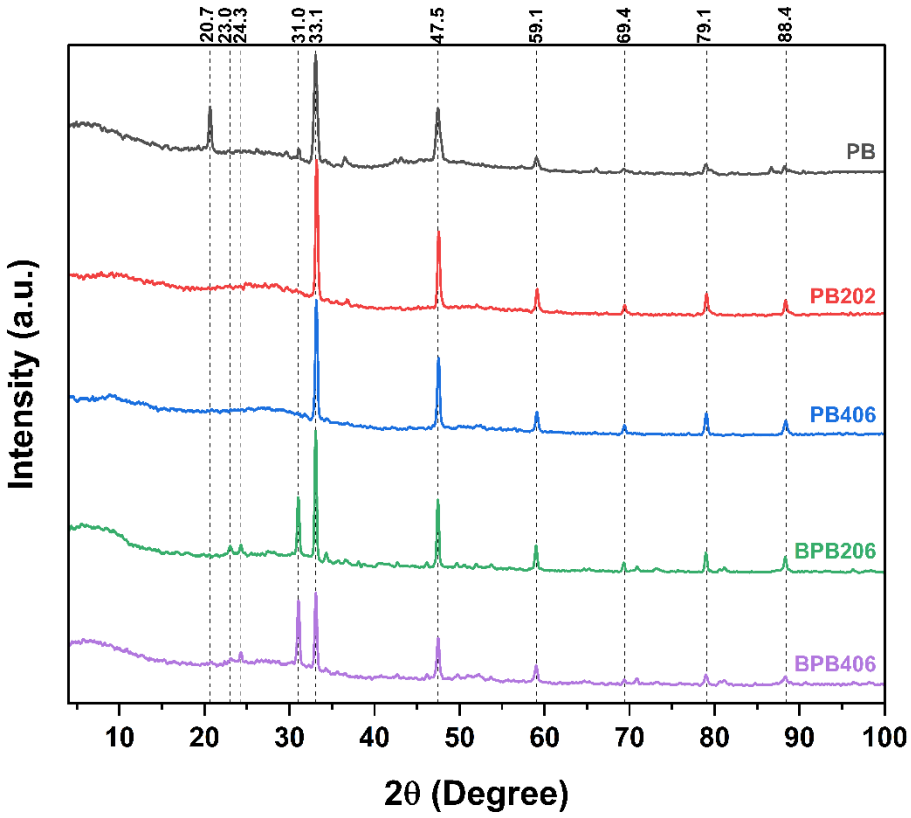

Source: Autor.

The PB exhibits a high-intensity peak centered around 20.7°, which is typically associated with the (002) plane of disordered carbon structures. This feature reflects the predominantly amorphous nature of lignocellulosic-derived biochars, characterized by turbostratic carbon arrangements and limited graphitic ordering (Sudhakaran; Rajan; Ravindranath, 2022; Zhao, F. *et al.*, 2023). After high-energy ball milling (PB202 and PB406), the interruption of this band indicates that the fundamental amorphous carbon structure is changed, although slight variations in peak intensity suggest subtle changes in structural ordering and defect density induced by mechanical treatment.

In addition to the amorphous carbon contribution, all samples display a pronounced diffraction peak at 33.1°, along with secondary reflections at 47.5°, 59.1°, 79.1°, and 88.4°. These peaks are commonly attributed to inorganic crystalline phases, such as mineral ash components (e.g., silica, calcite, or metal oxides) inherently present in biomass-derived biochars (Fosso-Kankeu E; Waanders F B, 2019; Shakir; Al-Yaqoobi, 2025). The consistent presence of these reflections across all samples indicates that ball milling does not eliminate these phases but may alter their dispersion and crystallite size. However, the effect of milling conditions can also be inferred from peak broadening and intensity variations. In general,

PB406 sample (higher milling severity) shows slightly reduced peak intensity compared to PB202, suggesting partial disruption of crystalline domains and increased structural disorder. A similar trend is observed for the composites, where B-PB406 presents less intense peaks than B-PB206, indicating that prolonged or more energetic milling may induce partial amorphization of the clay structure and improved dispersion within the biochar matrix. This structural modification is particularly relevant, as it may enhance the accessibility of active sites and contribute to improved adsorption performance (Fosso-Kankeu E; Waanders F B, 2019; Sudhakaran; Rajan; Ravindranath, 2022; Zhao, F. *et al.*, 2023).

The composite samples (B-PB206 and B-PB406) exhibit additional diffraction features at 23.0°, 24.3°, and 31.0°, which are absent or less pronounced in the biochar samples. These peaks are characteristic of bentonite clay minerals, particularly layered aluminosilicates such as montmorillonite (Fosso-Kankeu E; Waanders F B, 2019; Shakir; Al-Yaqoobi, 2025). The emergence and increased intensity of these reflections confirm the successful incorporation of the clay phase into the carbon matrix. Furthermore, the sharper and more defined peaks observed in the composites, compared to the biochar samples, indicate a higher degree of crystallinity due to the presence of the mineral component (Fosso-Kankeu E; Waanders F B, 2019; Zhao, F. *et al.*, 2023).

Given this, the XRD patterns obtained in this study are consistent with previous reports on lignocellulosic biochars and biochar–clay composites. Studies have shown, ZHAO, F. et al., 2023, that ball milling can reduce crystallite size, increase defect density, and promote better interaction between carbon and mineral phases. In biochar–bentonite composites, these effects are often associated with improved dispersion of clay particles, enhanced surface heterogeneity, and the creation of additional adsorption sites. This hybrid structure is advantageous for adsorption processes, as it provides multiple interaction mechanisms, including electrostatic attraction, π–π interactions, and ion exchange.

5.10 FTIR - Selected Samples

The FTIR spectra of the selected samples — PB, PB202, PB406, B-PB206, and B-PB406 — are presented in Graphic 12, enabling a comparative evaluation of the surface functional groups as a function of milling conditions and the incorporation of bentonite. The highlighted bands provide a consistent basis for interpreting the structural and chemical modifications across the biochar and composite materials.

Graphic 12 - FTIR spectra of the selected samples (PB, PB202, PB406, B-PB206 and B-PB406).

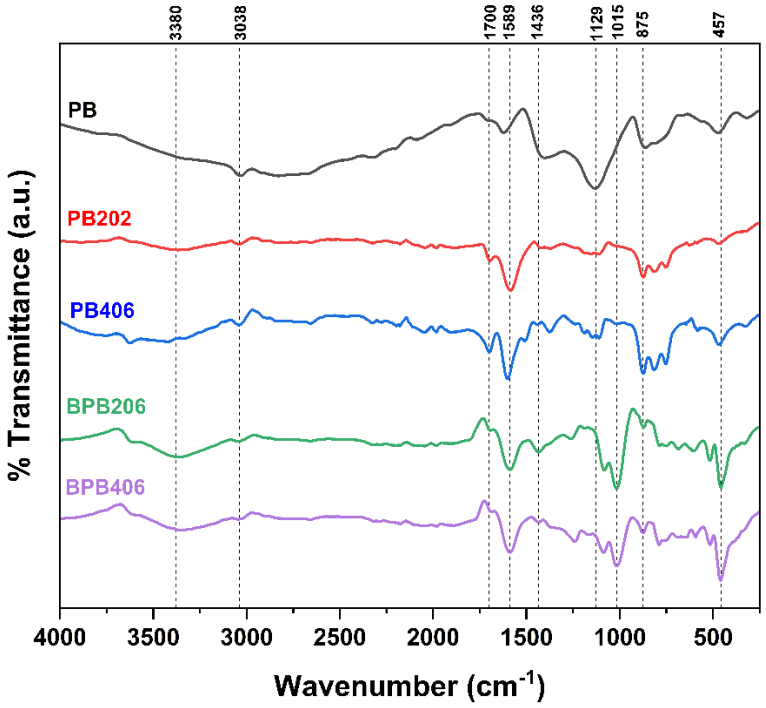

Source: Autor.

Upon high-energy ball milling, noticeable modifications are observed in PB202 and PB406. Although the main functional groups are preserved, subtle changes in band intensity and definition can be identified, particularly in the regions associated with C=O stretching of carbonyl or carboxylic groups (1700 cm^{-1}) and C=C vibrations in aromatic rings (1589 cm^{-1}). According to Fosso-kankeu e Waanders F.B., 2019, these variations suggest that mechanical activation promotes surface restructuring, possibly exposing new active sites and altering the distribution of functional groups. The increased definition of bands in PB406, in particular, may indicate a higher degree of surface heterogeneity and defect formation, which has been associated in the literature with enhanced adsorption performance due to the creation of more accessible binding sites (Shakir; Al-Yaqoobi, 2025; Sudhakaran; Rajan; Ravindranath, 2022).

The incorporation of bentonite in B-PB206 and B-PB406 introduces more pronounced spectral changes throughout the entire spectral zone. The intensification of bands around 1015−1129 cm^{-1} is characteristic of Si−O stretching vibrations from the aluminosilicate framework of bentonite, confirming the successful integration of the clay phase into the composite (Sudhakaran; Rajan; Ravindranath, 2022; Zhao, F. *et al.*, 2023). Additionally, the band near 457 cm^{-1} becomes more prominent, corresponding to Si−O−Al and Si−O−Si bending modes, which are typical of layered silicate minerals. In agreement with Zhao, F. et al., 2023, the persistence of bands related to aromatic carbon (~1589 cm^{-1}), along with these mineral

characteristics present in bentonite clay, demonstrates the coexistence of organic and inorganic domains, a striking characteristic of biochar and clay composites.

By comparing B-PB206 and B-PB406, there are small differences in the intensity and sharpness of the bands, however, this indicates that the grinding conditions influence not only the dispersion of bentonite in the carbon matrix, but also the accessibility of the functional groups. The more pronounced mineral-related bands in B-PB406 suggest improved exfoliation or dispersion of the clay phase at higher milling intensity, which can enhance the availability of adsorption sites. This observation is consistent with studies reporting that mechanical activation improves interfacial contact between biochar and clay, leading to synergistic effects in adsorption performance (Fosso-Kankeu E; Waanders F B, 2019; Shakir; Al-Yaqoobi, 2025).

Thus, the FTIR results are consistent with literature reports on biochar–bentonite composites, where the combination of aromatic carbon domains and the layered aluminosilicate structure of bentonite enhance surface functionality and adsorption capacity. The presence of Si−O groups contributes to cation exchange capacity, while the carbon matrix provides π–π interaction sites for aromatic pollutants such as methylene blue, resulting in a synergistic adsorption behavior superior to that of pristine biochar or clay. Overall, FTIR confirms that high-energy ball milling process increases surface heterogeneity and functional group accessibility, while bentonite incorporation introduces additional inorganic functionalities, jointly improving the adsorption performance through complementary carbon–mineral interactions.

5.11 SEM/EDS - Selected Samples

Figure 12 presents the SEM micrographs of the selected samples after the preliminary screening, highlighting the morphological characteristics of the biochar (PB202 and PB406) and the clay–biochar composite (B-PB206 and B-PB406). The images were acquired at different magnifications, allowing the evaluation of both surface texture and the distribution of mineral phases associated with the materials.

Figure 12 - SEM micrographs of the selected samples: (a) PB202 at 1200x magnification, (b) PB406 at 2500x magnification, (c) B-PB206 at 1500x magnification and (d) B-PB406 at 1500x magnification.

(a) (b)

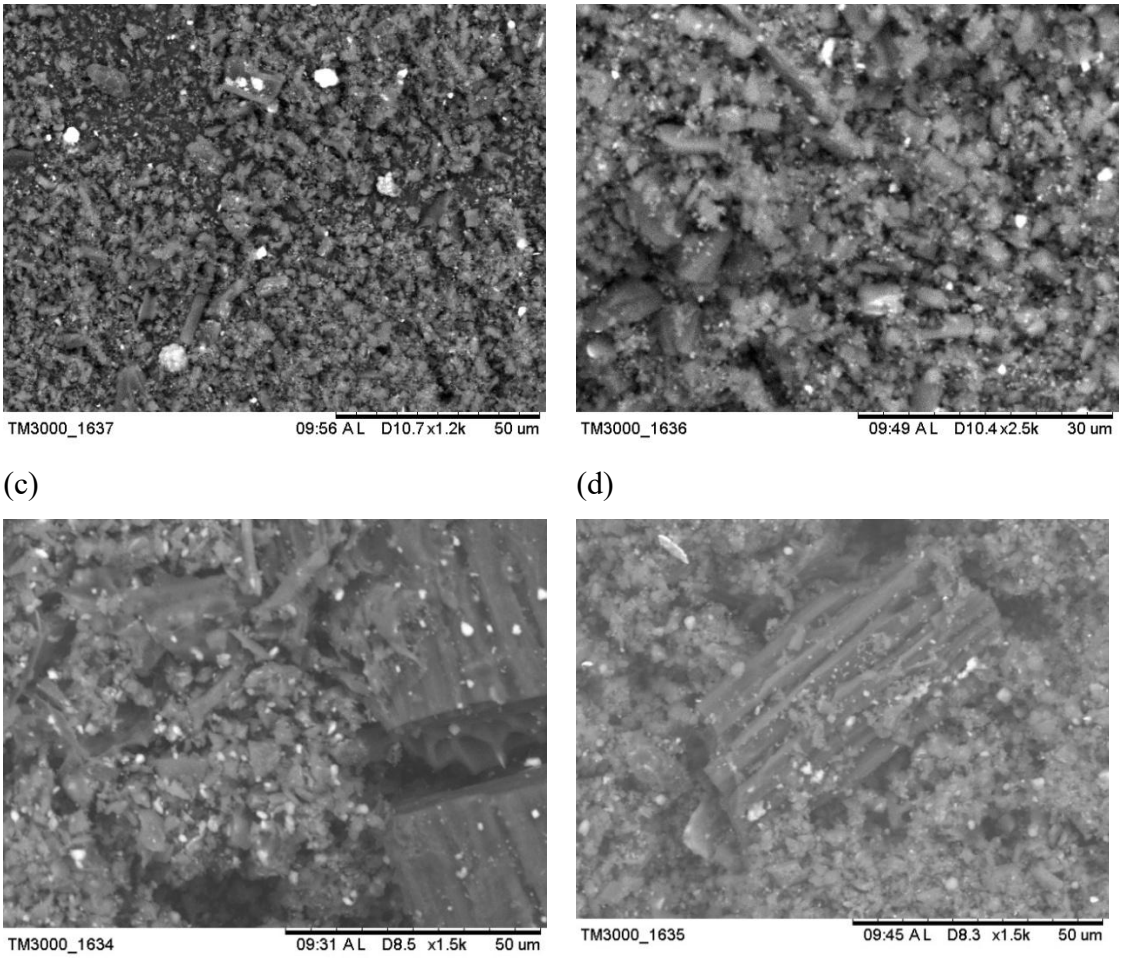

Source: Autor.

Firstly, it can be observed that the biochar samples PB202 and PB406, Figures 12 (a–b), exhibit a predominantly irregular morphology, composed of carbonaceous fragments with relatively rough surfaces and a limited presence of adhered particles. The lower amount of mineral agglomerates suggests a composition that is predominantly organic, with a reduced contribution from surface mineral phases (Yao *et al.*, 2014; Zhao, F. *et al.*, 2023). Furthermore, a markedly disintegrated morphological structure is evident when compared to the original biomass, characterized by compact regions interspersed with heterogeneous porosity, which is typical of lignocellulosic biochars produced via pyrolysis. Moreover, high-energy milling at greater intensity (PB406) promoted a slight reduction in particle size and an increase in structural fragmentation, which tends to enhance the exposure of active sites and increase the surface area available for adsorption (Yang *et al.*, 2020).

In contrast, the composite samples B-PB206 and B-PB406, Figures 12 (c–d), exhibit a more heterogeneous surface densely covered with mineral particles, as evidenced by the significant increase in mineral agglomerates. These agglomerates are associated with the incorporation of bentonitic clay into the carbonaceous matrix, resulting in a hybrid structure in which lamellar

clay particles coexist with the biochar (Lopez-Tenllado; Motta; Hill, 2021; Wang *et al.*, 2023). Additionally, the presence of more defined lamellar structures — particularly evident in sample B-PB406 — is consistent with the typical morphology of phyllosilicates, indicating that the high-energy milling process promoted effective dispersion of the clay over the biochar surface. This behavior has been reported Yang et al., 2020, where biochar–clay composites exhibit greater structural heterogeneity and an increased density of active sites due to the synergistic interaction between organic and mineral phases.

Based on the EDS analysis, Table 11, these morphological observations can be confirmed. The biochar samples (PB202 and PB406) exhibit higher concentrations of elements associated with the carbonaceous matrix and residual mineral salts, such as K and Cl, along with moderate O contents and low Si levels. In contrast, the composite samples show a significant increase in Si content (18.78 wt% for B-PB206 and 10.02 wt% for B-PB406) and O, evidencing the incorporation of the silicate phase from bentonite. This compositional shift reinforces the presence of aluminosilicates within the structure and indicates a substantial modification of the material's surface chemistry. Furthermore, the relative decrease in K and Cl in the composites suggests a dilution of the original mineral phase of the biochar due to the addition of clay.

Table 11 - EDS for PB202, PB406, B-PB206 and B-PB406.

Sample	**Si (%wt)**	**K (%wt)**	**Cl (%wt)**	**Ca (%wt)**	**S (%wt)**	**Mg (%wt)**	**Na (%wt)**
PB 202	5.73	27.12	22.89	6.75	2.44	5.88	2.76
PB 406	4.36	30.83	23.72	7.98	2.40	5.63	2.45
B-PB 206	18.78	13.47	12.21	4.93	1.50	5.40	2.29
B-PB 406	10.02	24.61	17.63	4.42	2.09	4.34	3.59

Source: Autor.

Thus, the combination of biochar porosity and the high specific surface area of bentonite results in a material with a greater diversity of adsorption sites. While the biochar contributes oxygenated functional groups and a porous structure, the clay provides negatively charged surfaces and ion-exchange sites, favoring the adsorption of cationic dyes such as methylene blue. This synergistic effect has been widely reported in studies involving biochar–clay composites, where enhanced adsorption capacity is attributed to the combination of physical mechanisms and chemical interactions. Furthermore, high-energy ball milling plays a crucial role in the structural modification of these materials, promoting particle size reduction,

increased surface area, and improved dispersion of the clay phase within the carbonaceous matrix, thereby enhancing the accessibility of active sites.

5.12 Thermal Analysis - Selected Samples

Graphic 13 presents the thermogravimetric (TG), derivative thermogravimetric (DTG), and differential scanning calorimetry (DSC) curves for the selected samples, highlighting the thermal behavior of biochar and biochar–bentonite composites produced under different high-energy ball milling conditions. The thermal events were divided into three main regions: Region I (25–265°C), Region II (265–625°C), and Region III (625–1000°C), allowing a systematic interpretation of the degradation processes.

Graphic 13 - Thermograms of selected samples (PB202, PB406, B-PB206, and B-PB406): (a) TG curves; (b) DTG curves; and (c) DSC curves.

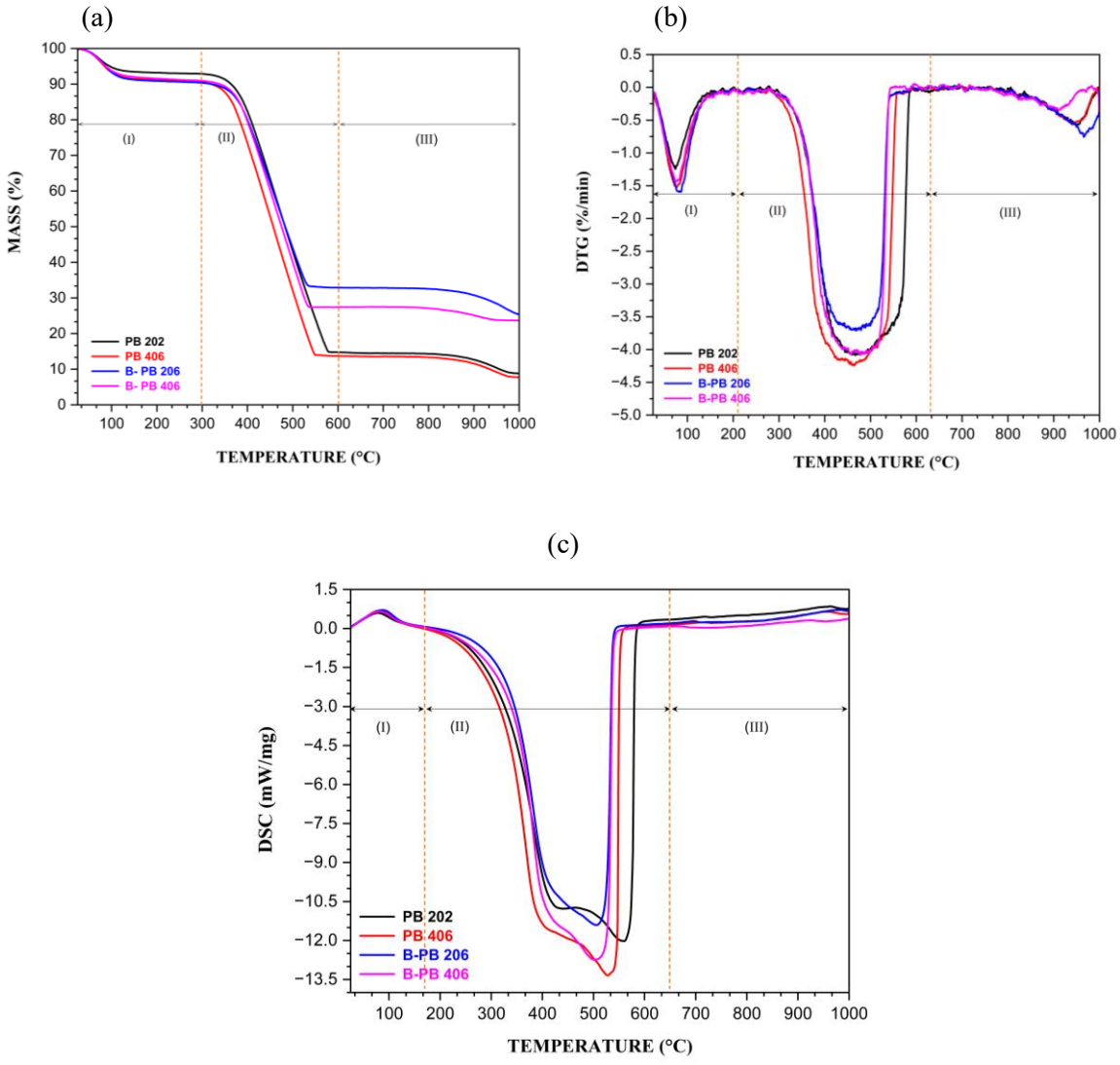

Source: Autor.

The main thermal parameters observed in the thermograms are summarized in Table 12.

Table 12 - Main thermal parameters obtained from TG, DTG, and DSC analyses for the selected samples (PB202, PB406, B-PB206, and B-PB406).

PARAMETERS		SAMPLES			
		PB 202	**PB 406**	**B-PB 206**	**B-PB 406**
Region I	**Δ** [a]	06.72%	08.80%	09.10%	08.24%
	T_{max} [b]	73.5°C	76.3°C	83.28°C	75.6°C
	V_{max} [c]	− 01.24 %/min	− 01.52 %/min	− 01.59 %/min	− 01.43 %/min
	J_{max} [d]	+ 0.59 mW/mg	+ 0.69 mW/mg	+ 0.71 mW/mg	+ 0.65 mW/mg
	A_{max} [e]	+ 90.87 J/g	+ 108.9 J/g	+ 132.7 J/g	+ 107.6 J/g
Region II	**Δ** [a]	78.69%	77.44%	58.06%	64.28%
	T_{max} [b]	466.7°C	464.4°C	479.3°C	494.3°C
	V_{max} [c]	− 04.08 %/min	− 04.24 %/min	− 03.70 %/min	− 04.06 %/min
	J_{max} [d]	− 12.02 mW/mg	− 13.34 mW/mg	− 11.40 mW/mg	− 12.73 mW/mg
	A_{max} [e]	− 15,617 J/g	− 14,722 J/g	− 10,799 J/g	− 12,148 J/g
Region III	**Δ** [a]	05.77%	05.93%	07.46%	03.79%
	J_{max} [d]	+ 0.85 mW/mg	+ 0.64 mW/mg	+ 0.71 mW/mg	+ 0.30 mW/mg
	A_{max} [e]	+ 248.9 J/g	+ 89.66 J/g	+ 961.5 J/g	+ 253.5 J/g

Source: Autor.

In Region I, all samples exhibit relatively low mass losses (≈ 6.7−9.1%), associated with the removal of physically adsorbed moisture and light volatile compounds. This stage is supported by DTG peaks around 73−83 °C and endothermic DSC signals (≈ 0.60 to 0.71 mW/mg), confirming dehydration processes. The slightly higher mass loss observed for B-PB206 (9.10%) suggests an increased hydrophilic character due to the presence of bentonite, which is consistent with the hygroscopic nature of clay minerals and their ability to retain interlayer water (Fosso-Kankeu E; Waanders F B, 2019; Ribeiro Filho *et al.*, 2024).

Region II corresponds to the main thermal degradation stage, where significant mass losses occur due to the decomposition of organic structures. The biochar samples (PB202 and PB406) show higher mass losses (≈ 77−79%) compared to the composites (≈ 58−64%), indicating that the incorporation of bentonite improves thermal stability by reducing the relative organic fraction. The onset temperatures (T_{ONSET} ≈ 292.7−338.8 °C) and DTG peaks (≈ 430−535 °C) are associated with the breakdown of residual hemicellulose, cellulose, and lignin-derived structures, as well as the decomposition of oxygen-containing functional groups. According to Hamzaoui et al., 2015, the presence of two DTG peaks in this region suggests multi-step degradation processes, which are typical of lignocellulosic-derived biochars, it should be noted that exothermic DSC peaks (−10 to −13 mW/mg) further confirm that these processes involve oxidative decomposition and structural rearrangements of the carbon matrix. Notably, PB406 exhibits a slightly higher T_{ONSET} (323.5 °C) compared to PB202 (292.7 °C), indicating that increased milling intensity may promote structural ordering or partial graphitization, enhancing thermal resistance (Chen, M., 2016; Hamzaoui *et al.*, 2015).

In Region III, the mass loss becomes significantly lower (≈ 3.8−7.5%), corresponding to the decomposition of highly stable carbonaceous structures and mineral transformations. The composites exhibit substantially higher residual masses (≈ 23−25%) than the biochar samples (≈ 7−9%), directly reflecting the inorganic contribution of bentonite. DTG peaks near 910−965 °C and weak endothermic DSC signals indicate slow degradation of recalcitrant carbon structures and possible dehydroxylation of clay minerals, in which the higher residual fraction and reduced degradation rate in composites confirm the stabilizing effect of the mineral phase, which acts as a thermal barrier and limits heat transfer and volatile release (Chen, M., 2016; Ram *et al.*, 2014).

Therefore, the observed thermal behavior aligns well with previous studies on lignocellulosic biochars and clay-based composites. Studies on biochar–bentonite composites report similar trends, where the clay phase increases residual mass, shifts degradation temperatures, and reduces overall mass loss due to dilution of the organic fraction and improved structural stability, as observed in this study. Additionally, the presence of bentonite has been associated with enhanced thermal resistance through “physical shielding” and interactions between silicate layers and carbon structures. Therefore, the results obtained for B-PB206 and B-PB406 confirm that the incorporation of bentonite not only modifies adsorption properties but also significantly improves the thermal robustness of the material.

5.13 Adsorption Test - Selected Samples

5.13.1 Biochar Dosage Variation

Graphic 14 presents the effect of adsorbent dosage (2−25 mg) on the removal efficiency (%) of MB for the PB, PB202, PB406, B-PB206 and B-PB406. Overall, all materials exhibit an increase in removal efficiency with increasing dosage, although with different magnitudes and trends depending on composition and milling conditions.

Graphic 14 - Effect of adsorbent dosage (2, 5, 10, 15, 20 and 25 mg) on the removal efficiency (%) of methylene blue for PB, PB202, PB406, B-PB206 and B-PB406.

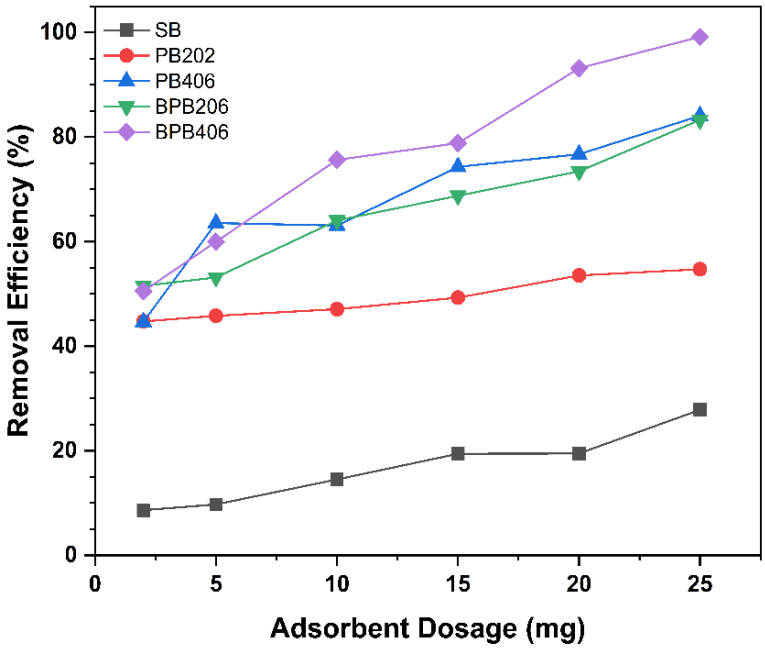

Source: Autor.

Initially, PB exhibits the lowest adsorption performance across the entire dosage range, with removal efficiencies increasing modestly from 8.66% (2 mg) to 27.83% (25 mg). This behavior reflects the limited availability of active sites and the relatively less developed porosity of the non-milled material. In contrast, the ball milled biochars (PB202 and PB406) demonstrate a clear improvement in adsorption performance, confirming the positive impact of high-energy milling, as can be seen with PB202 which shows a gradual increase from 44.74% to 54.72%, while PB406 exhibits a more pronounced improvement, rising from 44.66% to 84.07%. This superior performance of PB406 is attributed to the higher milling intensity, which promotes pore development, particle size reduction, and exposure of active sites, as widely reported for mechanically activated biochars (Kovalchuk *et al.*, 2023; Mohan *et al.*, 2014).

A more significant improvement is observed for the composite materials, particularly B-PB206 and B-PB406. The B-PB206 sample shows a steady increase in removal efficiency from 51.55% to 83.27%, outperforming PB202 and approaching PB406 at higher dosages. However,

the most remarkable behavior is observed for B-PB406, which reaches near-complete removal (99.17%) at 25 mg. This trend highlights the synergistic effect between the biochar matrix and bentonite clay, where the combination of porous carbon structure and negatively charged aluminosilicate layers enhances the adsorption of cationic dyes such as methylene blue (Ângelo Silva, 2017; Leonel et al., 2014).

From this perspective, the increase in removal efficiency with adsorbent dosage is primarily associated with the greater availability of adsorption sites and surface area. At lower dosages, it is noted the number of active sites is insufficient to capture all dye molecules in solution, leading to lower efficiencies. As the dosage increases, more adsorption sites become available, resulting in higher removal percentages, however, it is important to note that at higher dosages, the increase in removal efficiency tends to become less pronounced (e.g., PB202), indicating a possible approach to saturation conditions or particle aggregation, which can reduce the effective surface area. This effect is particularly evident in composite systems, as reported by Lopez-Tenllado; Motta; Hill, 2021, where bentonite contributes additional active sites through ion-exchange and electrostatic interactions, while biochar provides a porous structure that facilitates mass transfer.

5.13.2 Contact Time Variation

Graphic 15 (a–d) presents the adsorption kinetics of MB onto the selected materials — PB202, PB406, B-PB206 and B-PB406 — expressed as adsorption capacity (q_t) as a function of contact time (5−240 min), along with the fitted kinetic models (PFO, PSO, Elovich and Weber–Morris). Overall, all samples exhibit a rapid initial adsorption stage followed by a gradual approach to equilibrium, with distinct kinetic behaviors depending on milling intensity and the presence of bentonite.

Graphic 15 - Adsorption kinetics of MB expressed as adsorption capacity (qt) and function of contact time (5, 15, 30, 60, 120, 180 and 240 min). (a) PB202, (b) PB406, (c) B-PB206 and (d) B-PB406.

(a) (b)

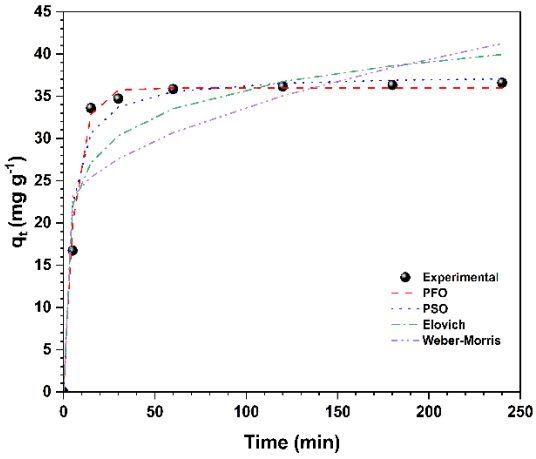

(c)

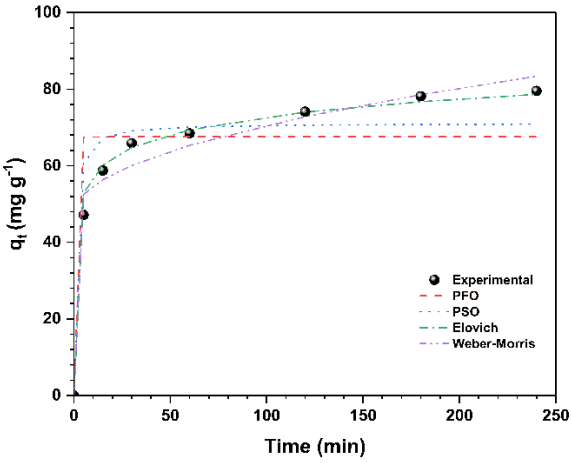

(d)

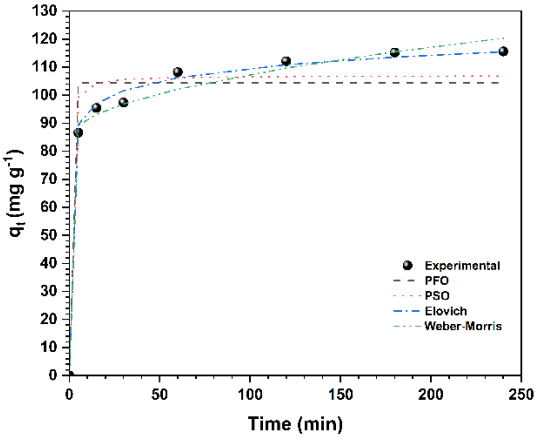

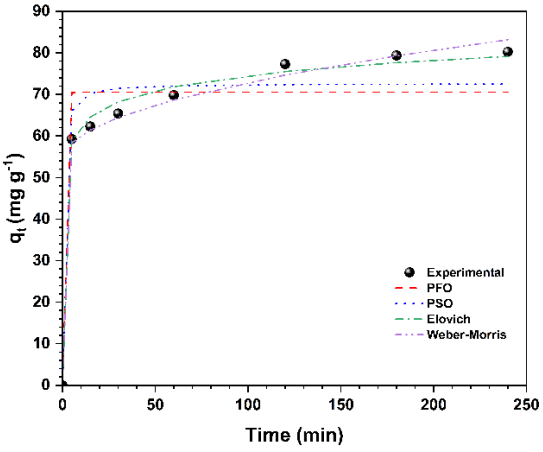

Source: Autor.

The kinetic parameters summarized in Table 13 provide further insight into the adsorption mechanism.

Table 13 - Adsorption kinetic parameters of MB on selected samples (PB202, PB406, B-PB206 and B-PB406).

MODEL TYPE	PARAMETER	PB 202	PB 406	B-PB 206	B-PB 406
Experimental	q_e (mg/g)	36.6	79.53	115.62	80.24
Pseudo-First Order (PFO)	q_e (mg/g)	35.99	67.6	104.41	70.56
	k_1 (h^{-1})	0.162	1.114	1.554	1.345
	R^2	0.89	0.33	0.35	0.39
Pseudo-Second Order (PSO)	q_e (mg/g)	37.59	71.12	107.01	72.65
	k_2 (g/mg·h)	0.00774	0.0161	0.024	0.0276
	h (mg/g·h)	10.94	81.28	274.6	145.8

	R^2	0.90	0.59	0.56	0.58
Elovich	α (mg/g·h)	108.3	$3.7 \cdot 10^3$	$8.6 \cdot 10^5$	$7.4 \cdot 10^4$
	β (g/mg)	0.21	0.15	0.14	0.19
	R^2	0.82	0.94	0.95	0.95
Intraparticle Diffusion (Weber–Morris)	K_p (mg/g·$h^{1/2}$)	1.36	2.32	2.34	1.87
	C (mg/g)	20.12	47.33	84.02	54.17
	R^2	0.56	0.91	0.92	0.95

Source: Autor.

For PB202, adsorption increases sharply within the first 15 min (16.74 → 33.60 mg·g^{-1}), followed by a slow progression toward equilibrium ($q_e \approx 36.6$ mg·g^{-1}). The modest increase after 30 min indicates limited availability of active sites and slower diffusion into internal pores. Kinetic modeling shows relatively similar fits for PFO ($R^2 = 0.89$) and PSO ($R^2 = 0.90$), suggesting that both physisorption and chemisorption mechanisms may contribute. However, the low R^2 for the Weber–Morris model (0.56) indicates that intraparticle diffusion is not the sole rate-controlling step.

In contrast, PB406 exhibits significantly enhanced kinetics and capacity, reaching ($q_e \approx$ 79.53 mg·g^{-1}). The adsorption process remains rapid in the early stage but continues to increase more substantially over time compared to PB202. Notably, the Elovich model provides the best fit ($R^2 = 0.95$), indicating a heterogeneous adsorption surface and chemisorption-dominated behavior. The relatively high R^2 values for the Weber–Morris model (0.91) further suggests that intraparticle diffusion plays a relevant role, although the non-zero intercept (C = 47.33 mg·g^{-1}) confirms that boundary layer effects are also significant. These results are consistent with the effects of high-energy ball milling, which enhances surface heterogeneity, defect density, and active site availability (Ahmad *et al.*, 2020; Gouamid; Ouahrani; Bensaci, 2013).

The composite B-PB206 demonstrates the highest adsorption capacity among all samples ($q_e \approx 115.62$ mg·g^{-1}), with very rapid uptake (≈ 86.64 mg·g^{-1} at 5 min), indicating a strong affinity between the adsorbent and methylene blue. Similar to PB406, the Elovich model provides the best fit ($R^2 = 0.96$), reinforcing the presence of a heterogeneous surface and chemisorption mechanisms. Additionally, the high α value ($8.6 \cdot 10^5$ mg·g^{-1} h^{-1}) reflects a very fast initial adsorption rate. The Weber–Morris model ($R^2 = 0.92$) suggests that intraparticle diffusion contributes significantly to the adsorption process, although it is not the only controlling step. The superior performance of B-PB206 can be attributed to the synergistic

interaction between the porous carbon matrix and the layered structure of bentonite, which provides additional adsorption sites through electrostatic attraction and ion exchange (Chen, S. *et al.*, 2022; Fosso-Kankeu E; Waanders F B, 2019).

For B-PB406, the adsorption capacity ($q_e \approx 80.24$ mg·g^{-1}) is lower than that of B-PB206, but still higher than PB202. The adsorption process follows a similar trend, with rapid initial uptake and gradual stabilization. The Elovich ($R^2 = 0.95$) and Weber–Morris ($R^2 = 0.96$) models both show excellent fits, indicating that adsorption occurs on a heterogeneous surface with significant contribution from intraparticle diffusion. However, the lower capacity compared to B-PB206 suggests that excessive milling may partially disrupt the lamellar structure of bentonite or promote particle agglomeration, reducing the accessibility of active sites.

Therefore, the adsorption process for all materials can be divided into three stages: (Subratti *et al.*, 2021; Yang *et al.*, 2020; Zhao, F. *et al.*, 2023)

(I) Rapid external surface adsorption driven by concentration gradients,
(II) Gradual intraparticle diffusion into pores, and
(III) Equilibrium stage where adsorption sites become saturated.

The better performance of the Elovich model for most samples highlights the importance of surface heterogeneity and chemisorption interactions, particularly for composite materials. This behavior has been widely reported for biochar–clay systems, where the combination of porous carbon structures and aluminosilicate layers enhances adsorption through multiple mechanisms, including π–π interactions, electrostatic attraction, and ion exchange (Abollino *et al.*, 2003; Wang *et al.*, 2023).

5.13.3 MB Concentration Variation

The adsorption curves obtained for the selected materials are presented as plots of equilibrium adsorption capacity (q_e) versus equilibrium concentration (C_e), Graphic 16 (a-d), together with the nonlinear fittings of the Langmuir and Freundlich models. These curves provide a comprehensive evaluation of how MB molecules interact with the surface of petiole–derived biochar and biochar–bentonite composites, allowing the identification of adsorption capacity, surface heterogeneity, and affinity.

Graphic 16 - Adsorption isotherms of MB onto selected samples. (a) PB202, (b) PB406, (c) B-PB206 and (d) B-PB406).

(a) (b)

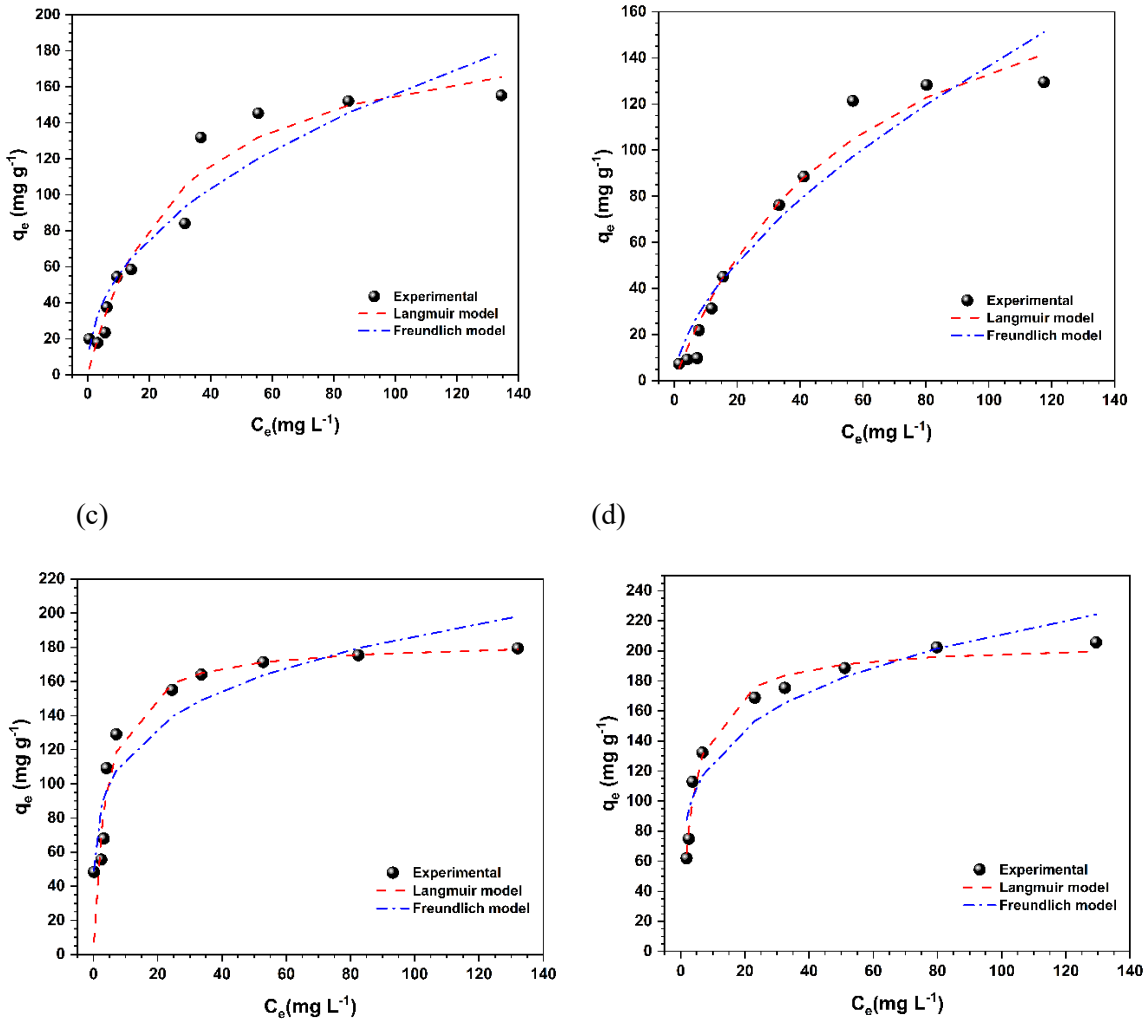

(c) (d)

Source: Autor.

The isotherm parameters summarized in Table 14 provide further insight into the adsorption process.

Table 14 - Parameters obtained from fitting the isotherm models to the methylene blue adsorption data.

MODEL TYPE	PARAMETER	PB 202	PB 406	B-PB 206	B-PB 406
Langmuir	q_m (mg/g)	201.03	178.89	184.1	205.53
	K_L (L/mg)	0.034	0.098	0.25	0.25
	R^2 (a)	0.95	0.91	0.89	0.98
	R_L (b)	0.162–0.921	0.063–0.802	0.025–0.609	0.025–0.608
Freundlich	K_F (c)	19.62	44.16	71.58	76.79
	n (d)	2.22	3.43	4.8	4.54
	R^2 (a)	0.90	0.94	0.87	0.91

[a] Coefficient of determination (dimensionless)
[b] Langmuir separation factor (dimensionless)
[c] Freundlich constant [(mg/g)·(L/mg)$^{1/n}$]
[d] Heterogeneity factor (dimensionless)

Source: Autor.

Graphic 16 (a–b), PB202 and PB406, exhibited a progressive increase in adsorption capacity with increasing MB concentration, indicating the gradual occupation of available active sites. PB202 reached a maximum q_e of 155.25 mg·g^{-1}. with a Langmuir maximum capacity (Q_m) of 201.03 mg·g^{-1} and a relatively good fit (R^2 = 0.95), suggesting monolayer adsorption on a homogeneous surface. However. Freundlich model (R^2 = 0.90; n = 2.22) also adequately described the data. indicating a certain degree of surface heterogeneity. In contrast, PB406 showed a slightly lower maximum experimental capacity (129.45 mg·g^{-1}) and Q_m of 178.89 mg·g^{-1}, but a higher Freundlich constant (K_F = 44.16) and heterogeneity factor (n = 3.43). suggesting stronger adsorption intensity and more energetically favorable sites.

The composite materials B-PB206 and B-PB406, Graphic 16 (c–d), exhibited significantly higher adsorption capacities compared to the pristine biochars. confirming the synergistic effect between the carbonaceous matrix and bentonite clay. B-PB206 reached a maximum q_e of 179.44 mg·g^{-1} with Q_m = 184.1 mg·g^{-1}, while B-PB406 achieved the highest adsorption performance among all samples with q_e = 205.67 mg·g^{-1} and Q_m = 205.53 mg·g^{-1}. Notably, B-PB406 showed an excellent fit to the Langmuir model (R^2 = 0.98) indicating predominance of monolayer adsorption, whereas the Freundlich parameters (K_F = 76.79; n = 4.54) further confirmed high adsorption affinity and strong surface heterogeneity. The elevated K_L values (0.255−0.258 L·mg^{-1}) and favorable R_L range (0.025−0.608) for both composites indicate highly favorable adsorption processes across the studied concentration range.

The improved performance of the composites can be attributed to the incorporation of bentonite, which introduces additional adsorption mechanisms such as cation exchange, electrostatic attraction and surface complexation, alongside the π–π interactions and pore-filling mechanisms typical of biochar. The presence of aluminosilicate structures enhances surface polarity and increases the density of active sites, resulting in higher adsorption capacities and stronger affinity toward methylene blue molecules (Leal *et al.*, 2012; Silva; Lima, 2017). Consequently, the isotherm analysis indicates that although both Langmuir and Freundlich models adequately describe the adsorption process, their predominance depends on the material, that is, biochars exhibit a mixed behavior with moderate surface heterogeneity,

whereas the composites — particularly B-PB406 — show higher adsorption capacity, stronger affinity and a tendency toward monolayer adsorption.

6 CONCLUSION

The petiole of *Copernicia prunifera* was successfully employed as a precursor to produce biochar by slow carbonization and for the preparation of biochar–bentonite composites modified by high-energy ball milling, which were effectively applied as bioadsorbents for the removal of methylene blue from aqueous media. Biochar was successfully synthesized from the carnauba petiole, and biochar–bentonite composites were prepared under different milling conditions, enabling the systematic evaluation of the effects of milling time and rotational speed on the properties of the resulting materials.

The carbonization of carnauba petiole at 550 °C promoted profound compositional and structural transformations, converting lignocellulosic biomass into a biochar with properties highly favorable for methylene blue adsorption. Proximate and elemental analyses evidenced a significant reduction in volatile matter and marked increases in fixed carbon and ash content, alongside a strong enrichment in carbon and a decrease in H/C and O/C ratios. These changes indicate the development of a more aromatic, chemically stable structure, enriched with mineral phases, which are known to contribute to adsorption processes.

Multitechnique characterization (XRD, FTIR, SEM/EDS, and thermal analyses) confirmed that carbonization led to the degradation of the original lignocellulosic domains, yielding a disordered carbonaceous matrix embedded with crystalline mineral phases such as silica and carbonates. The resulting biochar exhibited a heterogeneous surface combining aromatic domains, residual oxygen-containing functional groups, and mineral active sites. In this way, this multifunctional nature enabled the coexistence of multiple adsorption mechanisms, including π–π interactions, electrostatic attraction, ion exchange, and surface complexation, which collectively enhanced adsorption performance beyond what would be expected solely from surface area considerations.

Regarding batch adsorption experiments, it was concluded that the adsorption process is strongly influenced by the adsorbent dosage, contact time, and initial dye concentration, although the adsorption capacity decreased with increasing dosage due to site saturation effects, the removal efficiency increased and stabilized at higher dosages. Kinetic studies revealed an initial stage of rapid adsorption, followed by a slower phase governed by intraparticle diffusion, in which the process was best described by PSO and Elovich models, indicating chemisorption on a heterogeneous surface. Furthermore, the equilibrium data were well fitted by the Langmuir model, with a high theoretical maximum adsorption capacity ($q_m \approx 210.66$ mg g^{-1}), although the Freundlich parameters confirmed the heterogeneity of the surface.

Through the analysis of the results, the application of high-energy ball milling and the incorporation of bentonite played a crucial role in modulating adsorption performance. For biochar, increasing milling energy enhanced adsorption capacity (up to 72.39 mg g^{-1} for PB406), due to particle size reduction, defect generation, and increased exposure of active sites. In contrast, biochar–bentonite composites exhibited superior adsorption performance even without milling, highlighting the synergistic interaction between the porous carbon matrix and the aluminosilicate layers. Intermediate milling energies improved clay dispersion and preserved structural integrity, whereas excessive milling led to aggregation and partial loss of adsorption efficiency. Under optimized conditions, the composite B-PB406 achieved near-complete removal efficiency (99.17%) and the highest experimental adsorption capacity (205.67 mg g^{-1}), with excellent agreement with the Langmuir model, indicating favorable monolayer adsorption.

Comparative analyses of the selected samples demonstrated that high-energy ball milling promoted increased structural disorder and surface heterogeneity, while bentonite incorporation introduced additional cation exchange sites and enhanced thermal stability, resulting in composites with significantly higher initial adsorption rates than pristine biochar due to improved accessibility of active sites and the combined contribution of surface reactions and intraparticle diffusion mechanisms. Overall, these findings confirm that biochar derived from carnauba petiole, especially when modified through mechanical activation and combined with bentonite, constitutes a efficient and sustainable adsorbent for methylene blue removal, as the integration of pyrolysis, ball milling, and mineral modification effectively tailors physicochemical properties and maximizes adsorption performance through synergistic effects. Consequently, this approach supports the valorization of regional agro-industrial residues and the development of multifunctional adsorbent materials with competitive relative to activated carbons, while also highlighting the need for future studies focused on regeneration, continuous-flow applications, and the removal of a broader spectrum of contaminants.

7 FUTURE PERSPECTIVES

Although this study provides a comprehensive evaluation of biochar and biochar–bentonite composites produced from carnauba petiole, as well as the influence of high-energy ball milling assessed via response surface methodology (RSM), some aspects remain to be further explored in order to deepen the understanding of the adsorption system. The results clearly demonstrated that both milling intensity and clay incorporation play a key role in tuning adsorption performance; however, additional investigations are necessary to refine the mechanistic interpretation and expand the applicability of the materials.

A key point for future research is the characterization of surface charge properties. The determination of the point of zero charge (Ph_{pzc}), combined with zeta potential measurements, would provide valuable information regarding the electrostatic behavior of the adsorbents under different pH conditions. Such analyses are essential to clarify the contribution of electrostatic interactions in the adsorption of methylene blue and to better correlate surface chemistry with adsorption efficiency.

Furthermore, while FTIR analyses were conducted for the initial materials, post-adsorption FTIR studies were not performed. Incorporating this analysis in future work would enable the identification of changes in functional groups after adsorption, offering direct evidence of the interaction mechanisms involved, such as π–π interactions, ion exchange, electrostatic attraction, and surface complexation.

In addition, thermodynamic parameters were not addressed in the present study. Future investigations should include the determination of Gibbs free energy, enthalpy, and entropy changes, which would allow the assessment of the spontaneity and energetic nature of the adsorption process, complementing the kinetic and equilibrium analyses.

Lastly, it is recommended that future work investigates the behavior of these materials in more complex environments, including real effluents and systems containing contaminants. Evaluating the potential influence of inorganic residues introduced during the milling process is also important to ensure consistent performance. Altogether, these efforts will contribute to consolidating the practical viability of carnauba petiole-derived biochar and its bentonite-based composites as efficient and sustainable adsorbents for environmental remediation.

REFERENCES

ABOLLINO, O.; ACETO, M.; MALANDRINO, M.; SARZANINI, C.; MENTASTI, E. Adsorption of heavy metals on Na-montmorillonite. Effect of pH and organic substances. *Water Research*, v. 37, n. 7, p. 1619–1627, abr. 2003. Disponível em: https://www.sciencedirect.com/science/article/abs/pii/S0043135402005249. Acesso em: 15 jun. 2026.

AHMAD, A.; KHAN, N.; GIRI, B. S.; CHOWDHARY, P.; CHATURVEDI, P. Removal of methylene blue dye using rice husk, cow dung and sludge biochar: Characterization, application, and kinetic studies. *Bioresource Technology*, v. 306, art. 123202, 1 jun. 2020. Disponível em: https://doi.org/10.1016/j.biortech.2020.123202. Acesso em: 15 jun. 2026.

ALVES, M. O.; COÊLHO, J. D. Extrativismo da Carnaúba: Relações de Produção, Tecnologia e Mercado. 1. ed. Fortaleza: Banco do Nordeste do Brasil, 2008. v. 20. Disponívelem:https://www.bnb.gov.br/s482dspace/bitstream/123456789/784/1/2008_ART_Alves.pdf. Acesso em: 8 ago. 2025.

SILVA, L. A. Â. Avaliação da capacidade adsortiva de carvão ativado e bentonita para a remoção de micropoluentes. 2017. Trabalho de Conclusão de Curso (Graduação em Engenharia Ambiental) – *Universidade Tecnológica Federal do Paraná*, Londrina, 2017. Disponível em: http://repositorio.utfpr.edu.br/jspui/handle/1/3129. Acesso em: 15 jun. 2026.

ANOOP, P. P.; PALANISAMY, T. Coconut shell biochar–Bacillus cereus DKBovi-5 based biocomposite as a sustainable additive for cement mortar: Effect of pyrolysis temperature on characterization, strength, hydration, and healing. *Sustainable Chemistry and Pharmacy*, v. 46, art. 102112, ago. 2025. Disponível em: https://doi.org/10.1016/j.scp.2025.102112. Acesso em: 15 jun. 2026.

ARAÚJO, E. G.; LEAL NETO, R. M.; PILLIS, M. F.; FILHO, F. A. High energy ball mill processing. *Materials Science* Forum, v. 416–418, p. 128–133, 2003. Disponível em: https://doi.org/10.4028/www.scientific.net/MSF.416-418.128. Acesso em: 15 jun. 2026.

ARIF, M.; LIU, G.; YOUSAF, B.; AHMED, R.; IRSHAD, S.; ASHRAF, A.; ZIA-UR-REHMAN, M.; RASHID, M. S. Synthesis, characteristics and mechanistic insight into the clays and clay minerals-biochar surface interactions for contaminants removal: A review. *Journal of Cleaner Production*, v. 310, art. 127548, 10 ago. 2021. Disponível em: https://doi.org/10.1016/j.jclepro.2021.127548. Acesso em: 15 jun. 2026.

AVOM, J.; MBADCAM, J. K.; NOUBACTEP, C.; GERMAIN, P. Adsorption of methylene blue from an aqueous solution on to activated carbons from palm-tree cobs. *Carbon*, v. 35, n. 3, p. 365–369, 1997. Disponível em: https://linkinghub.elsevier.com/retrieve/pii/S0008622396001583. Acesso em: 15 jun. 2026.

BALÁŽ, P. Mechanochemistry in Minerals Engineering. In: BALÁŽ, P. Mechanochemistry in Nanoscience and Minerals Engineering. Berlin; Heidelberg: *Springer*, 2008. p. 257–296. Disponível em: http://link.springer.com/10.1007/978-3-540-74855-7_5. Acesso em: 15 jun. 2026.

BERGAYA, F.; LAGALY, G. Chapter 1: General Introduction: Clays, Clay Minerals, and Clay Science. In: BERGAYA, F.; THENG, B. K. G.; LAGALY, G. (ed.). *Handbook of Clay Science. Amsterdam: Elsevier*, 2006. p. 1–18. Disponível em: https://linkinghub.elsevier.com/retrieve/pii/S1572435205010019. Acesso em: 15 jun. 2026.

BIZERRA, D.; NUNES, J.; BARROS, C.; PAIXÃO, R.; MARQUES, R.; NETO, F. S.; SANTOS, J.; MELO, R.; FERNANDES, B.; RIOS, M. Carnauba Straw as Feedstock for Solid Biofuel Production. *Advances in Environmental and Engineering Research*, v. 4, n. 3, p. 1–13, 2023. Disponível em: https://doi.org/10.21926/aeer.2303043. Acesso em: 15 jun. 2026.

BRIDGWATER, A. V. Biomass for energy. *Journal of the Science of Food and Agriculture*, v. 86, n. 12, p. 1755–1768, 2006. Disponível em: https://doi.org/10.1002/jsfa.2605. Acesso em: 15 jun. 2026.

CAO, X.; HARRIS, W. Properties of dairy-manure-derived biochar pertinent to its potential use in remediation. *Bioresource Technology*, v. 101, n. 14, p. 5222–5228, jul. 2010. Disponível em: https://doi.org/10.1016/j.biortech.2010.02.052. Acesso em: 15 jun. 2026.

CARVALHO, E. dos S. Síntese e caracterização de Al-MCM-41 a partir de caulim por rota hidrotérmica e avaliação de desempenho na adsorção de azul de metileno. 2015. Dissertação (Mestrado em Engenharia Química) – *Universidade Federal do Ceará*, Fortaleza, 2015. Disponível em: http://repositorio.ufc.br/handle/riufc/16931. Acesso em: 15 jun. 2026.

CARVALHO, J. D. S. Análise imediata e avaliação do poder calorífico superior da biomassa de carnaúba com diferentes aglutinantes para uso em forno industrial. 2022. Trabalho de Conclusão de Curso (Graduação em Engenharia Metalúrgica) – *Universidade Federal do Ceará*, Fortaleza, 2022. Disponível em: http://repositorio.ufc.br/handle/riufc/64629. Acesso em: 15 jun. 2026.

CHANG, J. H.; SIVASUBRAMANIAN, P. D.; DONG, C. D.; KUMAR, M. Study on adsorption of ammonium and nitrate in wastewater by modified biochar. *Bioresource Technology Reports*, v. 21, art. 101346, fev. 2023. Disponível em: https://doi.org/10.1016/j.biteb.2023.101346. Acesso em: 15 jun. 2026.

CHEN, M. Thermal Analysis. In: CHUNG, D. D. L. Materials Science and Engineering of Carbon: Fundamentals. *Oxford: Elsevier*, 2016. p. 249–272. Disponível em: https://linkinghub.elsevier.com/retrieve/pii/B978012805256300012X. Acesso em: 15 jun. 2026.

CHEN, S.; ZHANG, B.; HE, X.; SU, Y.; LIU, Q.; XU, H. Research on mechanical-activated nanoscale bentonite and surface aging behavior of its modified asphalt. *Construction and Building Materials*, v. 321, art. 126356, 2022. Disponível em: https://doi.org/10.1016/j.conbuildmat.2022.126356. Acesso em: 15 jun. 2026.

CONTI, R.; FABBRI, D.; VASSURA, I.; FERRONI, L. Comparison of chemical and physical indices of thermal stability of biochars from different biomass by analytical pyrolysis and thermogravimetry. *Journal of Analytical and Applied Pyrolysis*, v. 122, p. 160–168, nov. 2016. Disponível em: https://doi.org/10.1016/j.jaap.2016.10.003. Acesso em: 15 jun. 2026.

DA GAMA, B. M. V.; SILANPÄÄ, M.; SELVASEMBIAN, R.; DE FARIAS SILVA, C. E.; MEILI, L. Effective adsorptive removal of a cationic dye from aqueous solutions using a biosorbent derived from Sargassum sp. *Water Practice and Technology*, v. 19, n. 1, p. 263–280, 2024. Disponível em: https://doi.org/10.2166/wpt.2023.233. Acesso em: 15 jun. 2026.

DE COSTA, P. D.; FURMANSKI, L. M.; DOMINGUINI, L. Production, characterization and application of activated carbon from nutshell for adsorption of methylene blue. *Revista Virtual de Química*, v. 7, n. 4, p. 1272–1285, jul. 2015. Disponível em: https://doi.org/10.5935/1984-6835.20150070. Acesso em: 15 jun. 2026.

DE OLIVEIRA, M. A.; SOUZA, E. S.; CORREIA, D. V.; BARROS, B. S.; BARROS, J. K. Biochar Derived from Sugarcane Bagasse for Adsorption of Anionic and Cationic Dyes. *Materials Research*, v. 28, 2025. Disponível em: https://doi.org/10.1590/1980-5373-MR-2025-0179. Acesso em: 15 jun. 2026.

DEMIRBAŞ, A. Mechanisms of liquefaction and pyrolysis reactions of biomass. *Energy Conversion and Management*, v. 41, n. 6, p. 633–646, 2000. Disponível em: https://linkinghub.elsevier.com/retrieve/pii/S0196890499001302. Acesso em: 15 jun. 2026.

ELNOUR, A. Y.; ALGHYAMAH, A. A.; SHAIKH, H. M.; POULOSE, A. M.; AL-ZAHRANI, S. M.; ANIS, A.; AL-WABEL, M. I. Effect of pyrolysis temperature on biochar microstructural evolution, physicochemical characteristics, and its influence on biochar/polypropylene composites. *Applied Sciences*, v. 9, n. 6, 2019. Disponível em: https://doi.org/10.3390/app9061149. Acesso em: 15 jun. 2026.

AGUIAR, José Euranio de. Remoção de corantes têxteis utilizando adsorventes nanoporosos. 2012. 126 f. Dissertação (Mestrado em Engenharia Química) – Centro de Tecnologia, *Universidade Federal do Ceará*, Fortaleza, 2012. Disponível em: http://repositorio.ufc.br/handle/riufc/5048. Acesso em: 15 jun. 2026.

FERNANDES, J. E.; DANTAS, T. N. D. C.; FONSECA, J. L. C.; PEREIRA, M. R. Carnauba straw: Characterization and chemical treatments. *Journal of Applied Polymer Science*, v. 122,

n. 3, p. 1614–1621, 2011. Disponível em: https://doi.org/10.1002/app.33882. Acesso em: 15 jun. 2026.

FOSSO-KANKEU E; WAANDERS F B. Removal of malachite green and toluidine blue dyes from aqueous solution using a clay-biochar composite of bentonite and sweet sorghum bagasse. *International Journal of Applied Engineering Research*, 2019. 1324–1333 p. Disponível em: http://www.ripublication.com.

FUERTES, A. B.; ARBESTAIN, M. C.; SEVILLA, M.; MACIÁ-AGULLÓ, J. A.; FIOL, S.; LÓPEZ, R.; SMERNIK, R. J.; AITKENHEAD, W. P.; ARCE, F.; MACIAS, F. Chemical and structural properties of carbonaceous products obtained by pyrolysis and hydrothermal carbonisation of corn stover. *Australian Journal of Soil Research*, v. 48, n. 6–7, p. 618–626, 2010. Disponível em: https://doi.org/10.1071/SR10010. Acesso em: 15 jun. 2026.

GOSHADROU, A.; KARIMI, K.; LEFSRUD, M. Characterization of ionic liquid pretreated aspen wood using semi-quantitative methods for ethanol production. *Carbohydrate Polymers*, v. 96, n. 2, p. 440–449, 2013. Disponível em: https://doi.org/10.1016/j.carbpol.2013.04.017. Acesso em: 15 jun. 2026.

GOUAMID, M.; OUAHRANI, M. R.; BENSACI, M. B. Adsorption equilibrium, kinetics and thermodynamics of methylene blue from aqueous solutions using date palm leaves. *Energy Procedia*, v. 36, p. 898–907, 2013. Disponível em: https://linkinghub.elsevier.com/retrieve/pii/S1876610213011892. Acesso em: 15 jun. 2026.

GUIDA, M. Y.; REBBAH, B.; ANTER, N.; MEDAGHRI-ALAOUI, A.; RAKIB, E. M.; HANNIOUI, A. Biofuels and biochars production from agricultural biomass wastes by thermochemical conversion technologies: thermogravimetric analysis and pyrolysis studies. *Progress in Agricultural Engineering Sciences*, v. 17, n. 1, p. 15–36, 2021. Disponível em: https://doi.org/10.1556/446.2021.00020. Acesso em: 15 jun. 2026.

HAMZAOUI, R.; MUSLIM, F.; GUESSASMA, S.; BENNABI, A.; GUILLIN, J. Structural and thermal behavior of proclay kaolinite using high energy ball milling process. *Powder*

Technology, v. 271, p. 228–237, 2015. Disponível em: https://doi.org/10.1016/j.powtec.2014.11.018. Acesso em: 15 jun. 2026.

HARINDINTWALI, J. D.; HE, C.; XIANG, L.; DOU, Q.; LIU, Y.; WANG, M.; WEN, X.; FU, Y.; ISLAM, M. U.; CHANG, S. X.; KUEPPERS, S.; SHAHEEN, S. M.; RINKLEBE, J.; JIANG, X.; SCHAEFFER, A.; WANG, F. Effects of ball milling on biochar adsorption of contaminants in water: a meta-analysis. *Science of the Total Environment*, v. 882, 2023. Disponível em: https://doi.org/10.1016/j.scitotenv.2023.163643. Acesso em: 15 jun. 2026.

HUANG, C.; XU, C.; MENG, X.; WANG, L.; ZHOU, X. Editorial: Isolation, modification, and characterization of the constituents (cellulose, hemicellulose, lignin, et al.) in biomass and their bio-based applications. *Frontiers in Bioengineering and Biotechnology*, v. 10, 2022. Disponível em: https://www.frontiersin.org/articles/10.3389/fbioe.2022.866531/full. Acesso em: 15 jun. 2026.

INYANG, M.; GAO, B.; YAO, Y.; XUE, Y.; ZIMMERMAN, A. R.; PULLAMMANAPPALLIL, P.; CAO, X. Removal of heavy metals from aqueous solution by biochars derived from anaerobically digested biomass. *Bioresource Technology*, v. 110, p. 50–56, 2012. Disponível em: https://doi.org/10.1016/j.biortech.2012.01.072. Acesso em: 15 jun. 2026.

IOANNIDOU, O.; ZABANIOTOU, A. Agricultural residues as precursors for activated carbon production: a review. *Renewable and Sustainable Energy Reviews*, v. 11, n. 9, p. 1966–2005, 2007. Disponível em: https://doi.org/10.1016/j.rser.2006.03.013. Acesso em: 15 jun. 2026.

JINDO, K.; MIZUMOTO, H.; SAWADA, Y.; SANCHEZ-MONEDERO, M. A.; SONOKI, T. Physical and chemical characterization of biochars derived from different agricultural residues. *Biogeosciences*, v. 11, n. 23, p. 6613–6621, 2014. Disponível em: https://doi.org/10.5194/bg-11-6613-2014. Acesso em: 15 jun. 2026.

KOPP ALVES, A.; BERGMANN, C. P.; BERUTTI, F. A. High-Energy Milling. *Engineering Materials*. Dordrecht: Springer, 2013. p. 77–85. Disponível em: https://link.springer.com/10.1007/978-3-642-41275-2_7. Acesso em: 15 jun. 2026.

KOVALCHUK, I.; ZAKUTEVSKYY, O.; SYDORCHUK, V.; DIYUK, O.; LAKHNIK, A. The effect of high-energy ball milling of montmorillonite for adsorptive removal of cesium, strontium, and uranium ions from aqueous solution. Eng, v. 4, n. 4, p. 2812–2825, 2023. Disponível em: https://www.mdpi.com/2673-4117/4/4/158. Acesso em: 15 jun. 2026.

KUMAR, M.; XIONG, X.; WAN, Z.; SUN, Y.; TSANG, D. C. W.; GUPTA, J.; GAO, B.; CAO, X.; TANG, J.; OK, Y. S. Ball milling as a mechanochemical technology for fabrication of novel biochar nanomaterials. *Bioresource Technology*, v. 312, 2020. Disponível em: https://doi.org/10.1016/j.biortech.2020.123613. Acesso em: 15 jun. 2026.

LEAL, P. V. B.; GREGÓRIO, A. M.; OTONI, E.; DA SILVA, P. R.; KRAUSER, M. O.; HOLZBACH, J. C. Estudo da adsorção do corante azul de metileno em resíduos de babaçu. *Journal of Biotechnology and Biodiversity*, v. 3, n. 4, p. 166–171, 2012. Disponível em: https://doi.org/10.20873/jbb.uft.cemaf.v3n4.leal. Acesso em: 15 jun. 2026.

LEHMANN, J.; JOSEPH, S. Biochar for Environmental Management: Science and Technology. London: Earthscan, 2009.

LEONEL, E. C.; NASSAR, E. J.; CIUFFI, K. J.; REIS, M. J. dos; CALEFI, P. S. Effect of high-energy ball milling in the structural and textural properties of kaolinite. *Cerâmica*, v. 60, n. 354, p. 267–272, jun. 2014. Disponível em: http://www.scielo.br/scielo.php?script=sci_arttext&pid=S0366-69132014000200016&lng=en&tlng=en. Acesso em: 15 jun. 2026.

LI, W.; JIANG, C.; ZHANG, Q.; LI, S. Evaluation of pozzolanic and alkali-activated reactivity of low-purity calcium bentonite. *Materials*, v. 15, n. 22, 2022. Disponível em: https://doi.org/10.3390/ma15228015. Acesso em: 15 jun. 2026.

LIMA, R. N.; PAIXÃO, R. L.; MARQUES, R. B.; MALVEIRA, J. Q.; FURTINI, J. A. O.; RIOS, M. A. de S. Investigação do potencial do talo e da palha da carnaúba para utilização como biocombustível. *Matéria (Rio de Janeiro)*, v. 24, n. 2, 2019. Disponível em:

http://www.scielo.br/scielo.php?script=sci_arttext&pid=S1517-70762019000200335&tlng=pt. Acesso em: 15 jun. 2026.

LOPEZ-TENLLADO, F. J.; MOTTA, I. L.; HILL, J. M. Modification of biochar with high-energy ball milling: development of porosity and surface acid functional groups. *Bioresource Technology Reports*, v. 15, 2021. Disponível em: https://doi.org/10.1016/j.biteb.2021.100704. Acesso em: 15 jun. 2026.

LU, L. Char structural ordering during pyrolysis and combustion and its influence on char reactivity. *Fuel*, v. 81, n. 9, p. 1215–1225, jun. 2002. Disponível em: https://linkinghub.elsevier.com/retrieve/pii/S0016236102000352. Acesso em: 15 jun. 2026.

MARSH, H.; RODRÍGUEZ-REINOSO, F. Activated Carbon. *Oxford: Elsevier*, 2006. Disponível em: https://linkinghub.elsevier.com/retrieve/pii/B9780080444635X50134. Acesso em: 15 jun. 2026.

MAYER-LAIGLE, C.; BLANC, N.; RAJAONARIVONY, R. K.; ROUAU, X. Comminution of dry lignocellulosic biomass, a review: Part I. From fundamental mechanisms to milling behaviour. *Bioengineering*, v. 5, n. 2, art. 41, 2018. Disponível em: https://doi.org/10.3390/bioengineering5020041. Acesso em: 15 jun. 2026.

MERGBI, M.; GALLONI, M. G.; ABOAGYE, D.; ELIMIAN, E.; SU, P.; IKRAM, B. M.; NABGAN, W.; BEDIA, J.; AMOR, H. B.; CONTRERAS, S.; MEDINA, F.; DJELLABI, R. Valorization of lignocellulosic biomass into sustainable materials for adsorption and photocatalytic applications in water and air remediation. *Environmental Science and Pollution Research*, v. 30, n. 30, p. 74544–74574, 2023. Disponível em: https://doi.org/10.1007/s11356-023-27484-2. Acesso em: 15 jun. 2026.

MOHAN, D.; SARSWAT, A.; OK, Y. S.; PITTMAN JUNIOR, C. U. Organic and inorganic contaminants removal from water with biochar, a renewable, low-cost and sustainable adsorbent: A critical review. *Bioresource Technology*, v. 160, p. 191–202, 2014. Disponível em: https://doi.org/10.1016/j.biortech.2014.01.120. Acesso em: 15 jun. 2026.

MORALES-PAREDES, C. A.; RODRÍGUEZ-LINZÁN, I.; SAQUETE, M. D.; LUQUE, R.; OSMAN, S. M.; BOLUDA-BOTELLA, N.; RODRÍGUEZ-DÍAZ, J. M. Silica-derived materials from agro-industrial waste biomass: Characterization and comparative studies. *Environmental Research*, v. 231, art. 116002, 2023. Disponível em: https://doi.org/10.1016/j.envres.2023.116002. Acesso em: 15 jun. 2026.

NANDA, S.; MOHANTY, P.; PANT, K. K.; NAIK, S.; KOZINSKI, J. A.; DALAI, A. K. Characterization of North American lignocellulosic biomass and biochars in terms of their candidacy for alternate renewable fuels. *BioEnergy Research*, v. 6, n. 2, p. 663–677, jun. 2013. Disponível em: https://doi.org/10.1007/s12155-012-9281-4. Acesso em: 15 jun. 2026.

PASUMARTHI, R.; SAWARGAONKAR, G.; KALE, S.; KUMAR, N. V.; CHOUDHARI, P. L.; SINGH, R.; DAVALA, M. S.; RANI, C. S.; MUTNURI, S.; JAT, M. L. Innovative bio-pyrolytic method for efficient biochar production from maize and pigeonpea stalks and their characterization. *Journal of Cleaner Production*, v. 448, art. 141573, 2024. Disponível em: https://doi.org/10.1016/j.jclepro.2024.141573. Acesso em: 15 jun. 2026.

PAULA, E. A. de O.; COSTA, C. Y. M. da; SILVA, L. E. S. da; SOUZA, F. M. de; MELO, R. R. de. Propriedades mecânicas do talo de carnaúba (Copernicia prunifera) obtidas através de ensaios de tração. *Agropecuária Científica no Semiárido*, v. 16, n. 3, p. 122–128, 2020. Disponível em: https://doi.org/10.30969/acsa.v16i3.1267. Acesso em: 15 jun. 2026.

PEREIRA JUNIOR, R. F.; MENDONÇA NEUBA, L. de; SOUZA, A. T.; PEREIRA, A. C.; NASCIMENTO, L. F. C.; MONTEIRO, S. N. Thermochemical and structural characterization of promising carnauba novel leaf fiber (Copernicia prunifera). *Journal of Materials Research and Technology,* v. 18, p. 4714–4723, 2022. Disponível em: https://doi.org/10.1016/j.jmrt.2022.04.127. Acesso em: 15 jun. 2026.

PHIRI, R.; MAVINKERE RANGAPPA, S.; SIENGCHIN, S. Agro-waste for renewable and sustainable green production: A review. *Journal of Cleaner Production*, v. 434, art. 139989, 2024. Disponível em: https://linkinghub.elsevier.com/retrieve/pii/S0959652623041471. Acesso em: 15 jun. 2026.

PRADHAN, S.; ABDELAAL, A. H.; MROUE, K.; AL-ANSARI, T.; MACKEY, H. R.; MCKAY, G. Biochar from vegetable wastes: agro-environmental characterization. *Biochar*, v. 2, n. 4, p. 439–453, 2020. Disponível em: https://doi.org/10.1007/s42773-020-00069-9. Acesso em: 15 jun. 2026.

QI, J.; YU, J.; SHAH, K. J.; SHAH, D. D.; YOU, Z. Applicability of clay/organic clay to environmental pollutants: Green way—An overview. *Applied Sciences*, v. 13, n. 16, art. 9395, 2023. Disponível em: https://doi.org/10.3390/app13169395. Acesso em: 15 jun. 2026.

RAM, V. R.; RAM, P. N.; KHATRI, T. T.; VYAS, S. J.; DAVE, P. N. Thermal analytical characteristics by TGA-DTA-DSC analysis of Carica papaya leaves from Kachchh. *International Letters of Natural Sciences,* v. 26, p. 12–20, 2014. Disponível em: https://doi.org/10.18052/www.scipress.com/ilns.26.12. Acesso em: 15 jun. 2026.

RAMOLA, S.; MOHAN, D.; MASEK, O.; MÉNDEZ, A. (ed.). Engineered Biochar. Singapore: *Springer Nature*, 2022. Disponível em: https://link.springer.com/10.1007/978-981-19-2488-0. Acesso em: 15 jun. 2026.

REZA, M. S.; AFROZE, S.; BAKAR, M. S. A.; SAIDUR, R.; ASLFATTAHI, N.; TAWEEKUN, J.; AZAD, A. K. Biochar characterization of invasive Pennisetum purpureum grass: Effect of pyrolysis temperature. *Biochar*, v. 2, n. 2, p. 239–251, 2020. Disponível em: https://doi.org/10.1007/s42773-020-00048-0. Acesso em: 15 jun. 2026.

RIBEIRO FILHO, M.; MEDEIROS, S.; LOPES, A.; CRUZ, G.; RIOS, M. Research trends of thermogravimetric pyrolysis of carnauba (Copernicia prunifera) and thermokinetic models based on a brief bibliometric investigation. *Energies*, v. 17, n. 23, art. 5851, 2024. Disponível em: https://doi.org/10.3390/en17235851. Acesso em: 15 jun. 2026.

SHAKIR, S. W.; AL-YAQOOBI, A. M. Advanced composite adsorbent based on biochar, bentonite, and boric acid for sustainable removal of Pinoxaden. *International Journal of Renewable Energy Development*, v. 14, n. 6, p. 1250–1261, nov. 2025. Disponível em: https://doi.org/10.61435/ijred.2025.61503. Acesso em: 15 jun. 2026.

SHORE, J. Colorants and auxiliaries: organic chemistry and application properties. 2. ed. Bradford: *Society of Dyers and Colourists*, 2002. v. 1. ISBN 0 901956 77 5.

SILVA, R.; LIMA, D. E. Adsorção de azul de metileno em biocarvão do endocarpo do fruto do ouricuri (Syagrus coronata (Mart.) Becc.) reativado por reação de Fenton. 2017. Dissertação (Mestrado em Engenharia Química) – *Universidade Federal de Alagoas*, Maceió, 2017. Disponível em: http://sucupira.capes.gov.br/sucupira/public/consultas/coleta/trabalhoConclusao/viewTrabalhoConclusao.jsf?popup=true&id_trabalho=6048099. Acesso em: 18 jun. 2026.

SOUSA, R. F. de; SILVA, R. A. R.; ROCHA, T. G. F.; SANTANA, J. A. da S.; VIEIRA, F. de A. Etnoecologia e etnobotânica da palmeira carnaúba no semiárido brasileiro. CERNE, v. 21, n. 4, p. 587–594, dez. 2015. Disponível em: http://www.scielo.br/scielo.php?script=sci_arttext&pid=S0104-77602015000400587&lng=pt&tlng=pt. Acesso em: 15 jun. 2026.

STEINMETZ, D. R. Texture evolution in processing of polystyrene-clay nanocomposites. 2007. Thesis – *Faculty of Drexel University*, Philadelphia, 2007. Disponível em: https://researchdiscovery.drexel.edu/esploro/outputs/graduate/Texture-evolution-in-processing-of-polystyrene-clay/991014632431804721. Acesso em: 15 jun. 2026.

SUBRATTI, A.; VIDAL, J. L.; LALGEE, L. J.; KERTON, F. M.; JALSA, N. K. Preparation and characterization of biochar derived from the fruit seed of Cedrela odorata L and evaluation of its adsorption capacity with methylene blue. *Sustainable Chemistry and Pharmacy*, v. 21, 2021. Disponível em: https://doi.org/10.1016/j.scp.2021.100421. Acesso em: 15 jun. 2026.

SUDHAKARAN, A.; RAJAN, R.; RAVINDRANATH, A. Characterization and application of biochar from spent fermentation sludge of coir wastes in removing malachite green from effluent water. *Pollution*, v. 8, n. 3, p. 1026–1037, 2022. Disponível em: https://doi.org/10.22059/POLL.2022.337925.1340. Acesso em: 15 jun. 2026.

SURYANARAYANA, C. Mechanical alloying and milling. *Progress in Materials Science*, v. 46, n. 1–2, p. 1–184, jan. 2001. Disponível em: https://linkinghub.elsevier.com/retrieve/pii/S0079642599000109. Acesso em: 15 jun. 2026.

TAVARES MARTINS FILHO, R. Biossorventes: biomassa de aguapé e esferas de alginato/goma do cajueiro para adsorção de azul de metileno. 2012. Dissertação (Mestrado em Engenharia Química) – *Universidade Federal do Ceará*, Fortaleza, 2012. Disponível em: http://repositorio.ufc.br/handle/riufc/14904. Acesso em: 15 jun. 2026.

TAVARES VIEIRA, N. et al. Estudo de equilíbrio de adsorção do corante azul de metileno em biocarvão de endocarpo de cansanção como adsorvente. In: *INIC 2024*, São José dos Campos. Universidade do Vale do Paraíba, 2024. Disponível em: https://www.inicepg.univap.br/cd/INIC_2024/anais/lista_geral_trabalhos.html. Acesso em: 15 jun. 2026.

TOMCZYK, A.; SOKOŁOWSKA, Z.; BOGUTA, P. Biochar physicochemical properties: pyrolysis temperature and feedstock kind effects. *Reviews in Environmental Science and Bio/Technology*, v. 19, n. 1, p. 191–215, mar. 2020. Disponível em: http://link.springer.com/10.1007/s11157-020-09523-3. Acesso em: 15 jun. 2026.

VAN LOO, S.; KOPPEJAN, J. The handbook of biomass combustion and co-firing. London: Earthscan, 2008. Disponível em: https://www.taylorfrancis.com/books/mono/10.4324/9781849773041/handbook-biomass-combustion-co-firing-jaap-koppejan-sjaak-van-loo. Acesso em: 15 jun. 2026

VITHANAGE, M.; LAZZARA, G.; UPAMALI, A. (ed.). Clay Composites. *Springer Nature Singapore*, 2023. (Advances in Material Research and Technology). Disponível em: https://link.springer.com/10.1007/978-981-99-2544-5. Acesso em: 15 jun. 2026.

WANG, J.; TAN, Y.; YANG, H.; ZHAN, L.; SUN, G.; LUO, L. On the adsorption characteristics and mechanism of methylene blue by ball mill modified biochar. *Scientific Reports*, v. 13, art. 21516, 2023. Disponível em: https://doi.org/10.1038/s41598-023-48373-1. Acesso em: 15 jun. 2026.

XU, R.; HUANG, J.; GUO, H.; WANG, C.; ZHAN, H. Functions of silicon and phytolith in higher plants. *Plant Signaling & Behavio*r, v. 18, n. 1, e2198848, 2023. Disponível em: https://www.tandfonline.com/doi/full/10.1080/15592324.2023.2198848. Acesso em: 15 jun. 2026.

XU, Y.; CHEN, B. Investigation of thermodynamic parameters in the pyrolysis conversion of biomass and manure to biochars using thermogravimetric analysis. Bioresource Technology, v. 146, p. 485–493, 2013. Disponível em: https://doi.org/10.1016/j.biortech.2013.07.086. Acesso em: 15 jun. 2026.

YANG, X.; LIU, Z.; JIANG, Y.; LI, F.; XUE, B.; DONG, Z.; DING, M.; CHEN, R.; YANG, Q.; AN, T.; SHAO, X.; WANG, L. L. Micro-structure, surface properties and adsorption capacity of ball-milled cellulosic biomass derived biochar based mineral composites synthesized via carbon-bed pyrolysis. *Applied Clay Science*, v. 199, art. 105877, dez. 2020. Disponível em: https://doi.org/10.1016/j.clay.2020.105877. Acesso em: 15 jun. 2026.

YAO, Y.; GAO, B.; FANG, J.; ZHANG, M.; CHEN, H.; ZHOU, Y.; CREAMER, A. E.; SUN, Y.; YANG, L. Characterization and environmental applications of clay-biochar composites. *Chemical Engineering Journal*, v. 242, p. 136–143, abr. 2014. Disponível em: https://doi.org/10.1016/j.cej.2013.12.062. Acesso em: 15 jun. 2026.

ZHAO, F.; SHAN, R.; LI, S.; YUAN, H.; CHEN, Y. Characterization and co-adsorption mechanism of magnetic clay-biochar composite for de-risking Cd(II) and methyl orange contaminated water. *International Journal of Molecular Sciences*, v. 24, n. 6, art. 5755, mar. 2023. Disponível em: https://doi.org/10.3390/ijms24065755. Acesso em: 15 jun. 2026.

ZHAO, S. X.; TA, N.; WANG, X. D. Effect of temperature on the structural and physicochemical properties of biochar with apple tree branches as feedstock material. *Energies,* v. 10, n. 9, art. 1293, 2017. Disponível em: https://doi.org/10.3390/en10091293. Acesso em: 15 jun. 2026.